5-1-2018

A Design Proposal for a Novel Gun-Launched Unmanned Aerial System

Douglas Bahr Rumbaugh, Jr.
Lehigh University, drumbaughjr@embarqmail.com

A Design Proposal for a Novel Gun-Launched Unmanned Aerial System

By

Douglas B. Rumbaugh, Jr.

A Thesis

Presented to the Graduate and Research Committee

of Lehigh University

in Candidacy for the Degree of

Master of Science

in

Mechanical Engineering

Lehigh University

May 2018

This thesis is accepted and approved in partial fulfillment of the requirements for the Master of Science.

_____

Date

_____

Keith W. Moored, Thesis Advisor

_____

Terry J. Hart, Co-advisor

_____

D. Gary Harlow, Department Chair

Department of Mechanical Engineering and Mechanics

Acknowledgments

I would first like to acknowledge the support and guidance given by my advisers: Keith Moored and Terry Hart. I entered this program with very little engineering background, and their recommendations and insights were critical to me overcoming this shortcoming. I'd also like to thank them for providing me the opportunity to work on this project. It has taught me far more about actual engineering than any class ever could.

I would also like to thank David Lee, for allowing me to piggyback off his experimental setup and working with me to schedule wind tunnel time, as well as for biting the bullet and learning LabView, and for helping direct me away from the over-engineered solutions that I'm apparently so fond of in favor of more practical ones.

Jason Conti and Zachary Rambo were also integral to this project's progress; their assistance in CAD modeling, design, and flight testing, was critical. I am very grateful for their help. Specifically, Zachary performed the majority of the modeling for the initial Model 5 GLUAS, before I knew how to use SolidWorks.

Contents

List of Tables

List of Figures

Abstract

A proposed design for a gun-launched, unmanned aerial system (GLUAS) is presented, along with experimental data pertaining to the characterization of said design, and specifically targeted towards improving its aerodynamics through an examination of planform shape and wing flexibility.

The proposed design consists of a deployable wing micro-aerial vehicle (MAV) that can fit inside of a 60mm mortar shell. The wings consist of 5 individual segments on each side, which stack on top of one another within the body, and are deployed by a torsion spring and an interlocking system of gears and bosses. These wings form a roughly semi-circular planform with a slightly adjustable sweep angle.

Flight testing of the proposed design remains inconclusive, as stable flight has not yet been achieved. The current design is difficult to control due to limited control authority provided by a pair of elevons, and has not been successfully trimmed.

Wind tunnel measurements are reported for flat plates of a variety of sweep angles, in order to determine if changing the sweep angle has any significant effect on the performance of a MAV at Reynolds numbers of order 10^5. It is

found that a sweep of 25 degrees potentially contributes to a more efficient wing, however the results are not conclusive. Further, it is shown that a 65 degree wing is conclusively inferior.

Testing also reveals that the use of plastic, in place of metal, to construct the wings could contribute to slightly higher values for the coefficient of lift, as well as range and endurance. It is also shown that the use of a highly-flexible membrane wing results in a significant improvement in the range and endurance of the test model, as well as a significant weight reduction.

Chapter 1

Introduction

1.1 Requirements

The Gun Launched Unmanned Aerial System (GLUAS) is a self-propelled projectile that, ultimately, will be launched from an artillery gun, mortar, or portable grenade launcher, in order to provide easy-to-use and portable reconnaissance capabilities to warfighters on the ground.

The original design targets for this project focused on the design of a 40mm variant to be fired from an M320 grenade launcher. However, this form factor presented a number of design challenges that were considered beyond the scope of the proof of concept phase of the project: namely, the scarcity of electronics designed to fit into this form factor.

As a result, it was decided to pursue the development of a 60mm variant designed for use with a 60mm mortar. This allowed for the testing of a design which could be scaled down to 40mm, and that was built using off-the-shelf

Table 1.1: Initial design targets for the 40mm Hybrid Projectile.

Design Item	**Initial Design**	**Threshold**	**Objective**
Gun	Air Gun/M320	M320	M320
Mass	242g	190g	180g
Range	.125 miles	.5 miles	5-10 miles
Endurance	1-2 min	2-5 min	10-15 min
Altitude	50m AGL	200m AGL	400m AGL
Cost	$1000	$500	$100
Payload	TBD	Same as M433	Same as M433

electrical systems taken from the RC airplane hobbyist market.

No specific design targets were provided for the 60mm variant, however the initial design targets for the 40mm variant, across all project phases, are reproduced in Table 1.1.

In addition to these targets, the projectile must be able to survive the forces of launch, deploy on its own at apogee, and posses a long shelf life. No provisions have been made to accommodate these requirements at this time, however they must be accounted for moving forward.

Specifically, the large forces that the projectile is subjected to at launch preclude the use of traditional servos. Consideration has been given to using piezoelectric solid state actuators, either for wing warping, or rotating each wing independently, however no specific provision has been made to design or implement a solution using this technology. At present, the goal remains to produce a rough proof-of-concept model, for which standard servos and motors remain acceptable.

1.2 Literature Review

There does not appear to exist a standard definition for the term micro aerial vehicle[1], with different sources citing different size requirements. Referenced sizes in the literature range from 6 inches (Ifju, Jenkins, Ettinger, Lian, & Shyy, 2002), up to 1 meter (Watkins et al., 2006). Another common definition is that a MAV is any UAS that is able to be carried, deployed, and operated by a single individual (Galinski & Zbikowski, 2007), which also corresponds to the DARPA definition that, though originally requiring the aircraft to fit into a 150mm bounding box, now only requires it to be "manportable" (Watkins et al., 2006). Based on some of these definitions, the hybrid projectile, with its relatively low required size (either 40mm, or in this case 60mm when folded) appears to fall into this classification.

The design of micro aerial vehicles presents a variety of challenges. They typically operate in low Re ranges, between 10^4 and 10^5, where drag is a significant problem due to flow separation, resulting in sudden losses of efficiency (Ifju et al., 2002). At these Reynolds numbers, separation bubbles as large as 20%-30% of the root chord length of the aircraft can form, dramatically reducing efficiency (Pelletier & Mueller, 2000). This is because the boundary layers over the wing are weak and unable to resist the adverse pressure gradients associated with high angles of attack (Lian & Shyy, 2007). Additionally, these aircraft often fly low to the ground, and thus are subjected to effects

[1]Depending on the source, the exact spelling/wording of this name can vary. For example, Microair Vehicles (Watkins, Milbank, & Loxton, 2006), or Micro Air Vehicles (Zuo & Wang, 2010). The term Micro Aerial Vehicle (Vega, Bose, & Buyuktosunoglu, 2017) is used in this document.

from the atmospheric boundary layer (Watkins et al., 2006).

Due to the unique requirements of designing an aircraft to operate within this size and speed regime, downsizing traditional aircraft designs does not work particularly well (Zuo & Wang, 2010). In order to maximize the lifting surface, various low aspect ratio wing designs are required. Commonly used planforms include the inverse-Zimmerman, Zimmerman, and elliptical planforms (Zuo & Wang, 2010). At particularly low aspect ratios, below 1.25, the lift curves for these planforms have been shown to be non-linear, which complicates modeling them (Torres & Mueller, 2004). Delta wings, and other swept designs, have also been examined as possible planforms for MAVs (Zuo & Wang, 2010) (Galinski, Lawson, & Zbikowski, 2004).

There are several design approaches for MAVs. The first is to use a fixed-wing design driven by a propeller. This design focuses on maximizing the relative planform area, whilst minimizing drag (Ifju et al., 2002). Other designs focus on using pitching or heaving wings (Galinski & Zbikowski, 2007). It is noted that there are no real examples of the former type of design in nature, whereas the latter are quite common (bats, hummingbirds, etc.) (Ifju et al., 2002). However, fixed wing designs are simpler, and further it has been shown that the propeller effects help reduce flow separation over the lifting surface (Galinski & Zbikowski, 2007). With that said, fixed wing systems are very difficult to control, and require either an expert pilot, or a very effective auto-stabilization system (Ifju et al., 2002). These control issues are further exacerbated by the vulnerability of such aircraft to even light-moderate winds (Watkins et al., 2006). However, due to power, reliability, and control sys-

tems constraints, it was decided to pursue a fixed-wing design for the hybrid projectile.

In order to fit this fixed wing inside of the 40mm/60mm required diameter, it was necessary to examine deployable wing designs. Such designs lend themselves well to membrane wings, as many examples of a folding-membrane can be found in nature. Insects such as ladybugs (Saito, Nomura, Yamamoto, Niiyama, & Okabe, 2017) and hymenoptera (Danforth & Michener, 1988) both have sophisticated folding mechanisms to store rather large wings in a small space. On a larger scale, folding wings have been designed on the basis of bats (Bahlman, Swartz, & Breuer, 2013) and birds (Stowers & Lentink, 2015). Such multiply hinged wings allow for large wing areas (and, in the case of the bird wing, large aspect ratios) to fold into a small body, however they are delicate and rely on a variety of servo motors to operate. This makes them not particularly suitable for the hybrid projectile, at least as presented in these papers, as the design will need to withstand significant force loadings on deployment.

In addition to ease of deployment, membrane wings have been shown to possess greater power efficiency than rigid wings at low aspect ratios and moderate Reynolds numbers, thus increasing the endurance of a MAV. In addition, such wings self-camber and thus possess higher C_L values than equivalent flat plates. In fact, at moderate angles of attack, membrane wings were shown improve lift by up to 57% when compared to an equivalent flat plate, with smaller–yet still significant–improvements in $C_{L,max}$ as well. Membrane wings were also shown to have better pitch stability than flat plates in the same study, and it was shown that the method of attachment of the membrane to

the spar can increase lift, at the cost of reduced range and endurance due to induced drag. (Bleischwitz, de Kat, & Ganapathisubramani, 2015).

Another approach to deployable wings is the use of an inflatable design. These designs allow for large wings to be compressed into a small space, and to allow them to be easily cambered. They have been used in earlier gun-launched designs, allowing for, for example, a wing with a span of 62 inches to be deployed from a vehicle with a packed diameter of only 5 inches. These designs use tubular spars made of high-modulus materials to withstand high pressures of inflation. Such wings can be readily designed to camber on inflation. (Brown, Haggard, & Norton, 2003) (Thamann, 2012)

The characterization of these models in the wind tunnel is another focus of this project. Both flow visualization techniques, and direct force measurements, are used for this characterization task. Often, for force measurements, a sensitive 6-axis force/torque transducer is used. For example, Bleischwitz de Kat and Ganapathisubramani use an ATI Nano-17 with a sampling frequency of 1 kS/s and a sampling period of 20s per measurement for force data collection, and high-speed photogrammetry to measure membrane deformation (Bleischwitz et al., 2015). Zuo and Wang also use a force sensor to collect data, although they leave the specific model and details unspecified (Zuo & Wang, 2010). Stanford et al. utilize a sting balance for force and pitching moment measurements (Stanford, Ifju, Albertani, & Shyy, 2008), as does Schutter (Schutter, 2016).

1.3 Aerodynamic Prolegomena

1.3.1 Nomenclature

Parameter	**Symbol**	**Units**
Freestream Velocity	V_∞	$\mathrm{m} \cdot \mathrm{s}^{-2}$
Velocity	V	$\mathrm{m} \cdot \mathrm{s}^{-2}$
Wing Surface Area	S	m^2
Sweep Angle	Λ	degrees
Efficiency	η	Dimensionless
Coefficient of Lift	C_L	Dimensionless
Coefficient of Drag	C_D	Dimensionless
Air Density	ρ	$\mathrm{kg} \cdot \mathrm{m}^{-3}$
Aspect Ratio	AR	Dimensionless
Mass	m	kg
Wing Span	s	m
Trailing Edge Length	s_t	m
Weight	W	N
Kinematic Viscosity	ν	$\mathrm{m}^2 \cdot \mathrm{s}^{-1}$
Dynamic Viscosity	μ	$\mathrm{Pa} \cdot \mathrm{s}$
Root Chord Length	C_R	m
Reynolds Number	Re	Dimensionless
Range	R	km
Endurance	E	s
Energy Density	E^*	$\mathrm{J} \cdot \mathrm{kg}^{-1}$

1.3.2 Important Equations

Lift Equation

$$F_L = \frac{1}{2}\rho V^2 S C_L \tag{1.1}$$

$$C_L = \frac{F_L}{\frac{1}{2}\rho V^2 S} \tag{1.2}$$

Drag Equation

$$F_D = \frac{1}{2}\rho V^2 S C_D \tag{1.3}$$

$$C_D = \frac{F_D}{\frac{1}{2}\rho V^2 S} \tag{1.4}$$

Range Equation

The range equation describes how far an aircraft will be able to fly for a given aerodynamic performance and power source. Specifically, for this document, the range equation as derived for battery powered aircraft is relevant. This equation is given by

$$R = \left(\frac{1}{g}\right)\left(\frac{E^* \cdot \eta \cdot m_{battery}}{m_{total}}\right)\left(\frac{C_L}{C_D}\right) = \left(\frac{E^* \cdot \eta_{total} \cdot m_{battery}}{W_{total}}\right)\left(\frac{C_L}{C_D}\right) \tag{1.5}$$

where E^* represents the energy density of the battery (joules/kilogram), η represents the total efficiency of the aircraft (dimensionless), m represents the

mass of the specified component (kilograms), W represents the weight of the specified component (newtons), and ${}^{C_L}/_{C_D}$ is the aircraft's lift to drag ratio (Hepperle, n.d.).

The range calculated from this formula is in meters. However, reported ranges will be given in kilometers, because the energy density used in the calculations will be in kilojoules/kilogram, rather than joules/kilogram.

Endurance Equation

The endurance equation describes how long an aircraft can remain in the air for a given performance and power source. For this document, the endurance equation for a battery powered aircraft is considered.

$$E = \left(\frac{m_{battery} \cdot E^* \cdot \eta}{W_{total}^{\frac{3}{2}}} \right) \left(\frac{C_L^{\frac{3}{2}}}{C_D} \right) \sqrt{\frac{\rho S}{2}} \tag{1.6}$$

Like with the Range equation, E^* represents the energy density of the battery (joules/kilogram), η represents the total efficiency of the aircraft (dimensionless), m represents the mass of the specified component (kilograms), and W represents the weight of the specified component (newtons). ${}^{C_L^{\frac{3}{2}}}/_{C_D}$ is the power efficiency, derived from the coefficients of lift and drag, ρ is the air density, and S is the surface area of the wing (Schutter, 2016).

The endurance equation provides endurance time in seconds, however the dimensional analysis is a little convoluted, so it seems valuable to step through it.

Given that C_L and C_D are dimensionless, that,

$$\text{joule} = \frac{kg \cdot m^2}{s^2} \tag{1.7}$$

and that

$$\text{newton} = \frac{kg \cdot m}{s^2} \tag{1.8}$$

We have,

$$\frac{kg \cdot \frac{J}{kg}}{N^{\frac{3}{2}}} * \sqrt{\frac{kg}{m^3} \cdot m^2} \tag{1.9}$$

$$\frac{J}{N^{\frac{3}{2}}}\sqrt{\frac{kg}{m}} = \frac{kg \cdot m^2}{s^s}\frac{s^2}{kg \cdot m}\left(\frac{s^s}{kg \cdot m}\right)^{\frac{1}{2}}\left(\frac{kg}{m}\right)^{\frac{1}{2}} \tag{1.10}$$

$$m\left(\frac{s^2 \cdot kg}{kg \cdot m^2}\right)^{\frac{1}{2}} = \frac{m \cdot s}{m} = s \tag{1.11}$$

As this equation will be used with energy densities represented by kilojoules/kilogram, and with the endurance measured in minutes, all reported endurance figures will have had the conversion factor $\frac{1000}{60}$ applied to the number calculated using this formula.

Reynolds Number

In order to ensure that the wind tunnel testing, which requires a scaled-down wing when compared to a full sized aircraft, produces results that are applicable to the full-sized model, it is necessary to ensure that the tests are performed at an equivalent Reynolds number (Re) to that experienced by the full model in flight.

The Reynolds number represents the ratio of inertial to viscous forces in a flow, and is given by the formula

$$Re = \frac{\rho V_\infty L}{\mu} = \frac{V_\infty L}{\nu} \tag{1.12}$$

where L is the characteristic length scale, V_∞ is the freestream velocity, ρ is the air density, μ is the dynamic viscosity, and $\nu = \frac{\mu}{\rho}$ is the kinematic viscosity of the fluid. Strictly speaking, ν is a function of temperature, however for the purposes of this document it is assumed that $T = 20$ degrees C and thus this value is treated as a constant of $15.06 \times 10^{-6} \frac{\mathrm{m}^2}{\mathrm{s}}$. Unless otherwise stated, the characteristic length scale used to calculate the Reynolds number will be the root chord length.

Chapter 2

Design and Fabrication

2.1 Original Design

At the onset of this phase of the Hybrid Projectile Project, the standing design was the Model 4 Gun-launched Unmanned Aerial System (GLUAS), shown in Figure 2.1. This design utilized segmented, flexible wings that stacked on top of one another to fit inside of a 60mm tube (Figure 2.2), but would fan out to provide a sizable lifting surface when deployed. This fanning out was accomplished using two torsion springs, one on each side. The individual wing segments interlocked using a series of bosses and channels to ensure proper deployment.

The model was controlled by means of two elevons, located on the 3rd wing segment of both sides. These surfaces were actuated by means of a pair of servos mounted on the underside of the projectile, connected by a metal rod to protruding control horns on the elevon surface. The wings behind the

Figure 2.1: An image of the CAD model for the Model 4 GLUAS. (Schutter, 2016)

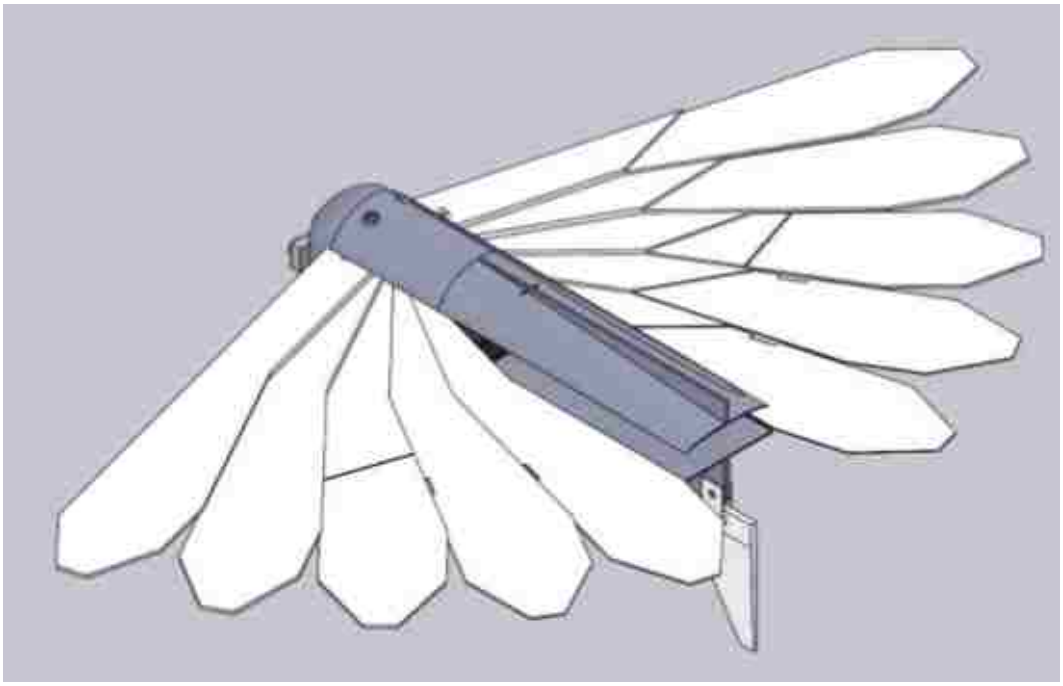

elevons contained slots for these control horns, to allow the wings to fully collapse without interference from these horns. There was also a single rear stabilizer mounted on the lower portion of the fuselage.

The body of the projectile was composed of two pieces, attached to each other by two screws used to attach the wings. Propulsion was provided by a small electric motor mounted at the front, onto which a propeller was affixed using a prop-saver. The camera was attached to the outside of the body, at the front, using hot glue. Control, guidance, and radio/video transmission electronics were attached to the inside of the lower portion of the body using hot glue and soldered connections.

Figure 2.2: An image of the Model 4 GLUAS folded up inside a 60mm mortar shell. (Schutter, 2016)

2.2 Design Changes

2.2.1 Symmetric Tail

During initial powered flight tests performed by Schutter, it was discovered that the Model 4 GLUAS suffered from a severe yaw instability when throttle was applied. Upon the application of the throttle, the projectile would begin to spin in circles in midair. It was thought that this instability was due to the interaction of propeller wash with the asymmetric rear stabilizers. The vorticity from the propeller would strike one side of the stabilizer, pushing on the rear of the projectile and causing it to yaw uncontrollably.

In order to resolve this problem, a symmetrical rear stabilizer setup was used. Rather than a single stabilizer on the lower fuselage, two identical stabilizers were used–one on the top, and one on the bottom. It was hoped that the propeller wash would strike both surfaces, and roughly cancel itself out. Since the implementation of this scheme, the yaw instability has not been noticeably

manifest.

2.2.2 Model 5 Re-design

During powered flight testing of the Model 4 GLUAS, it was noticed that the projectile suffered from a serious pitch instability. A very small perturbation, be it from the control surfaces, or a gentle breeze, would cause the projectile to pitch upwards violently and uncontrollably, resulting in a crash.

It was thought that this instability was due to the relative position of the aerodynamic center and the center of gravity of the Model 4. During unpowered flight this instability was not present, and so it was thought that the acceleration of air over the projectile by the propeller during powered flight moved the aerodynamic center of the model forward. Figure 2.3 shows a Model 4 fuselage with the approximated locations of these points marked down. It should be noted that the range of stable locations for the center-of-gravity in micro aerial vehicles is typically quite small, and thus this particular problem is not uncommon in the realm of MAV design (Stanford et al., 2008).

It should be noted that Schutter calculated the theoretical location of the aerodynamic center, and found that it was forward of the center of gravity (Schutter, 2016, p. 57), and so his calculations match with this theory.

In order to confirm experimentally that the instability was due to this, a Model 4 projectile was modified through the use of fishing weights and other heavy metal objects in order to force the center of gravity as far forward as possible. The specifics of this test are detailed in Section 4.1. The net result was a reasonable confirmation that moving the center of gravity forward would

Figure 2.3: The Model 4 GLUAS with the approximated locations of the center of gravity and aerodynamic center marked using sticky notes. The center of gravity is indicated by the yellow stick note closest to the back of the projectile, and the green sticky note at the front is the estimated location of the aerodynamic center.

resolve this issue.

As a result, a comprehensive redesign of the GLUAS was initiated with the goal of resolving this instability. This would lead to the current, Model 5 GLUAS. This new model was designed from scratch, rather than by modifying the existing Model 4 CAD files.

To resolve the pitch instability, the mounting points for the wings were moved back from the front of the projectile, with the goal being to move the aerodynamic center rearward. In the space created at the front of the GLUAS by this move, as many of the electrical systems as possible were positioned–to move the center of gravity forward.

Further modifications were also made. Notably, the camera was relocated to the inside of the projectile. In the Model 4, the camera was mounted on the outside of the projectile. As a result, on landing, occasionally the propeller would hit the camera and destroy it. By positioning the camera inside of the fuselage, it was much better protected.

The Model 5 GLUAS fuselage consists of 3 pieces. The bottom section contains mounting points for most of the electronics, as well as mounting holes for the wings, and two of the four mounting points for the front motor. The battery is located in the rear of this section. In addition, the antenna is mounted in this section. This section is shown in Figure 2.4.

The four posts in the front section are spacers for the circuitry. The engine speed controller (ESC) fits between them, and the circuit board onto which all of the other components are attached rests on top of them. The small square in the front corner is the mounting point for the GPS antenna.

The middle section is a simple piece that attaches to the bottom via four screws. It has a hole to allow the control wires for the motor to enter the front section, and further serves to protect the electronics and contain all of the wires within the fuselage. However, its most important role is to provide a bearing surface for the torsion springs used to hold the wings. The rear wall of this section is the surface upon which these springs push. As a result, it has been thickened several times over the lifetime of the Model 5 to ensure that it doesn't break. This section is shown in Figure 2.5.

Figure 2.6 shows the underside view of the top section of the projectile. This section contains the cutouts for the torsion springs used to mount the wings, as well as mounting points in the back for the video transmitter (VTX) and in the front for the control servos.

The middle section attaches directly to the bottom section. The top and bottom section are held together by the screws used to attach the wings, and by the motor itself. Figure 2.7 shows the fully assembled CAD file for the Model 5 GLUAS, with wings, stabilizers, etc. Note that the outer surface has indentations to allow for a folding propeller, which would be required to fit the entire assembly into a mortar shell or grenade.

Model 5 Wings

The wings for the Model 5, aside from being shortened, are not far different from the Model 4 wings. Each side of the projectile has five wing segments, with the 3rd segment containing the elevon. Each segment has a slightly different thickness–with the wings growing thinner towards the trailing edge.

Figure 2.4: An image of the lower section of the Model 5 GLUAS.

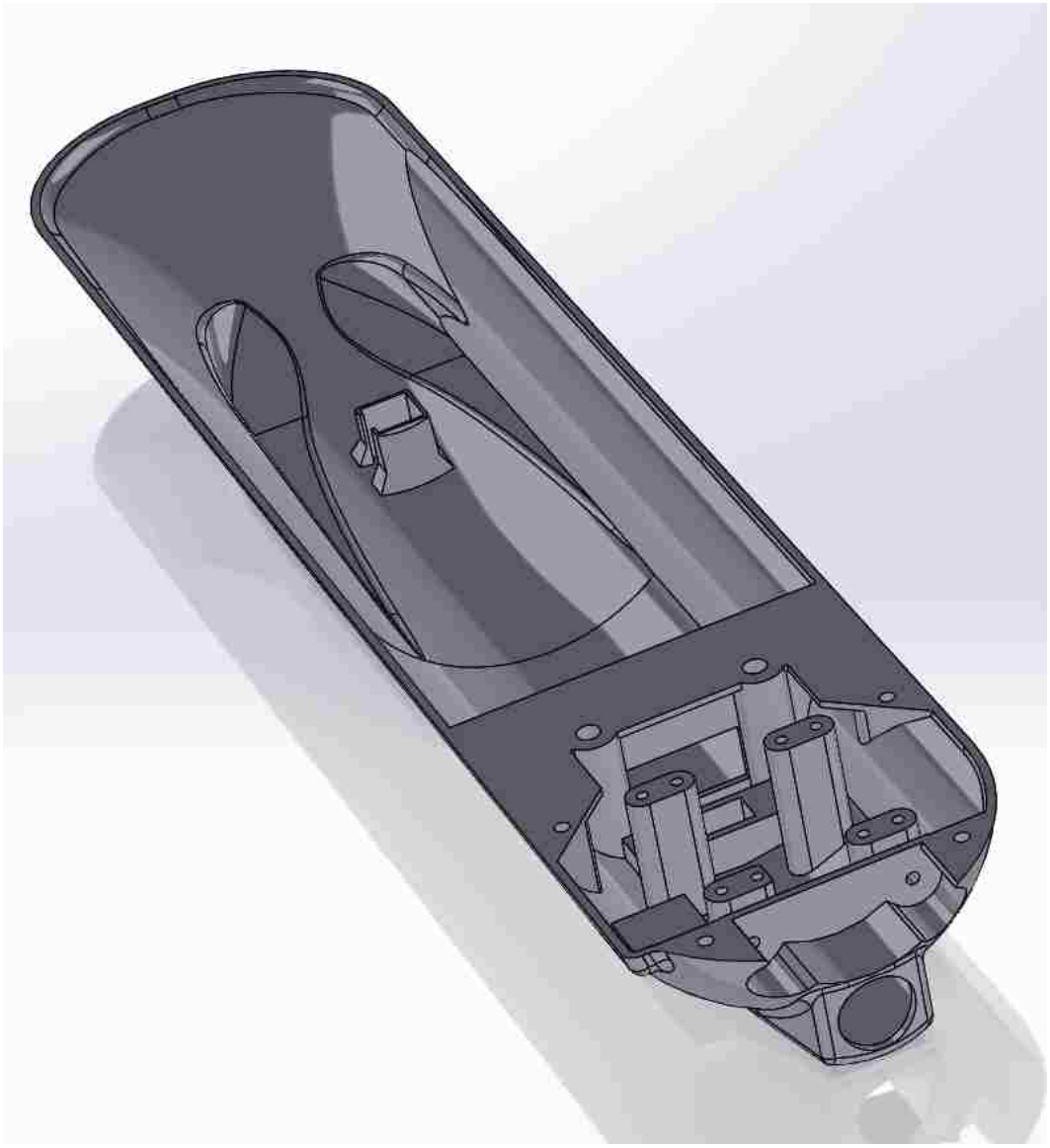

Figure 2.5: An image of the middle section of the Model 5 GLUAS.

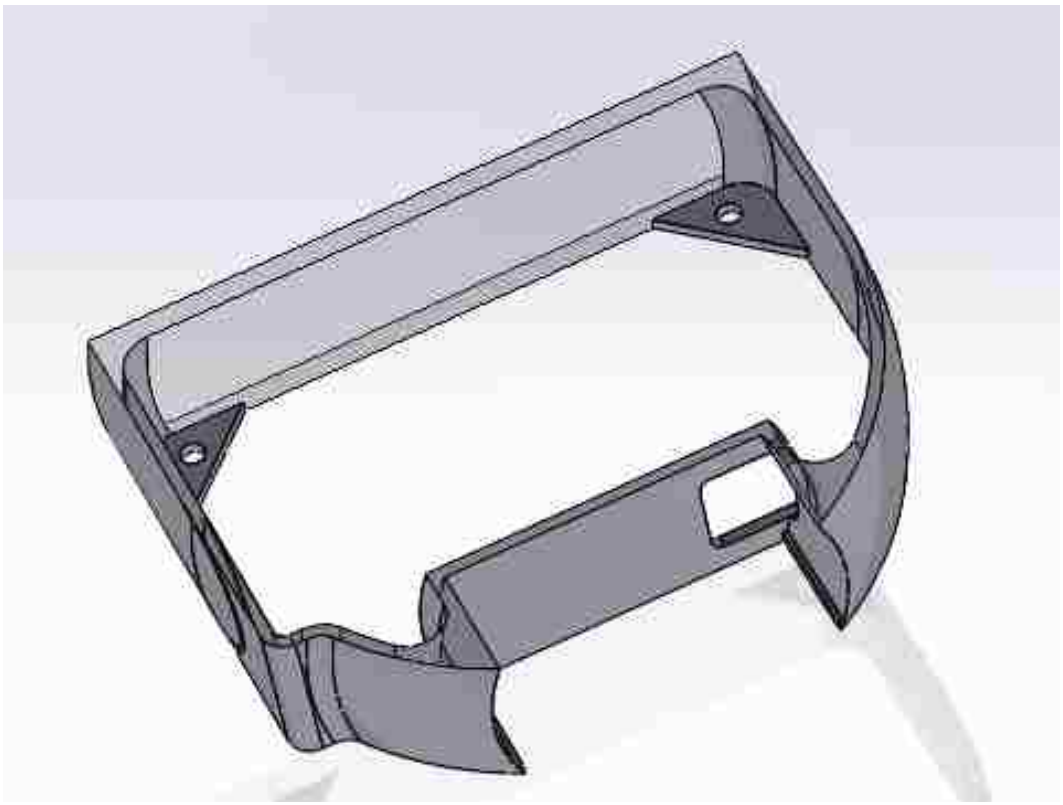

Figure 2.6: An image of the upper section of the Model 5 GLUAS.

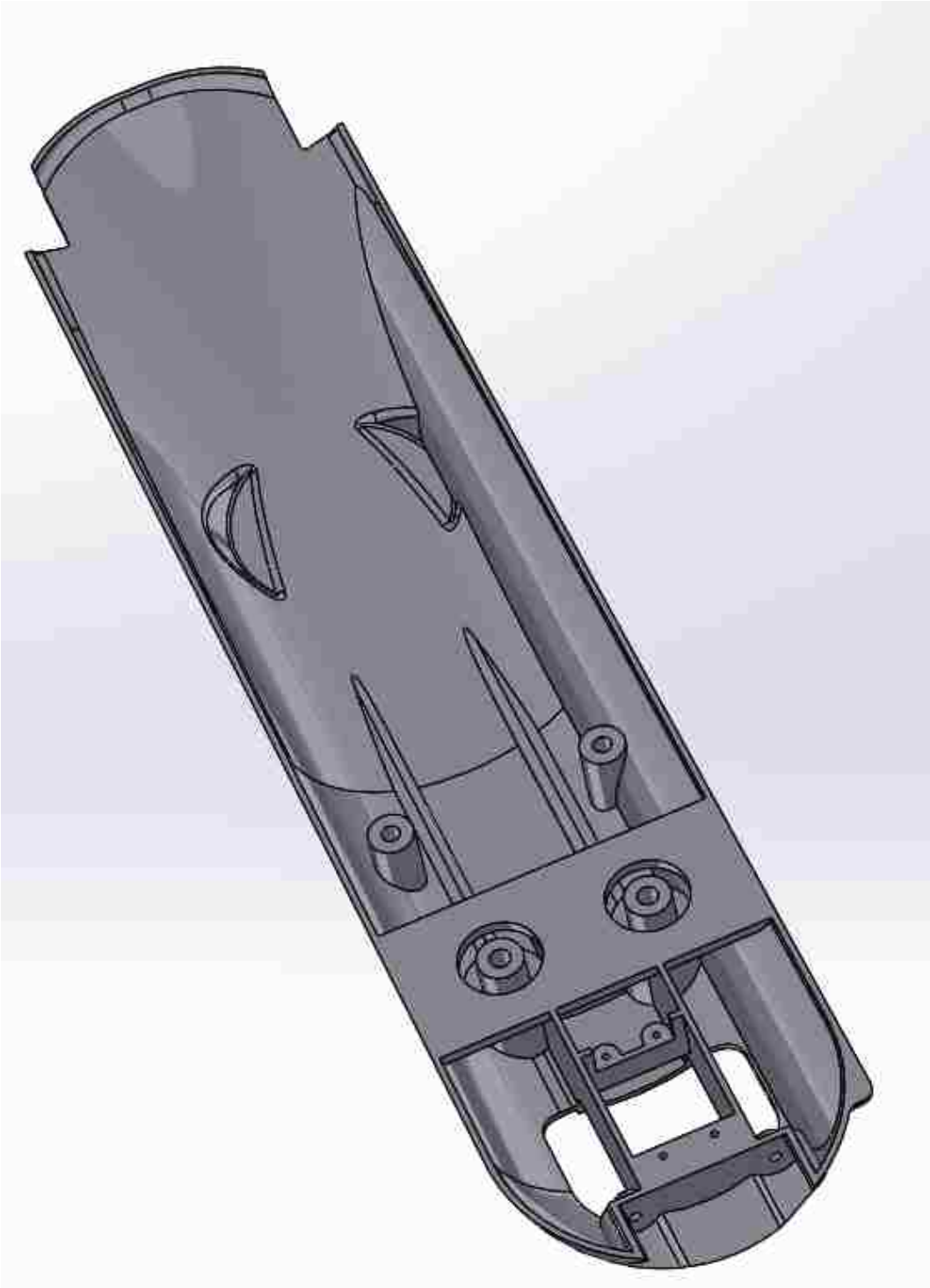

Figure 2.7: The Model 5 GLUAS. The gaps in the wings are where the elevons go–they aren't integrated into this CAD model.

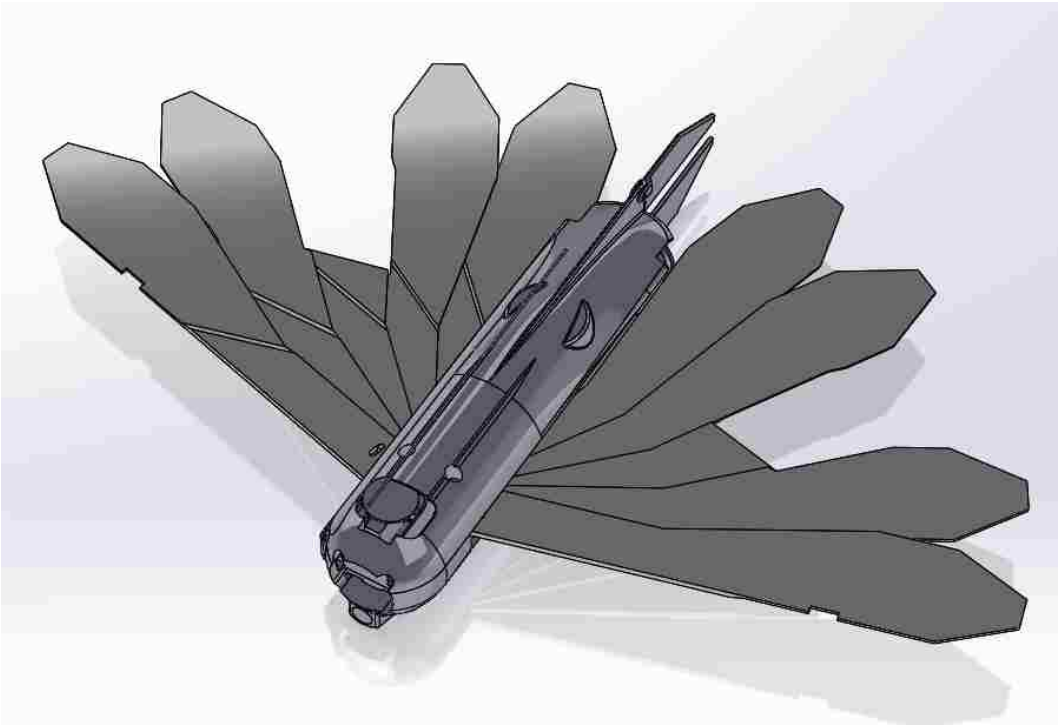

Figure 2.8: A close-up view of the interlock between the two wings.

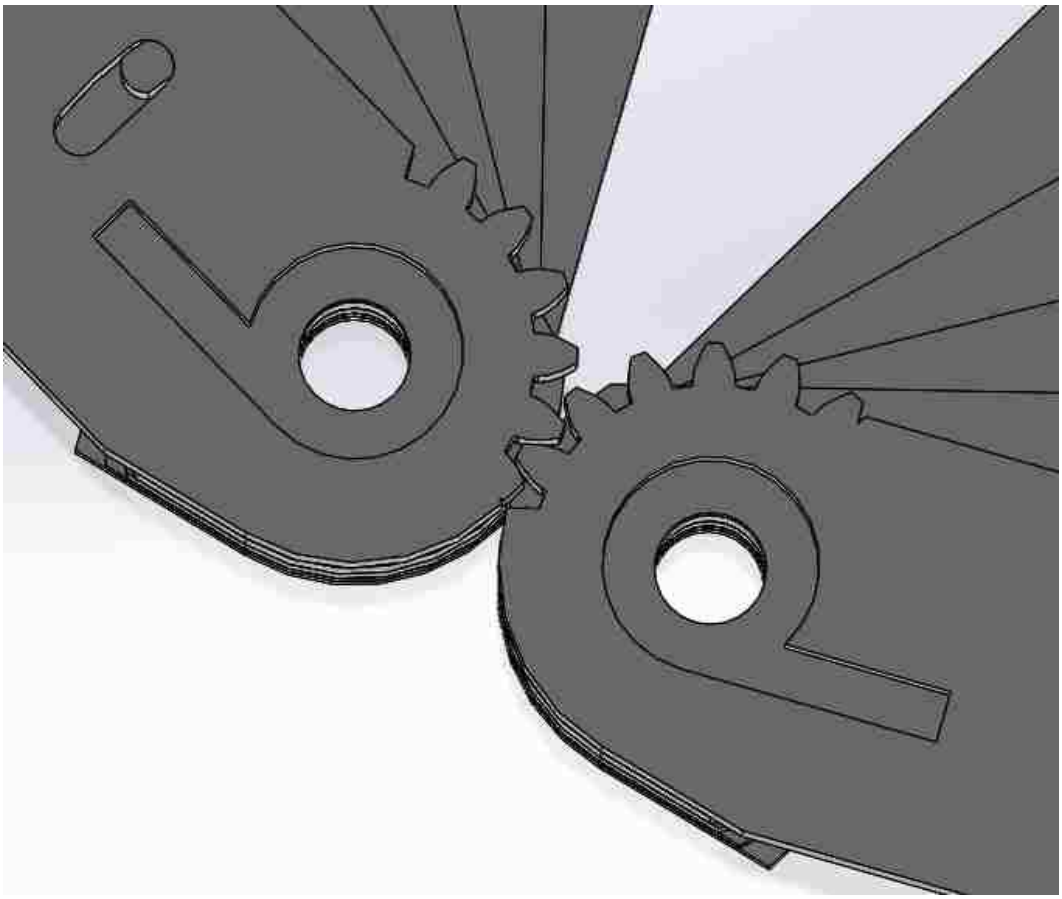

The thickness of the wings also varies along the span. The portions of the wing closest to the root experience the largest bending moment, and thus must be thicker to counter-act this. The bending moment at the wing tip is less severe, and making the wings thinner in this region assists fitting the wings together when folded, allowing the segments from either side to interlace with one another and occupy the same area.

Figure 2.8 shows a top view of the interlock between the two wings. The first wing segment on either side contains a cutout into which the torsion spring

Figure 2.9: A front view of the wings, demonstrating the thickness difference both per segment, and also along the spanwise length of each segment.

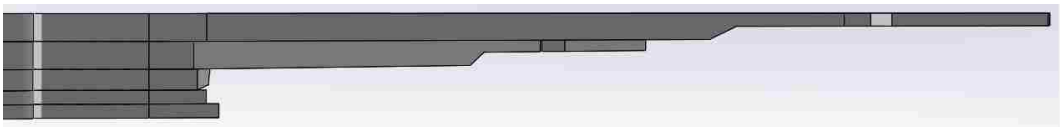

fits, and a gear to allow the two wings to interlock with one another. The wing segments for either side interlock together using a series of bosses. This arrangement allows the torsion springs to force the wings to deploy completely, even though only the first segment is in direct contact with the spring. Note that this is a common point of failure, as these bosses sheer off very easily on landing, forcing the wings to be deployed and fixed in place manually (duct tape typically suffices for this). These bosses are staggered so as to make it impossible to attach the wing segments in the wrong order, or on the wrong side.

The left and right side wing segments are mirror images of one another, with the only exception being the torsion spring cutouts being fixed on the same side for the first wing segment. The surface area of each wing segment is given in Table 2.1. Taking these values into account, the Model 5 GLUAS has an overall planform area of $96\,700\,\mathrm{mm}^2$ ($0.0967\,\mathrm{m}^2$).

Comparing this value to the Model 4's planform area, as reported in Schutter's thesis, the two wings have identical planform areas. The Model 4 has a planform area of $0.097\,\mathrm{m}^2$ (Schutter, 2016, p. 57), and the Model 5, to two significant figures, has an area of $0.097\,\mathrm{m}^2$. Any loss of area due to the wing redesign is thus outside of the limits of detection for the measurement technique used.

Table 2.1: A table of the surface area for each wing component, taken to 3 significant figures.

GLUAS Component	Surface Area
Segment 1	8330 mm^2
Segment 2	8300 mm^2
Segment 3	3600 mm^2
Elevon	4850 mm^2
Segment 4	8360 mm^2
Segment 5	8500 mm^2
Fuselage	12 800 mm^2

Because of this, the displacement of the aerodynamic center from the leading edge of the wing should remain unchanged from that calculated by T Schutter. He calculated, for the Model 4 GLUAS, that it would lie 80 mm from the leading edge of the wing[1]. (Schutter, 2016, p. 57)

The elevon control surfaces have, combined, a total area of 0.0097 m^2, which constitutes about 10% of the total planform area. When the leading edge is held at a sweep angle of 0 degrees, the wings have an effective aspect ratio of 5.9 with a span of 0.240 mm.

2.2.3 Motor Mount

The motor mount presented problems during flight testing. Because the motor is enclosed by its mount, it is susceptible to loss of energy due to friction between the spinning motor and the edges of the mount, should the fit be too tight. This problem was resolved in most cases by increasing the size of the

[1]Note that the original value was expressed to 3 significant figures, however as the wing area was only expressed to 2, the actual value is only known to 2, and thus the number of significant figures is here reduced. Further, the units of this measure were not listed in the original document, so the use of mm is assumed.

Figure 2.10: A front view of the Model 5 GLUAS, showing the motor and its mount, as well as the folding propeller cutouts.

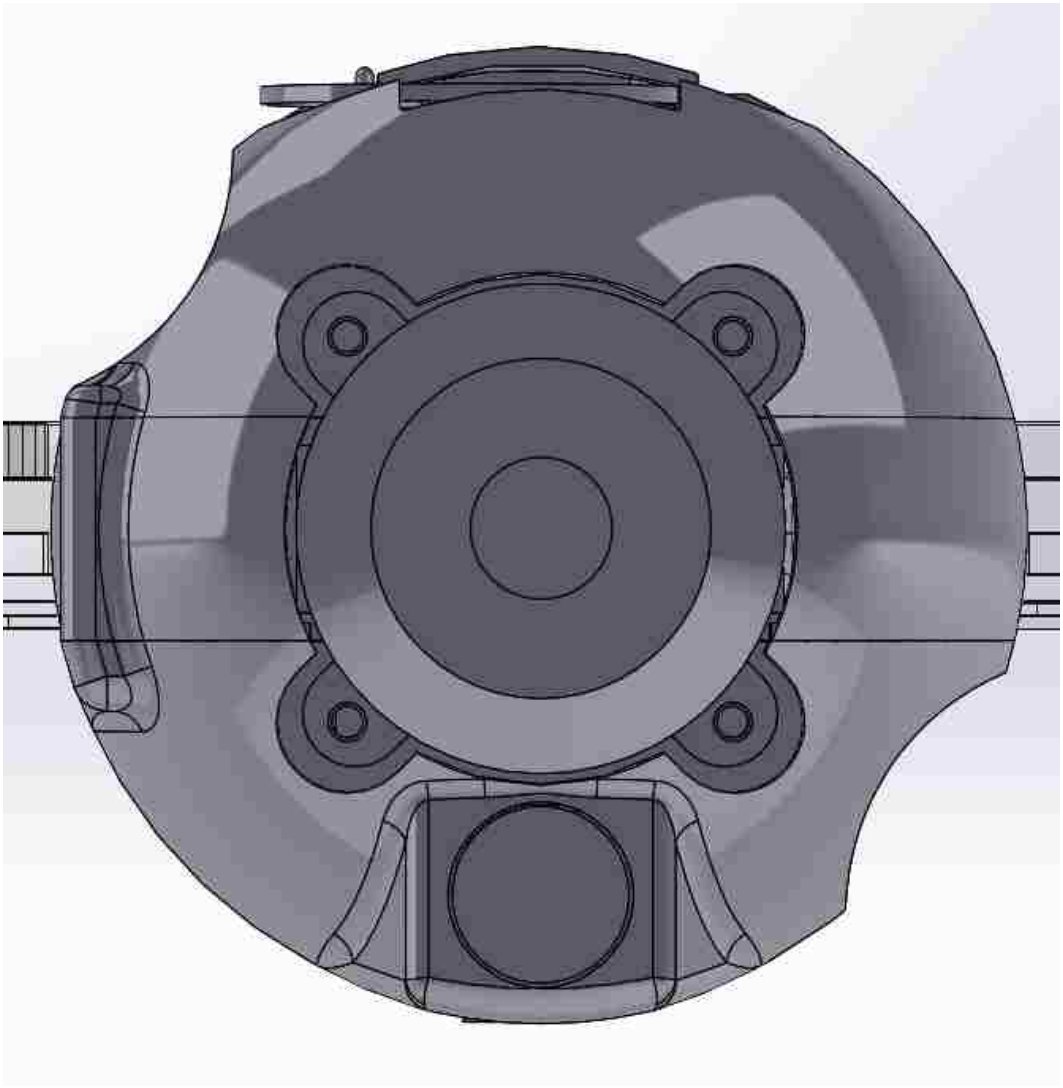

motor mount's hole, to allow sufficient tolerances for the motor to sit in the mount without making contact with its sides.

However, problems still arose as a result of insufficient strength in the connection between the top and bottom sections of the fuselage. The top section contains the torsion springs used to deploy the wings and hold them forward. These springs also push forward on the top section itself. Repeated crashes weakened the connection between the top and bottom section at the wing mounting points, which would occasionally result in this connection breaking entirely. While the GLUAS would still remain intact because of the connection of the two sections via the motor itself, this disconnection would allow the torsion springs to force the front section forward, onto the motor. This would result in the top part of the motor mount effectively pinching off the motor, preventing it from spinning.

This would occasionally happen midflight, especially during pitching maneuvers, resulting in the GLUAS loosing all thrust and crashing. In order to help prevent this from happening, the connection between the two model sections at the wing mounting points was strengthened.

2.2.4 Propeller Mount

During flight testing, one common occurrence was a loss of the propeller midflight. Either the propeller would slip the o-ring used to secure it to the prop-saver, or the o-ring would break. The net effect was the same in either case–an immediate termination of the test flight.

After spending quite some time trying to fine-tune the prop-saver arrange-

(a) The original, prop-saver, propeller mounting design.

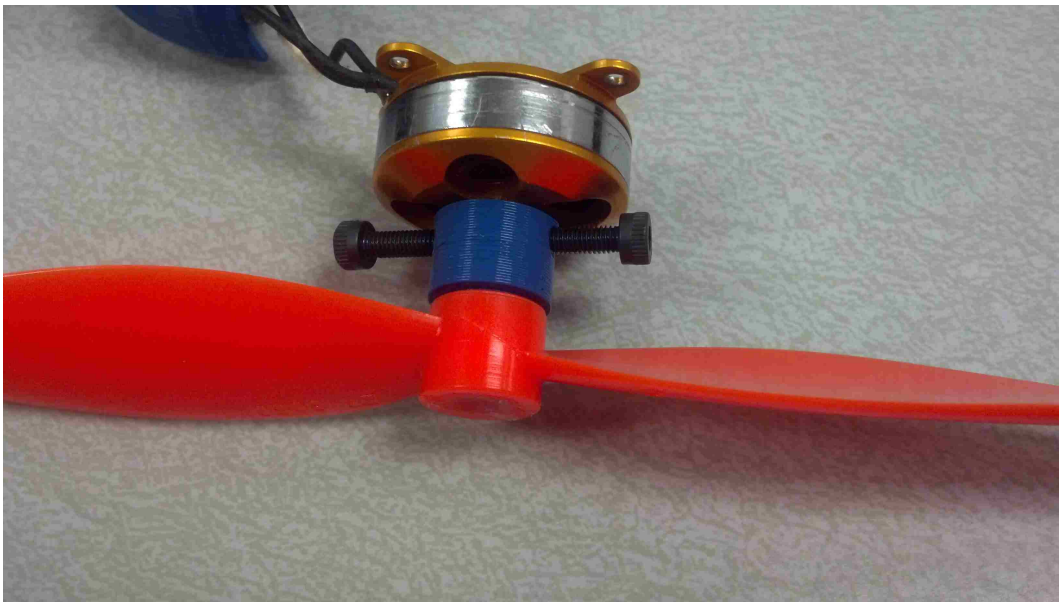

(b) The new propeller mounting scheme.

Figure 2.11: A comparison of old and new propeller mounting schemes.

ment in order to prevent this from happening, it was decided to develop a new method for attaching the propeller to the motor. This ultimately took the form of a small, 3D printed adapter that the propeller would be attached to using hot glue, and that would bolt onto the front of the motor.

Since the adoption of this new mounting scheme, the propeller has not fallen off. However, the disadvantage is that, with the more secure mount, the propeller breaks more frequently. The idea of the prop-saver is to allow the propeller to pop off of the front of the projectile on impact, thus decreasing

Figure 2.12: A CAD model of the propeller adapter.

the chances of it breaking. The new mount doesn't release the propeller as easily, and so the propeller usually doesn't survive the flight. Occasionally the glue joint will break, sparing the propeller–but that is atypical.

2.2.5 Model Trim

It was discovered that the Model 5 has a very strong left-turn tendency. This is normal for aircraft, and is a result of the propeller effects. In addition to the propeller itself causing a left-roll moment, when the propeller is at some angle of attack, the difference in lift produced by one blade versus the other results in a left-yaw tendency as well, an effect known as the P-Factor (Selig, 2010).

In order to help counteract this, it is traditional to use the rudder–especially during takeoff, when the angles of attack are highest. Unfortunately, the GLUAS does not possess a controllable rudder, or any real yaw control for that matter. The elevons can be used to provide roll control, but this is limited due to constraints on the overall throw of the servos, and proved insufficient

Figure 2.13: One of the two offset rear stabilizers, with a 10 degree angle.

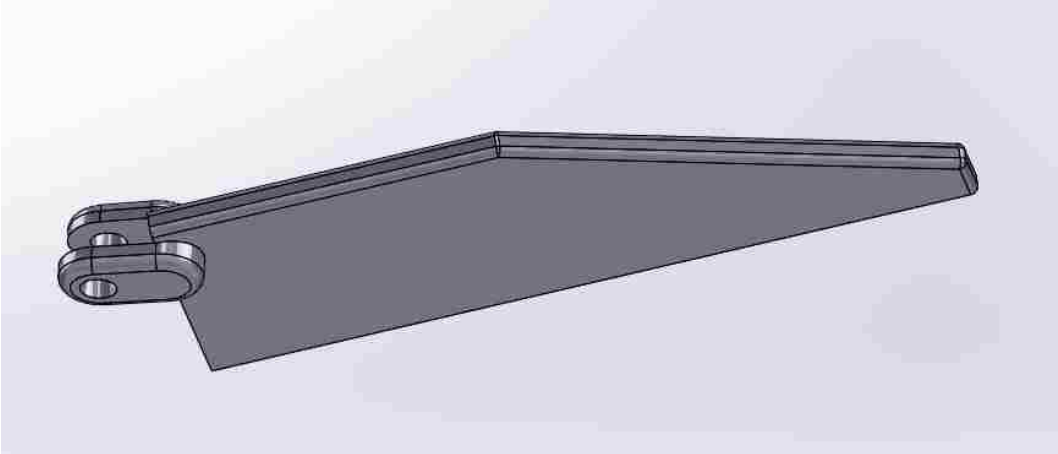

to balance out this left-turn tendency on takeoff.

As a result, it was decided to modify the rear stabilizers with a fixed 10 degree offset. This would, theoretically, help to overcome this left-turn tendency and keep the projectile stable during launch. It would, however, induce a right-turn tendency as lower angles of attack, but it is hoped that the roll control provided by the elevons would be enough to offset this and allow for stable flight.

2.3 Electrical Systems

During the redesign of the GLUAS, the entire electrical system of the Model 4 was revised and redesigned. The Model 4 was plagued by overheating issues, difficult to repair in the field, and time consuming to build. During the design of Model 5, it was decided to address all three of these issues.

The overheating in Model 4 was due to the voltage regulators used–specifically,

Figure 2.14: The Lisa/S autopilot board used in the GLUAS.

the voltage regulator built onto the ESC board. The design consisted of two voltage regulators in parallel, the one on the ESC, and a standalone one to service the video transmission system. This was resolved by moving to a single voltage regulator system. The ESC board was replaced with a 20A ESC from ReadyMadeRC's SP Series, which does not have an onboard regulator. Then, a Pololu 5V 1A step down regulator was used for the control electronics. The ESC and video systems were directly wired to the 11.1v lithium polymer battery, and the control electronics were wired through this voltage regulator.

For the video system, PICO-WIDE-V2 compact camera was used, connected to a Cricket Pro 5.8GHz VTX for transmission. This VTX was then connected to a cloverleaf antenna attached in the back of the GLUAS. It was decided to use 5.8GHz because of the increased image quality. This signal has lower penetration, and is easily blocked, however this is not a problem at the test flight locations.

The control board used was a Lisa/S, produced by 1BitSquared (See Figure 2.14). This small board contains a 3-axis magnetometer, barometer, GPS

Figure 2.15: The electronics package located in the front of the Model 5 GLUAS.

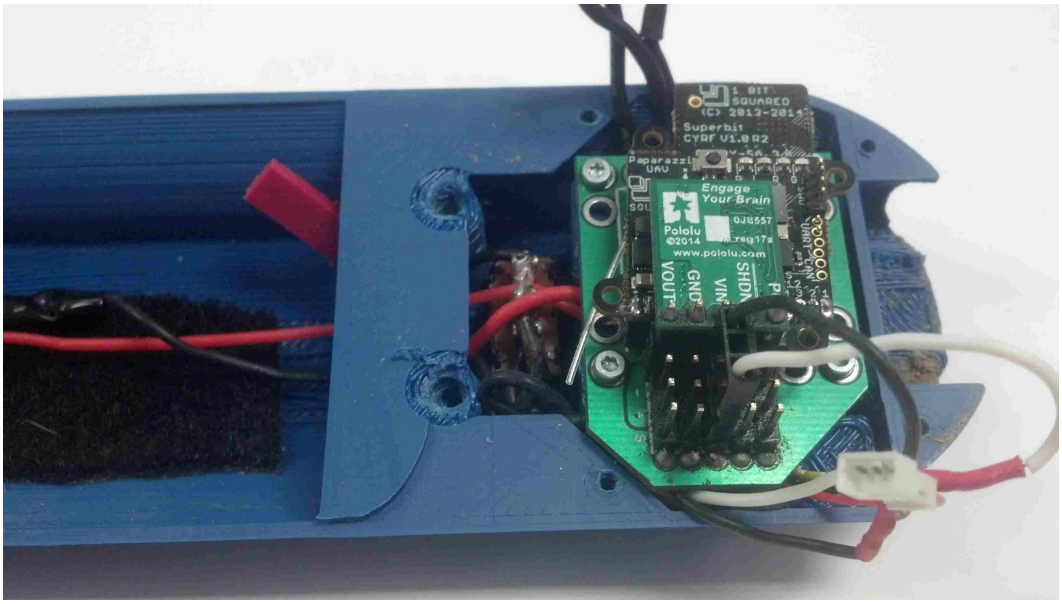

module, 3-axis gyroscope and accelerometer, and a telemetry uplink/downlink module. It runs the open-source Paparazzi autopilot software.

In order to resolve the second and third issues, it was decided to replace as many of the originally soldered connections with easy to use connectors. The motor connects to the ESC using small banana clips[2], and all of the boards (voltage regulator, Lisa/S) attach via header pins. A small circuit board was designed to allow the boards, ESC, and servos, to easily plug in via header pins.

Figure 2.15 shows a picture of the electronics installed in the front of the lower-portion of the GLUAS. The four main components are stacked–voltage regulator on top, then Lisa/S, then circuit board, and finally the ESC and

[2]This connector went through a number of iterations. It took quite a bit of experimentation to find the best sort of connector within the small space that was available.

Figure 2.16: The electronics package located in the top of the Model 5 GLUAS.

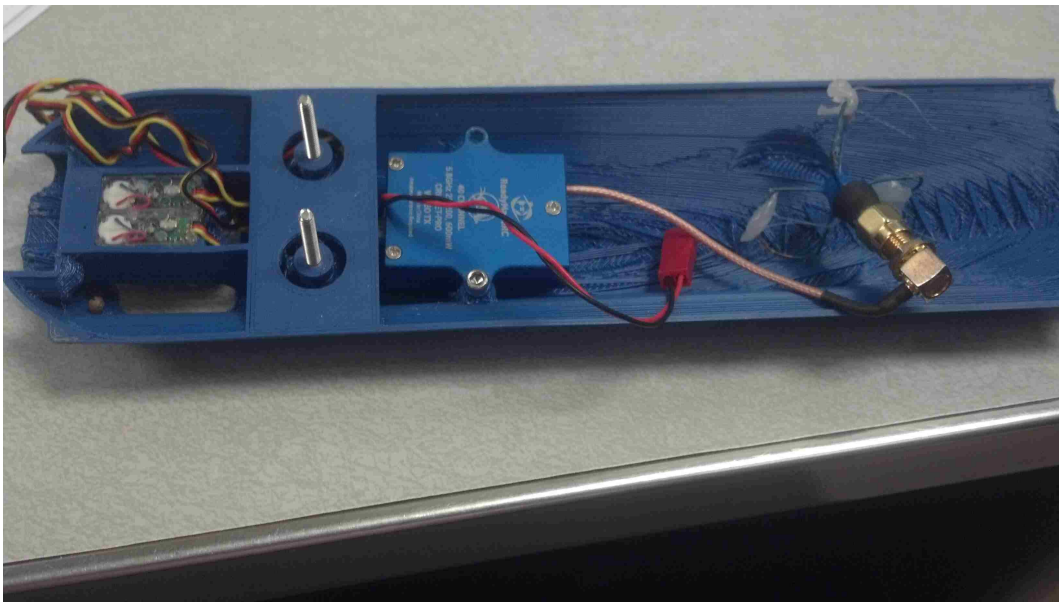

camera are hidden beneath the circuit board. Beside the circuit board, on the bottom of the fuselage, is a power switch that protrudes out the bottom of the projectile to allow it to be easily turned on and off. The wires passing into the back portion of the fuselage are connectors for the battery and VTX module, both of which are positioned in the main body of the GLUAS.

Figure 2.16 shows the electrical components located on the upper portion of the GLUAS fuselage. At the front are the servos used for elevon control, and in the rear are the VTX module (the blue box) and antenna.

2.4 Membrane Wing Model

In addition to the segmented wing Model 5, a design was drawn up for a proof-of-concept membrane wing, the Model 5m. The overall fuselage is identical to

Figure 2.17: A planform view of the Model 5m GLUAS. This CAD diagram does not include the latex membrane, which will be spread over the spars.

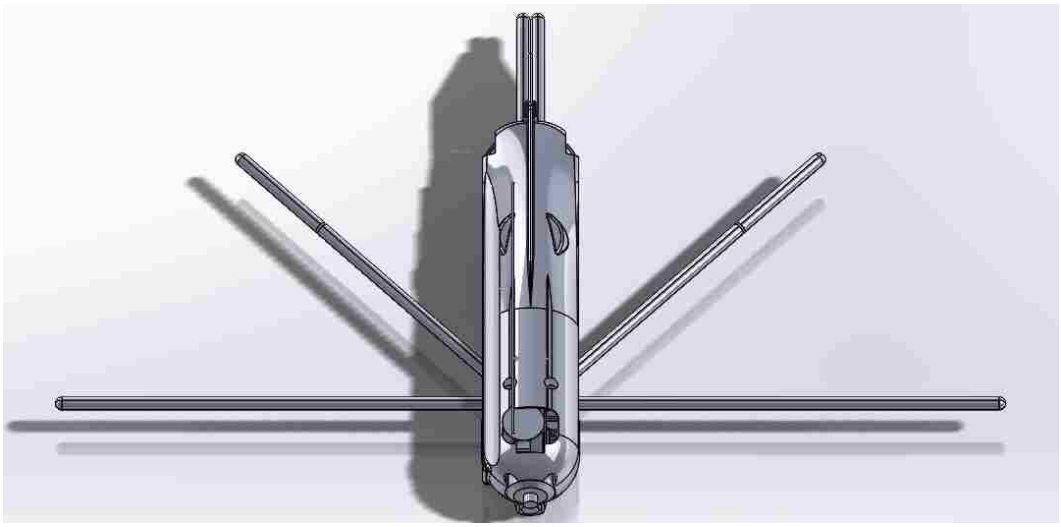

the Model 5, however rather than using segmented plastic wings, a series of three (on each side) spars are mounted, over which a latex membrane will be spread. Figure 2.17 shows a planform view of the design.

The leading edge spar, and the chordwise spar, are both rigid and fixed. These provide structural support for the wing. The middle spar is segmented, and will be connected together using a hinge. This hinged spar will be used in the same manner as the Model 5's elevons, to provide a rudimentary control surface by allowing the membrane to be warped. Ultimately, a better control system will need to be designed, potentially using solid state actuators to either warp the wing, or rotate each wing's leading edge.

In the current physical design, these spars have been constructed out of hollow carbon fiber rods, which are lightweight and provide a high amount of strength and rigidity. During wind tunnel testing of the membrane wing model (as discussed in Section 3.4.3), it was observed that a strictly 3D printed

spar was too flexible, and spars themselves flexed periodically when at speed. These spars are cylindrical, and the membrane will be attached to them in such a way to allow it free rotation about the spar, as it has been shown that this setup results in higher coefficient of lift values than directly fixing the membrane in place (Bleischwitz et al., 2015).

In the final design, these wing spars will need to fold inside the body of the GLUAS and deploy using a spring, in the same way as the segmented plastic wings of the Model 5 GLUAS. At present, these spars are fixed in place using a mounting hub that fits into the wing mounting section of a standard Model 5 fuselage. This hub is shown in Figure 2.18. Figure 2.19 shows the arrangement of these hubs in the actual projectile.

The elevon portions of the middle spar are attached using a simple hinging mechanism. The initial design of the hinge is shown in Figure 2.20. This hinge allows for one degree of rotational freedom, to allow the wing to warp up or down. The elevon section is attached using a control rod to the servo motors used in the Model 5 to actuate the elevons, and the same autopilot/control code is used for both models. Unfortunately, due to the highly flexible nature of the membrane wing, it is difficult to adequately describe the surface area of the wing that is involved in the actuation of these control surfaces.

The membrane spars themselves are each 240 mm in length. By approximating the planform as a circular sector, the total area of one side of the wing can be calculated using the equations provided in Section 3.2.1, to be $0.045\,\mathrm{m}^2$. Thus, combining this with the fuselage area from Table 2.1, we can calculate the total planform area of the membrane wing model to be $0.10\,\mathrm{m}^2$,

Figure 2.18: An image of the CAD diagram for the spar hub for the Model5m GLUAS.

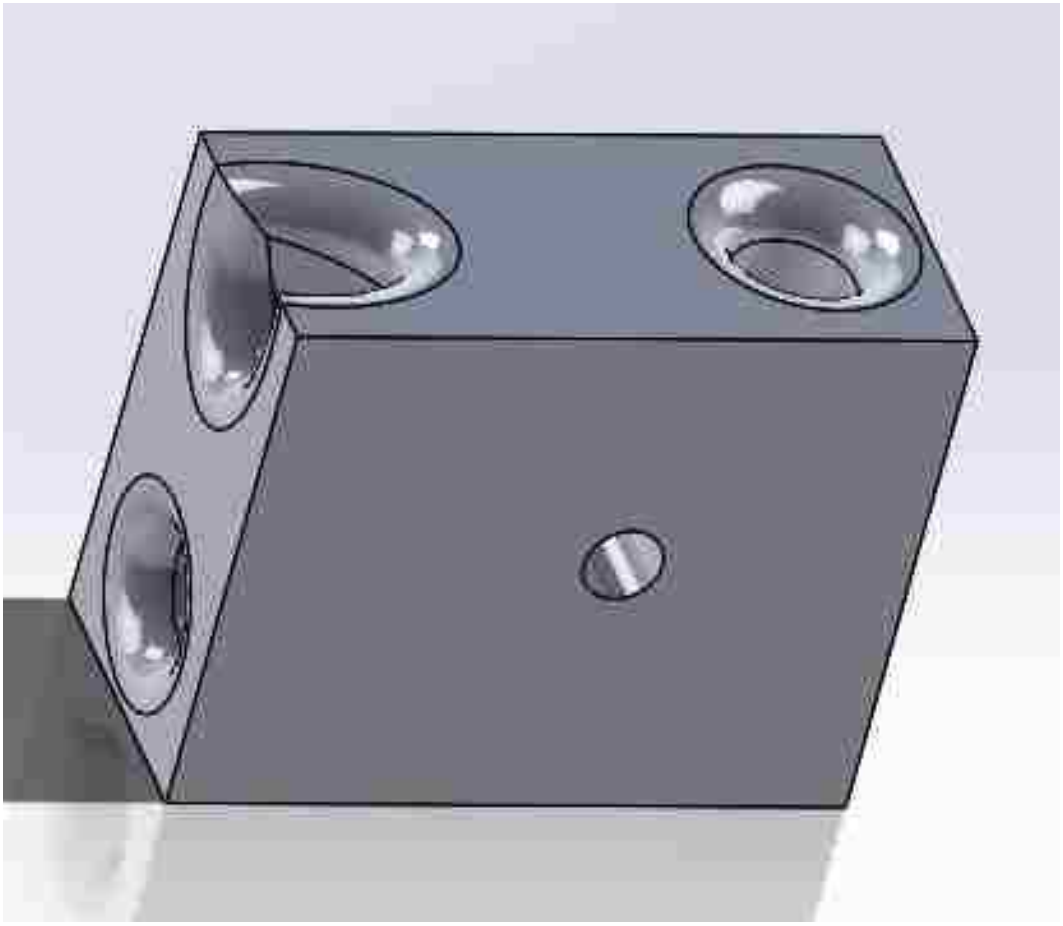

Figure 2.19: A top view of the Model 5m with the fuselage made transparent, to show the arrangement of the membrane hub blocks and the attachment points to the rest of the projectile.

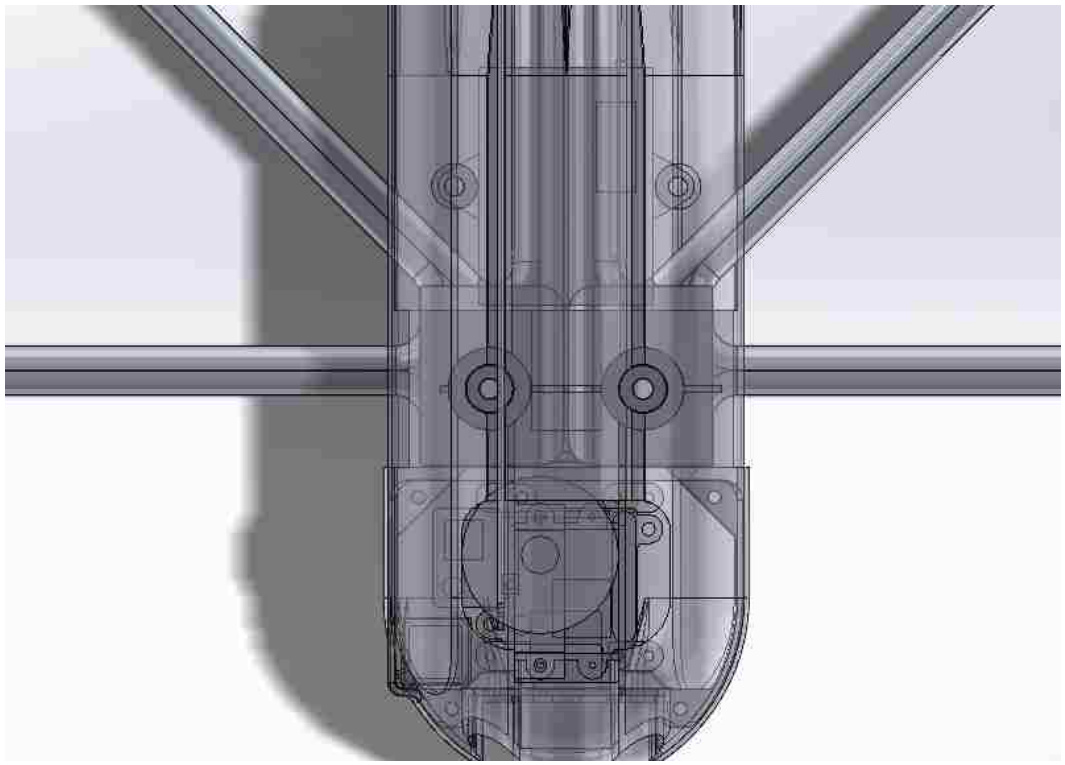

Figure 2.20: The hinge joint used for the elevon portion of the middle mounting spar. This was designed and modeled by Jason Conti.

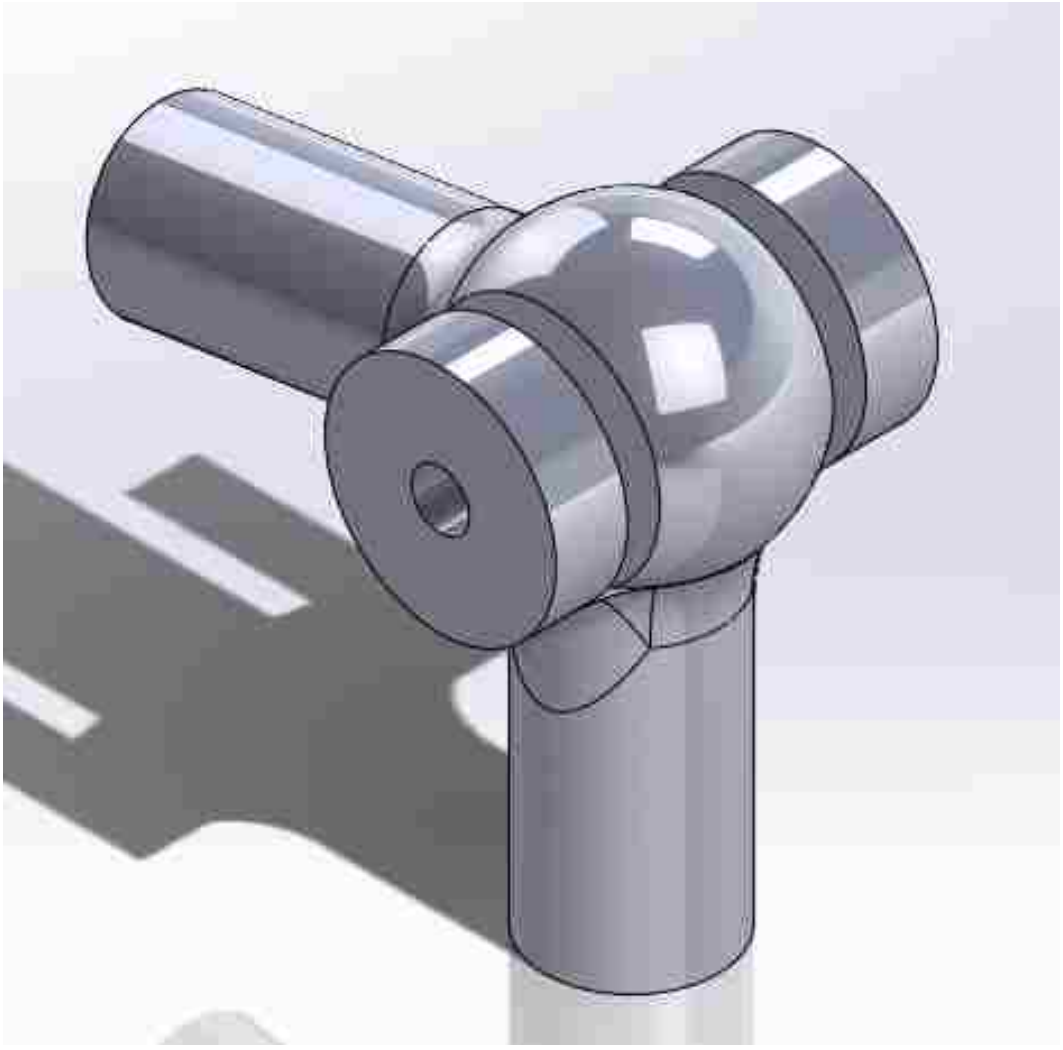

which is approximately 9.6% larger than the segmented wing. The wings have an effective aspect ratio of 5.76 with a span of 480 mm.

Chapter 3

Wind Tunnel Testing

3.1 Purpose and Goals

The experimental wind tunnel testing part of this project had three major goals:

1. Characterize the baseline aerodynamics of the GLUAS
2. Identify design parameters that can be improved/optimized
3. Quantify the propeller effects on the baseline model aerodynamics

Schutter, in his research, focused on Goal 1, and characterized the aerodynamics of scaled down models with segmented wings, in addition to testing the effects that the spreading out of the segmented wings had on the overall performance of the model (Schutter, 2016). Thus, for this project, it was decided to focus attention on Goal 2, identifying design parameters that could be improved.

The main design parameter of interest selected for this study was the sweep angle of the wing. The sweep angle was selected because it is easily changed on the current GLUAS model without requiring any significant design work.

In addition to sweep angle, a smaller study was performed to examine the effect of flexibility. A flexible PLA wing was tested in comparison to a rigid aluminum wing of the same dimensions, and further a membrane wing model was tested. Schutter's results seemed to indicate that flexibility improved wing efficiency in the case of the segments being restricted vs. being allowed to spread out.

Further, testing a flexible plastic wing would allow for a more thorough analysis of future results taken using models with segmented plastic wings, which are the wings currently in use on the Model 5 GLUAS. By first examining the difference between metal and plastic wings, the confounding effect of the flexibility of the wing could be potentially controlled, and a direct comparison made between flat plates and segmented wings.

No significant tests or experimental design work were directed towards Goal 3. This remains to be examined as part of a future research project.

Figure 3.1: The CAD diagram used to create the modified Δ-wings.

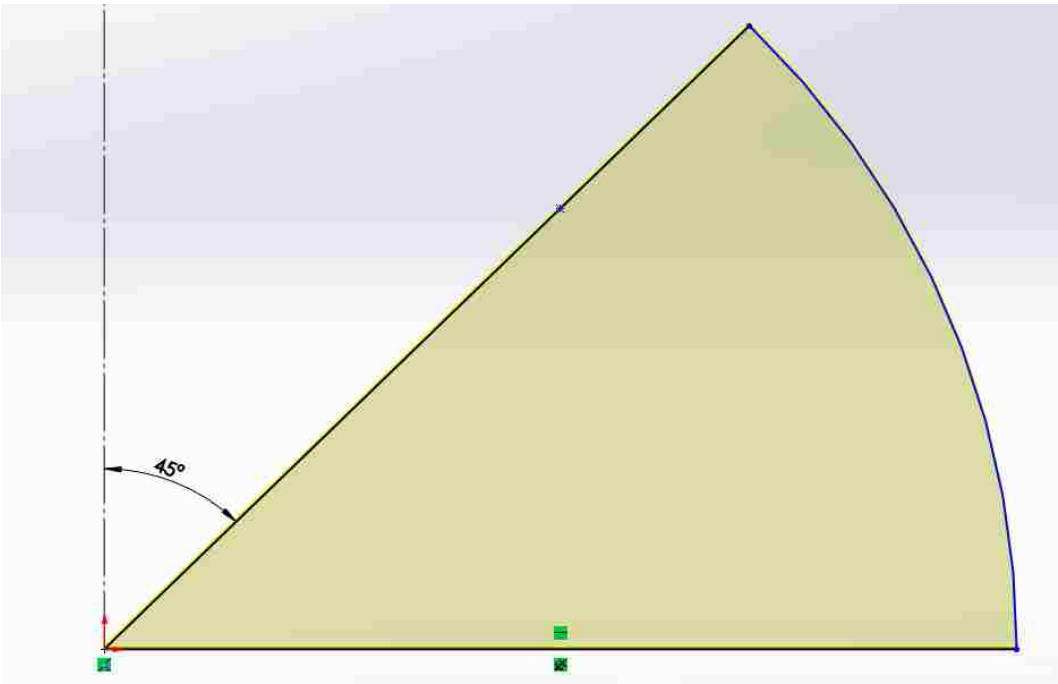

3.2 Experimental Design

3.2.1 Physical Design

Wing Design

The test wings used in this experiment are modified Δ-wings, with the trailing edge defined as an arc, rather than a straight line. This design approximates the planform shape of the GLUAS, without containing wing segments. By examining wings of this design, a basis for comparison can be established against which the segmented wings can be compared, to determine whether the segments are aerodynamically different from a flat plate.

All wings used in this study were made from water-cut aluminum (rigid case) or 3D printed PLA (flexible case). They all share a root chord length of 200mm, and were created from the model shown in Figure 3.1 by adjusting the sweep angle.

Metal wings were produced with sweep angles of 5, 15, 25, 35, 45, 65 degrees, and plastic wings were produced with sweep angles of 5 and 45 degrees.

In addition, a wing constructed from a latex sheet laid across several mounting spars was tested. This wing is shown in Figure 3.2.

Geometric Calculations For many of the calculations performed throughout this project, various geometric descriptions of parameters of the wing model used were required. Luckily, this wing geometry is very easily described, and is fully defined by only its root chord, and its sweep angle.

The formula for the area of this wing was derived by noting that the wing occupies a section of a circle, with a radius equal to the root chord. Because the sweep angles all fall within a quarter-circle, the area of a quarter-circle with this radius was calculated,

$$A = \frac{1}{4}\pi C_r^2 \tag{3.1}$$

and then the fraction of this area occupied by the wing was calculated using the sweep angle, and multiplied by the total area, in order to obtain the wing surface area,

$$S = A\left(\frac{90-\Lambda}{90}\right) = \frac{\pi C_r^2}{4}\left(\frac{\theta}{90}\right) \tag{3.2}$$

where $\theta = 90 - \Lambda$.

Another important parameter of the wing design is the wingspan: the longest distance between the wingtip and the root of the wing. This value can be easily calculated using trigonometry by assuming the wing to be a right triangle with a hypotenuse of length C_r. Applying this methodology gives the following,

$$\sin\theta = \frac{s}{C_r} \tag{3.3}$$

$$s = C_r \sin\theta \tag{3.4}$$

Finally, the aspect ratio of the wing is given by the formula

$$\mathrm{AR} = \frac{s^2}{S} = \frac{C_r^2 \sin^2\theta}{\frac{\pi C_r^2}{4}\left(\frac{\theta}{90}\right)} = \frac{360 sin\theta}{\pi\theta} \tag{3.5}$$

Membrane Wing Geometry The membrane wing model has a different geometry to the other wings, and is shown in Figure 3.2. The wing is most closely approximated by a trapezoid, the area of which is given by,

$$A = h\frac{b_1 + b_2}{2} \tag{3.6}$$

where h is given by the root chord, b_1 by the span, and b_2 by the length of the trailing edge. This results in the following,

$$S = C_r\frac{s + s_t}{2} \tag{3.7}$$

and

$$\mathrm{AR} = \frac{s^2}{C_r\frac{s+s_t}{2}} = \frac{2s^2}{C_r(s + s_t)} \tag{3.8}$$

Figure 3.2: A picture of the membrane wing test model.

Wing Design Parameters Based on the geometric formulae previously described, and physical measurements of the wings for both length and mass, the values for the weight, span, area, effective aspect ratio, etc. were determined. The values of these parameters are given in Table 3.1.

One relation between the parameters that is of particular interest is the relationship between the sweep angle of the wing, and its weight. This relationship was shown to have a significant effect on the range and endurance of the aircraft for a given wing. Excluding the plastic and membrane wings, as these have very different material properties when compared to the rigid metal wings, Figure 3.3 describes the relationship between these two properties. Note that the relationship is very linear, with a coefficient of determination of $R^2 = 0.97$.

Figure 3.3: Test Model Weight vs. Wing Sweep Angle (rigid metal wings)

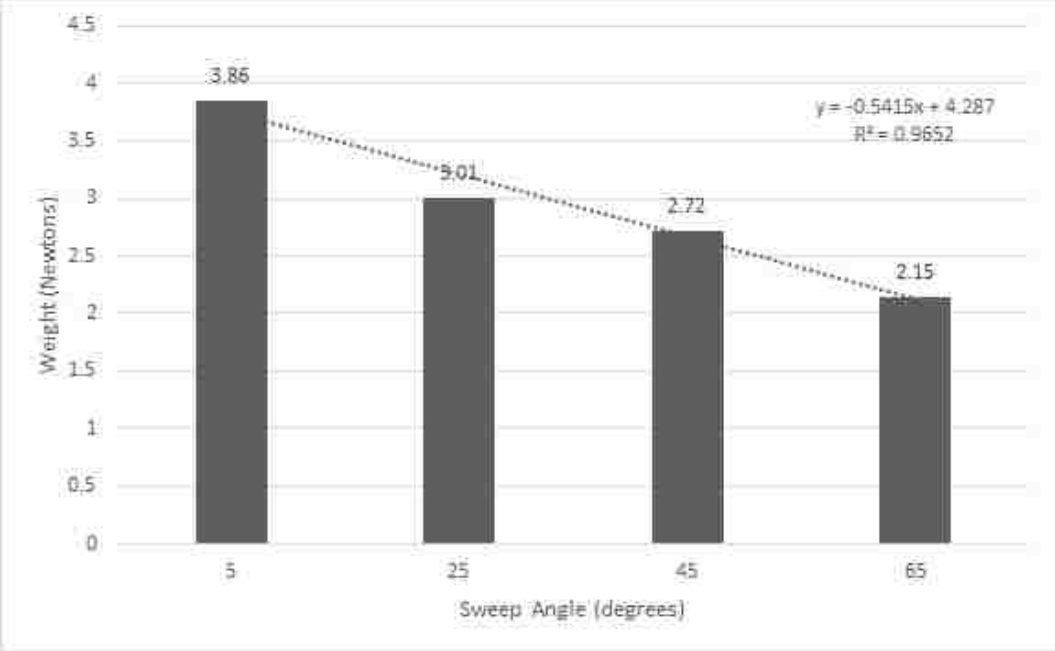

Table 3.1: The values of various wing design parameters.

Wing	**Test Model Weight**	**Wing Area**	**Span**	**Aspect Ratio**
5 Degree Rigid	3.86 N	0.030 m^2	0.20 m	2.68
25 Degree Rigid	3.01 N	0.023 m^2	0.18 m	2.90
65 Degree Rigid	2.15 N	0.0087 m^2	0.085 m	1.64
45 Degree Rigid	2.72 N	0.016 m^2	0.14 m	2.55
45 Degree Flexible	1.95 N	0.016 m^2	0.14 m	2.55
Membrane	1.93 N	0.026 m^2	0.17 m	2.22

Experimental Model

The experiment was designed so as to yield general results, and to be easy to modify to accept a wide variety of wings. In order to accomplish this design, a rough approximation of the GLUAS fuselage, without any of the protrusions of other elements unique to the GLUAS itself, was created in SolidWorks. This model was designed with deep sockets where screws are used to mount it, so

Figure 3.4: Profile views of the test model used for wind tunnel testing.

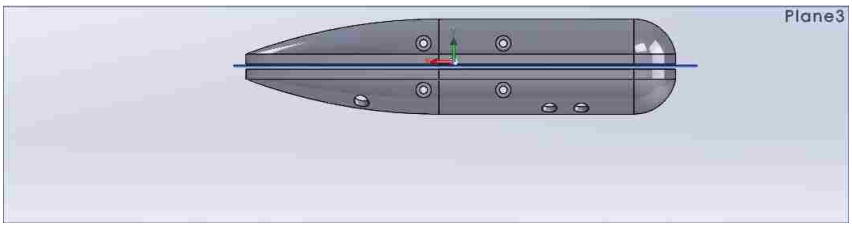

(a) Front view of the test model

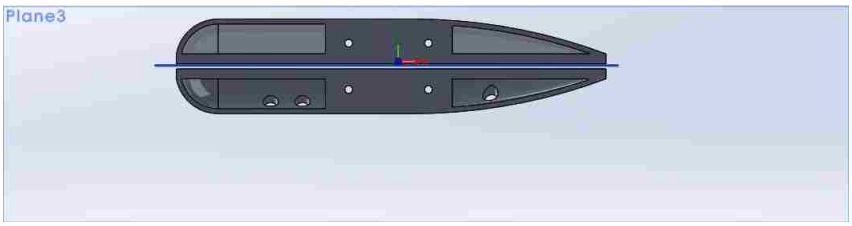

(b) Rear view of the test model

that there are no screws protruding out into the flow during testing. Figure 3.4 shows front and rear views of this test model.

Wings can be attached to this model using three M3 screws, which attach from the top[1]. In the physical model (which was 3D printed using ABS), modified tee-nuts are used within the model to reinforce these attachment points with metal threads. Should spacing be required to ensure that the wing is held tightly, M3 washers can be easily used.

The four holes running perpendicularly through the plane of the model are for use in attaching the model to the mounting plate (which is itself attached to the force sensor). It was decided to use an intermediate mounting plate for the model to help damp any internal tensions within the model, so that they

[1]In the initial model, which was used to collect some of the rigid-wing data, the screws attached from the bottom. This was changed to avoid the potential for a screw to fall out of the model and into the wind tunnel were it to come loose.

are not measured by the force sensor itself. This decision also makes it a lot safer to attach the model to the force sensor, as the plate can be attached to the force sensor before it is mounted in the wind tunnel, whereas the model must be attached once the sensor is in the wind tunnel (which is not a simple task, depending on the attached wing).

The test model to be used has undergone extensive revision over the course of this project. Appendix C.1 details past model and wing designs.

Wind Tunnel Test Section

The wind tunnel itself is set up as shown in Figure 3.6. In order to reduce noise, the Sensor Retaining Ring, and Sensor Mounting Plate were both made out of aluminum. The Back Plug is made of acrylic and fits into a hole in the wind tunnel wall. The entire force sensor assembly (back plug, mounting plate, retaining ring) is one unit, and can be removed from the tunnel. This assembly also rotates freely, in order to adjust angle of attack. A digital level and bracket are used to ensure that the angle adjustments are precise to within .1 degrees.

The Model Mounting Plate (Figure 3.5) is made of 3D printed PLA plastic, with M3 tee-nuts used for the holes into which the model is secured, and through-holes used to attach to the force sensor. Through-holes, rather than threaded holes, were used so as to reduce the amount of torque required to fasten the plate onto the sensor. This was a measure taken to protect the sensor from being over-torqued and damaged, as it is very torque sensitive.

The splitter plate is used in order to reduce boundary layer effects along

Figure 3.5: Model Mounting Plate

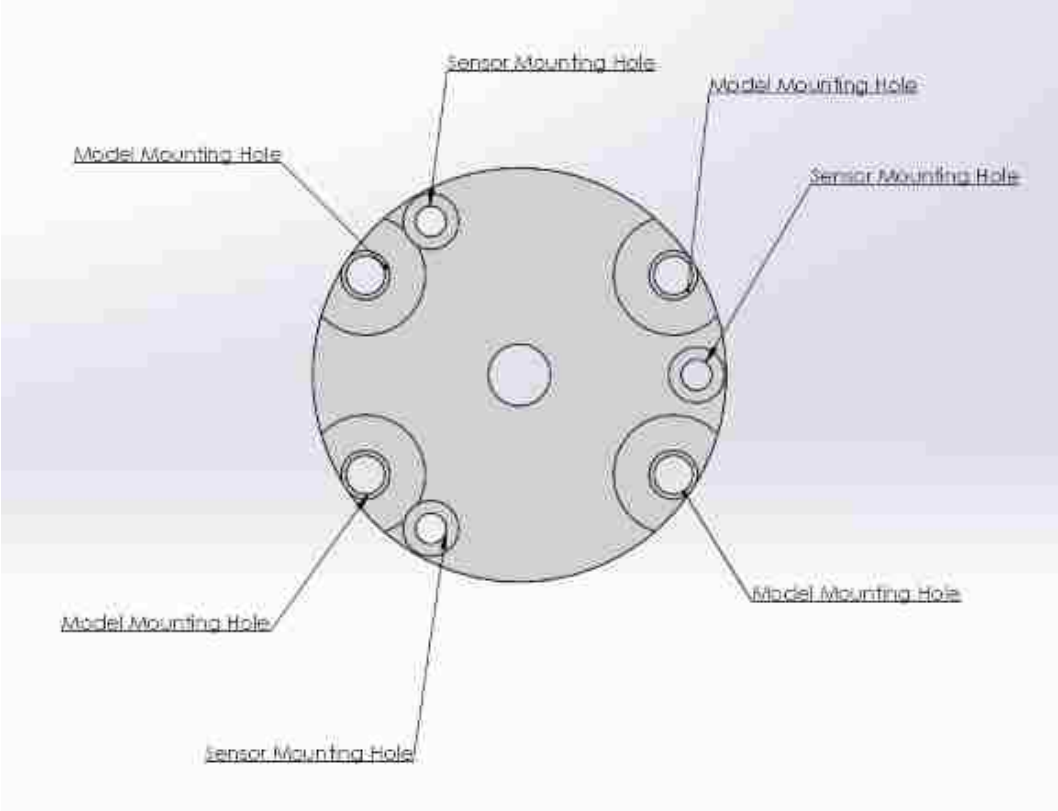

the tunnel wall. It is necessary because of how close to the wall the test model is mounted.

Data was collected using an ATI Nano-43 6-axis F/T Transducer in the SI-9-0.125 calibration. This transducer was connected to a National Instruments CompactRIO data acquisition system, controlled using National Instruments LabView. LabView was used to apply a 20Hz low-pass filter on the force sensor output, in order to reduce the effects of electrical noise, and also to handle the angular manipulations required to obtain lift and drag numbers from force data on the sensor's x and y axes. The angular manipulations are described in Section B.1. Lift was measured from the sensor's positive y axis, and drag

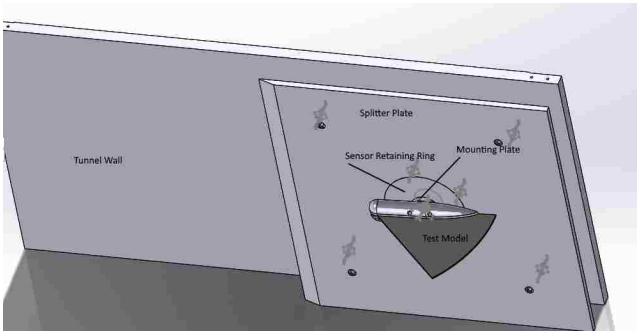

(a) A front view of the wind tunnel setup.

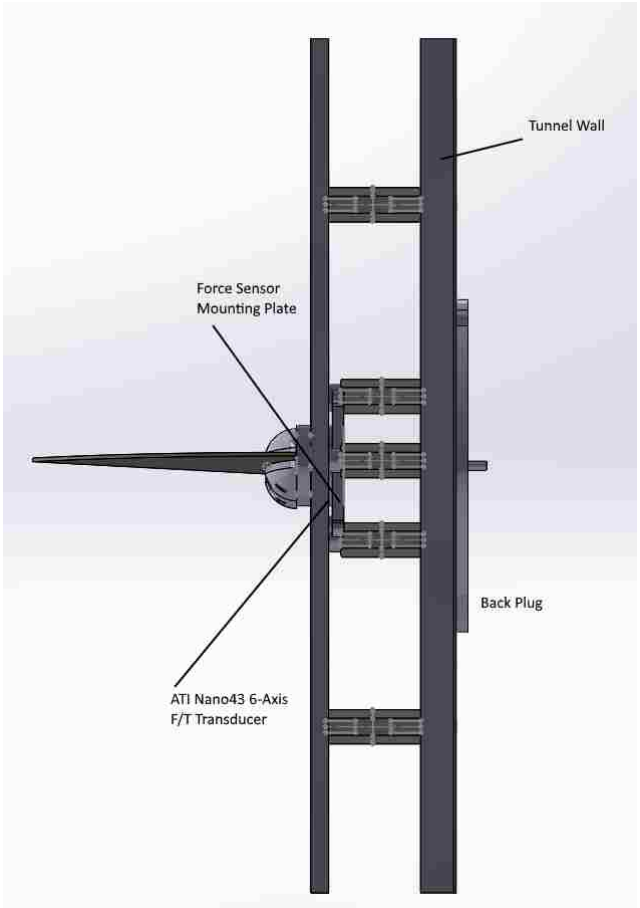

(b) A side view of the wind tunnel setup.

Figure 3.6: Front and side views of the wind tunnel setup

from the negative x axis.

3.2.2 Experimental Procedures

For each trial, the same procedure was used. The force sensor assembly was mounted in the wind tunnel, with the force sensor aligned such that, at zero angle of attack, lift was measured on its y-axis and drag was measured on its negative x-axis. Then, the model was assembled with the wing of choice, and bolted onto the force sensor assembly using the mounting plate.

A digital level was placed on the wing, and used to align it to 0 degrees (within ± 0.1 degrees). The wind tunnel was turned on, and left to run for thirty minutes, to allow the air temperature within the tunnel to reach equilibrium and avoid any convection effects while taking data.

Once the temperature had equalized, the wind tunnel was turned off. The force sensor was tared using LabView, in order to remove weight effects and to ensure that the only forces measured were aerodynamic in origin.

Once the force sensor was tared, the wind tunnel was run at 27.7 Hz[2] and LabView was used to collect data. The data was output from LabView in the form of a running average, and the lift and drag numbers were recorded once this average had stabilized for at least 15 seconds in all but the third decimal place.

Once the data was recorded, the wind tunnel was shut off. Using the level, the angle of attack of the model was increased, and the procedure repeated.

[2]This frequency was obtained through linear interpolation of the calibration curve, in order to obtain a chordwise Reynolds number of $2*10^5$, the Re_c associated with the estimated top speed of the current GLUAS design

The exact angles of attack, and the increments therein, varied slightly over the period of data collection, as a better understanding of the lift curves to be expected was developed.

In the end, data was collected in 1 degree increments from $\alpha = 0$ to $\alpha = 20$, and then two additional points were taken at $\alpha = 25$ and $\alpha = 30$. This procedure was used for data collection for the rigid and semi-flexible (plastic) wings.

For data collection for the membrane wing, a slightly different procedure was applied. Data was collected at $\alpha = 0$, and then in 1 degree increments from $\alpha = 3$ to $\alpha = 9$. After this, it was collected in 3 degree increments up to $\alpha = 21$. Also, for the membrane wing, data was collected at a Reynolds number of 1.25×10^5, due to fears of the membrane tearing free from the model at higher freestream velocities.

This procedure was repeated between 3 and 5 times for each wing, disassembling and reassembling the model between runs to ensure statistical independence. The results were then tabulated. All data reported in this document are the results of the averages of the trials for each wing.

3.3 Results

Figure 3.7: PIV Data for 5 degree Sweep, $\alpha = 0$

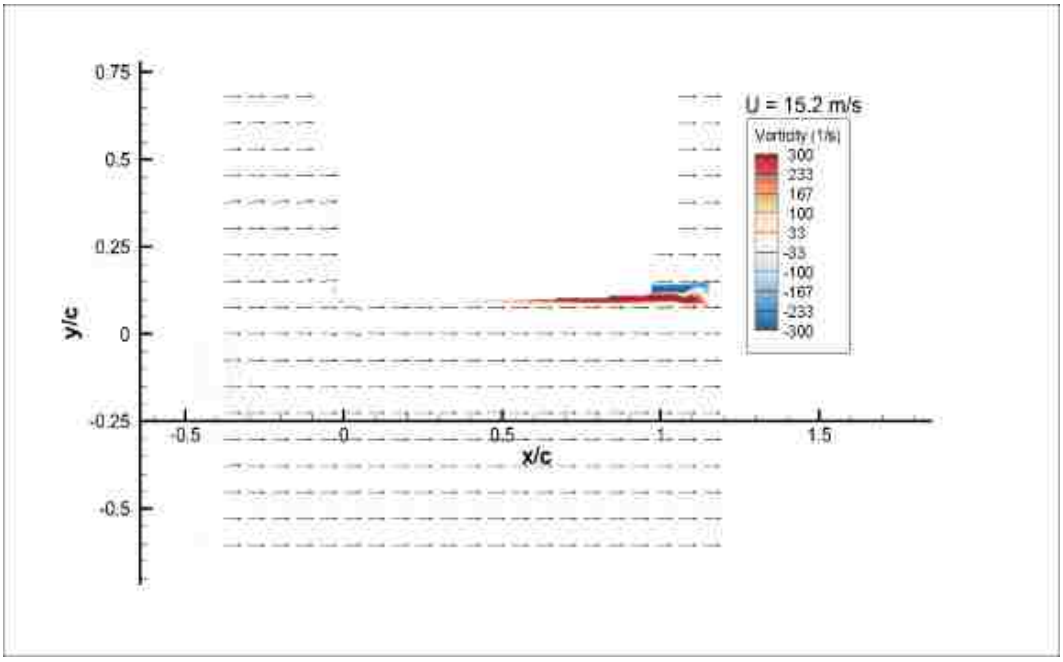

Figure 3.8: PIV Data for 5 degree Sweep, $\alpha = 3$

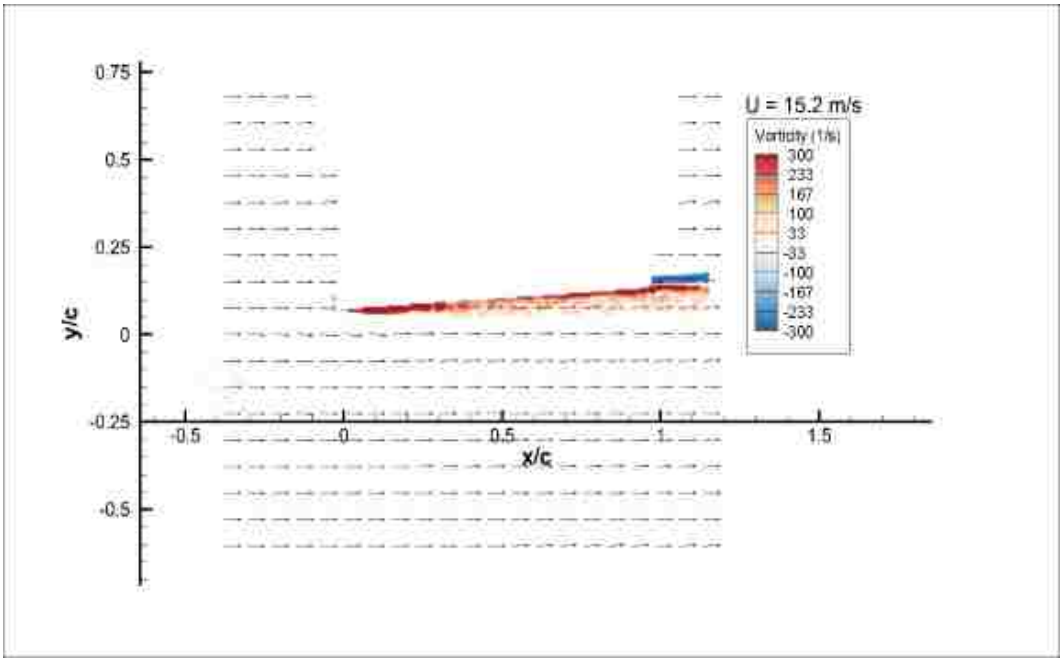

Figure 3.9: PIV Data for 5 degree Sweep, $\alpha = 5$

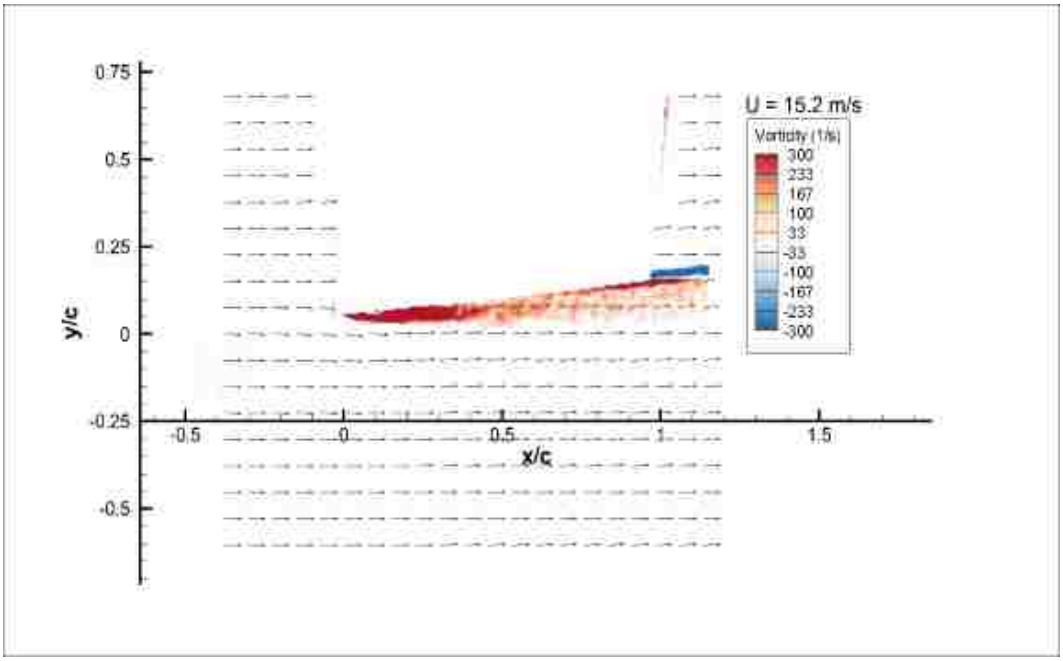

Figure 3.10: PIV Data for 5 degree Sweep, $\alpha = 10$

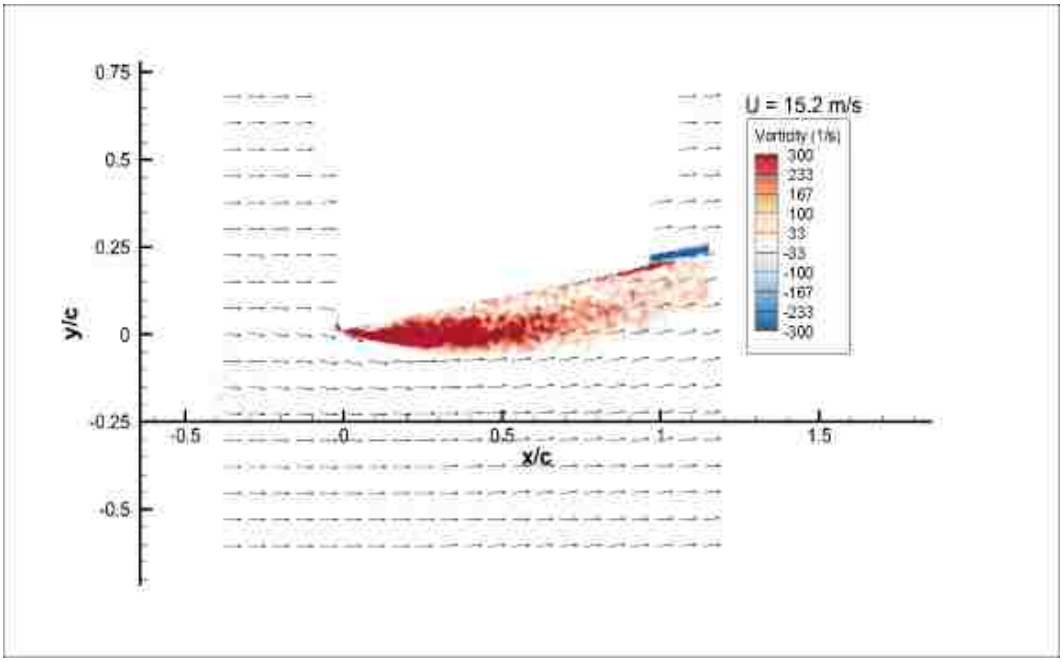

Figure 3.11: PIV Data for 5 degree Sweep, $\alpha = 15$

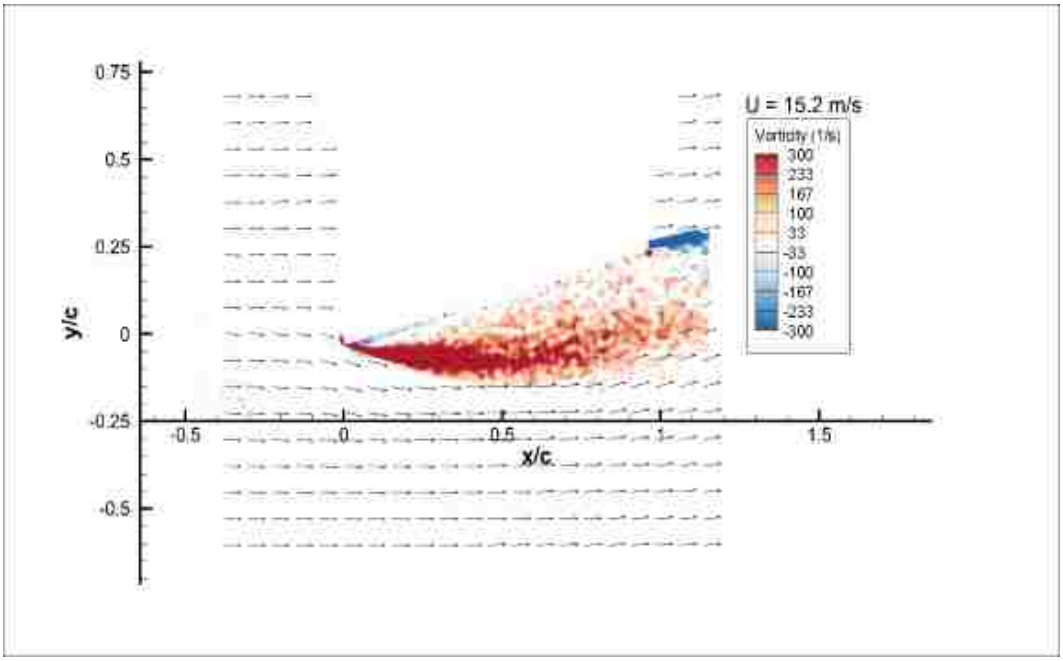

Figure 3.12: Maximum Coefficient of Lift vs. Wing

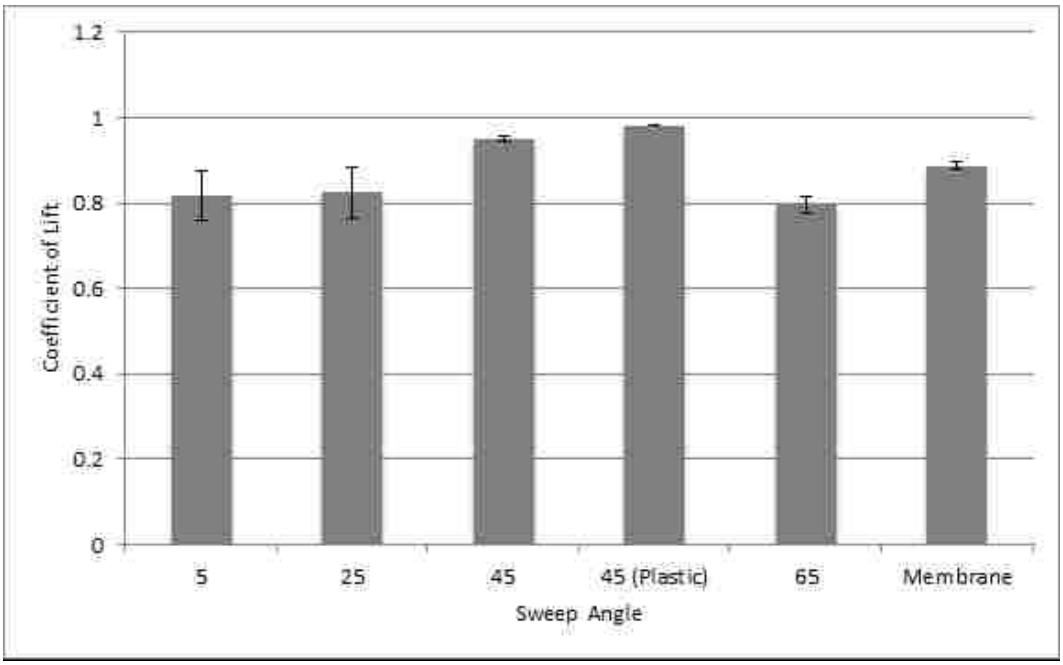

Figure 3.13: Maximum Lift to Drag Ratio vs. Wing

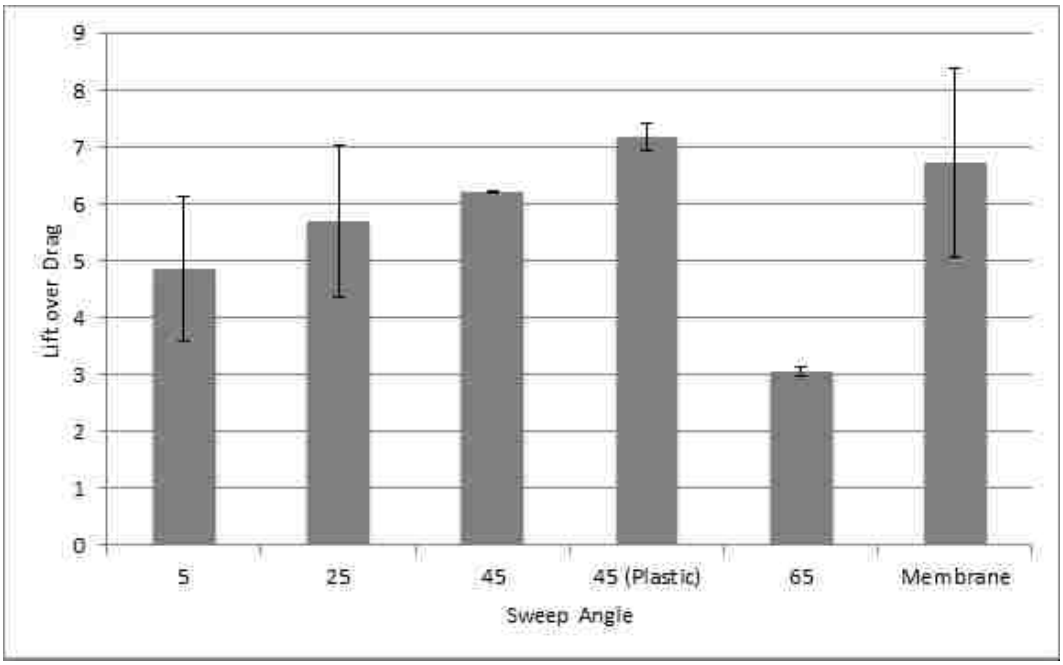

Figure 3.14: Maximum Endurance vs. Wing

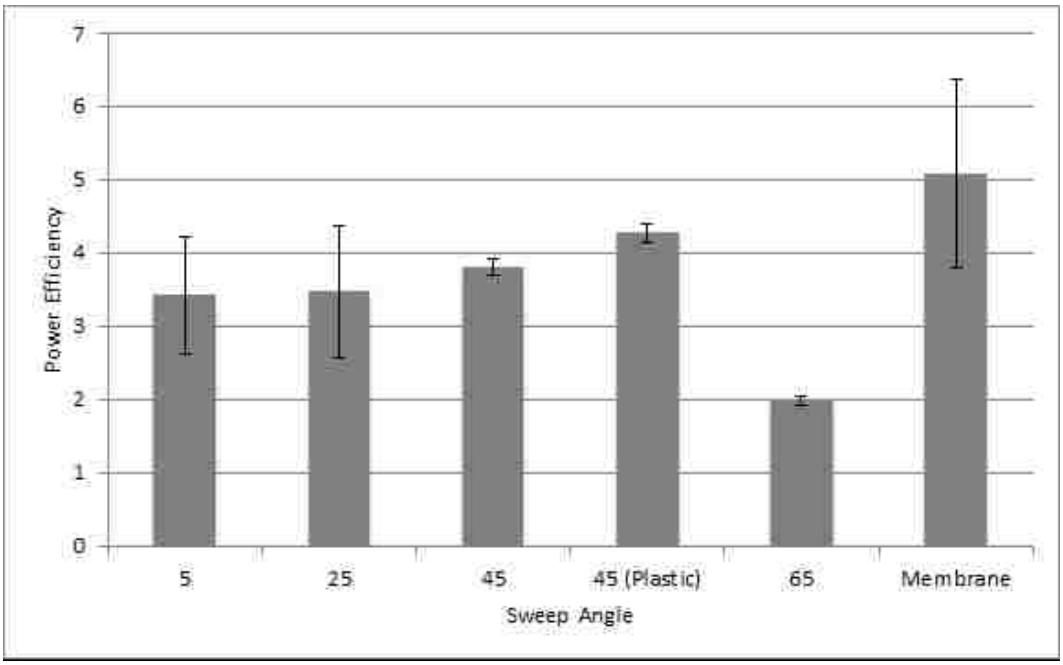

Figure 3.15: Lift Curves for Rigid Wings

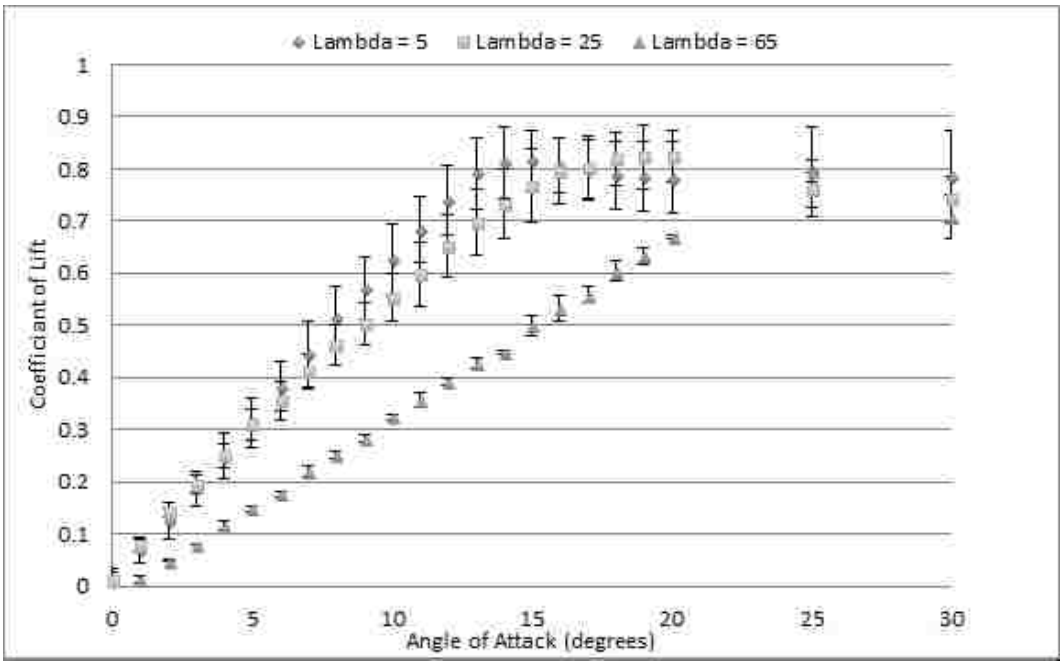

Figure 3.16: Drag Curves for Rigid Wings

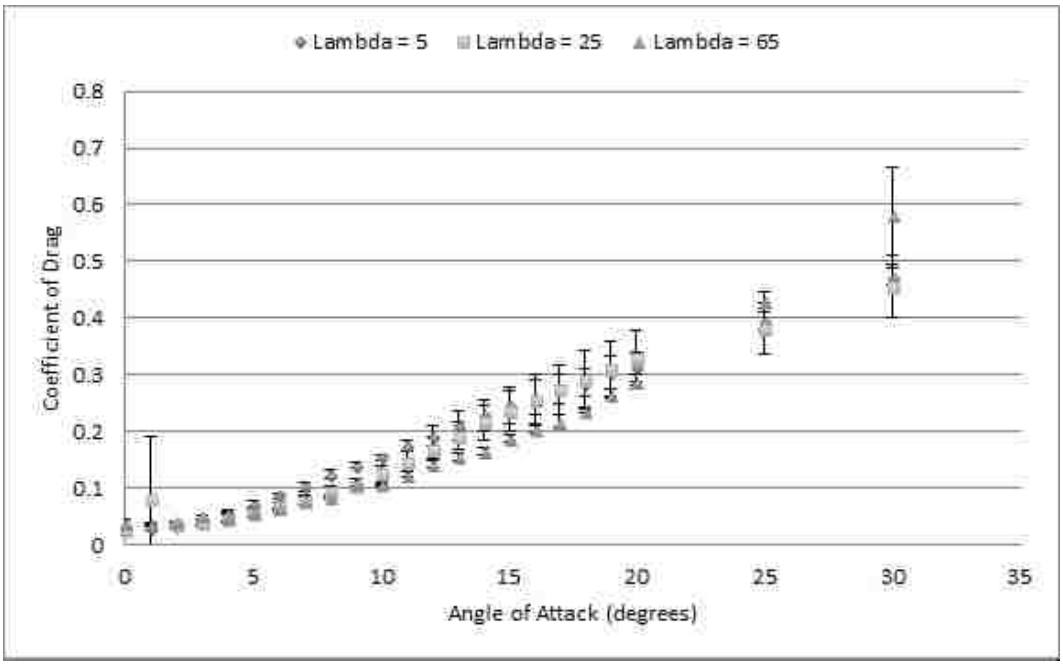

Figure 3.17: Lift to Drag Curves for Rigid Wings

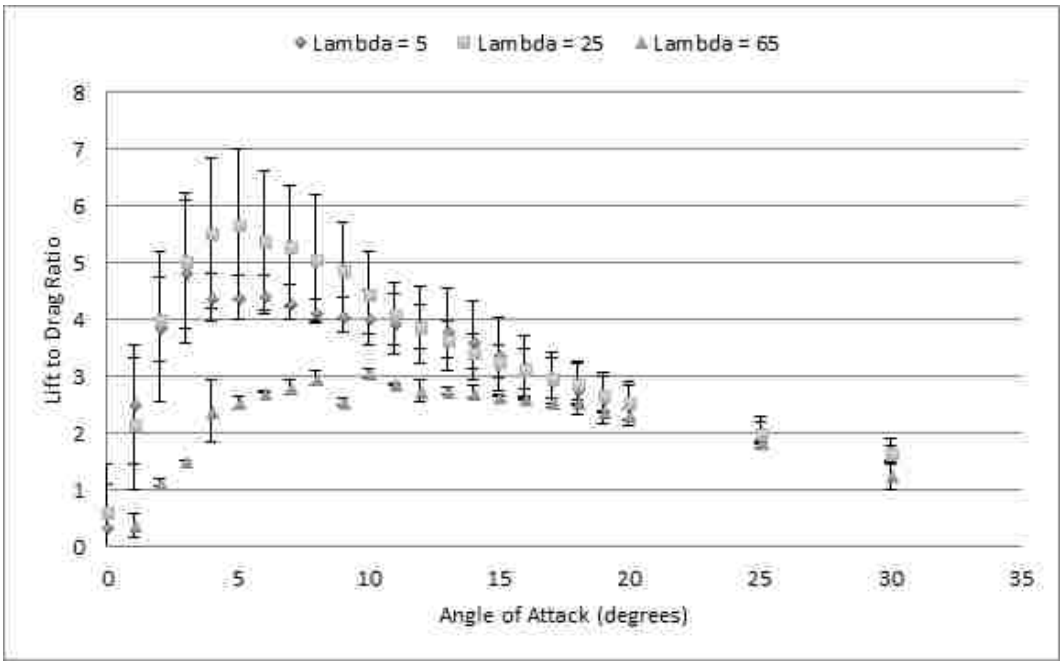

Figure 3.18: Endurance Curves for Rigid Wings

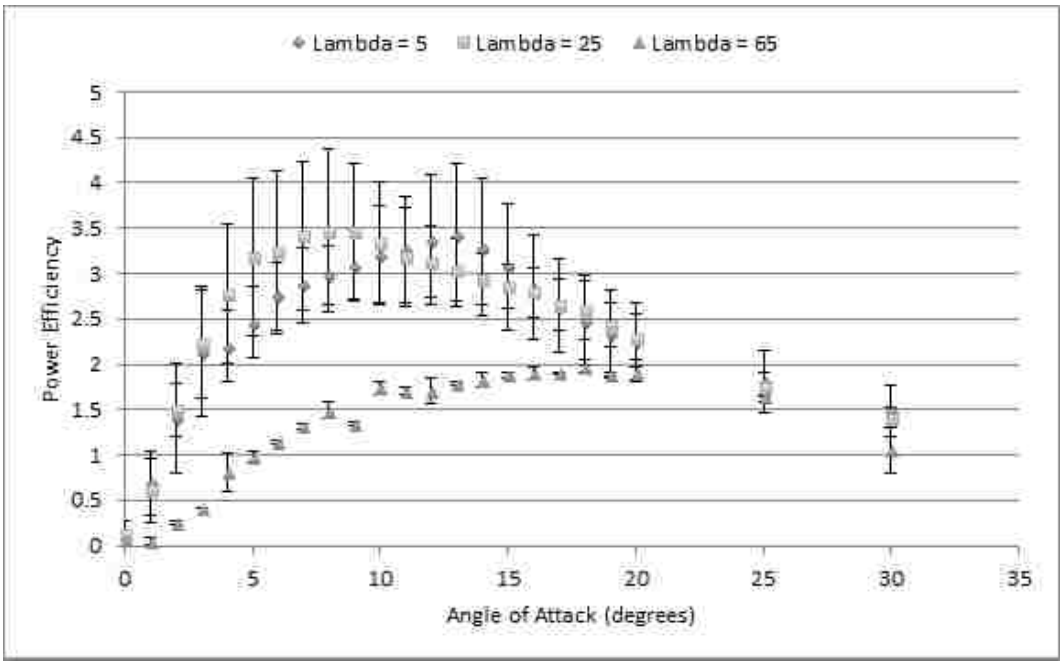

Figure 3.19: Lift Curves for 45 Degree Wings

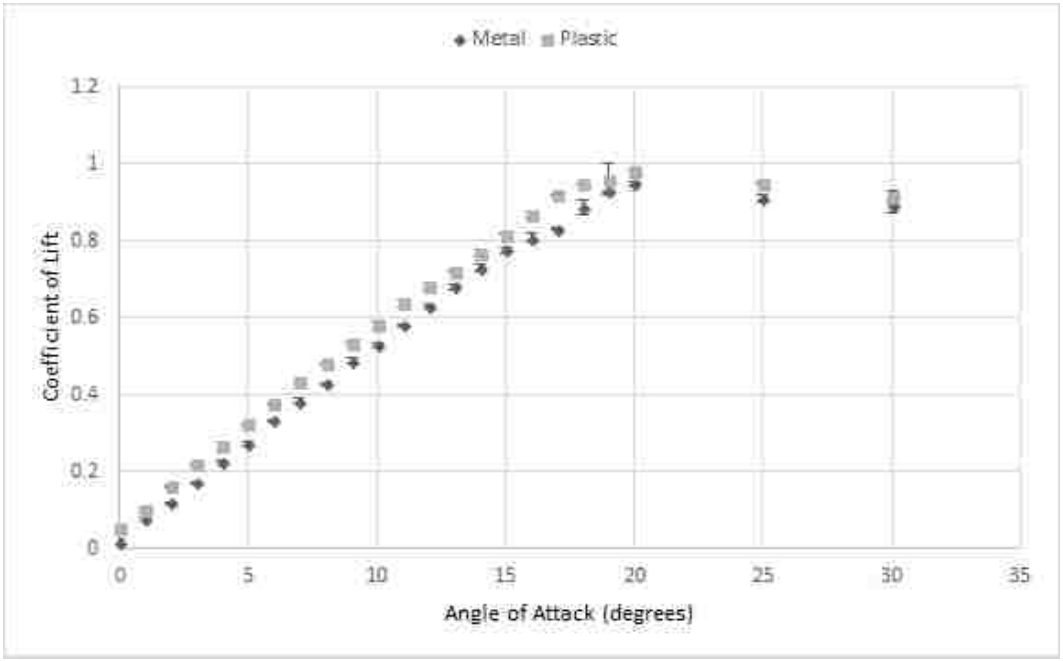

Figure 3.20: Lift to Drag Ratio for 45 Degree Wings

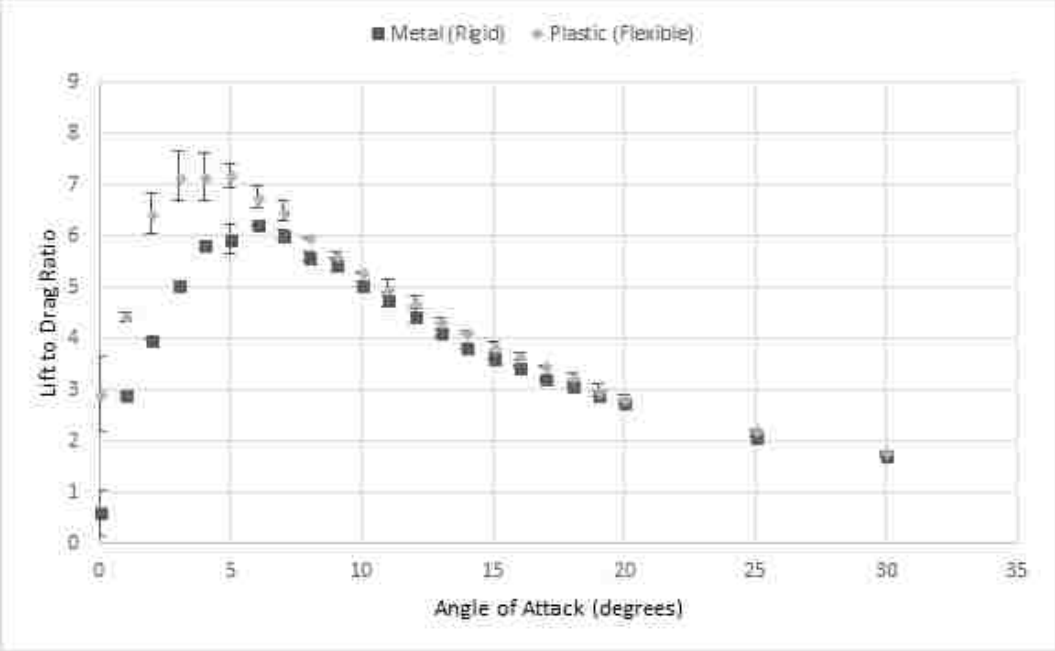

Figure 3.21: Endurance for 45 Degree Wings

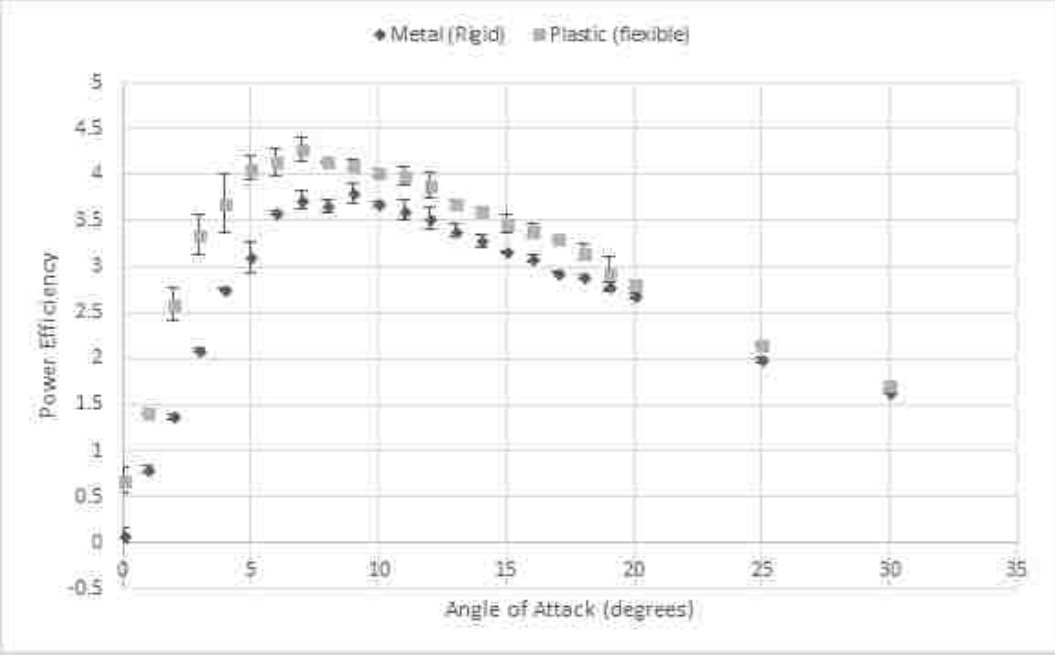

Figure 3.22: Lift Curve for Membrane Wing

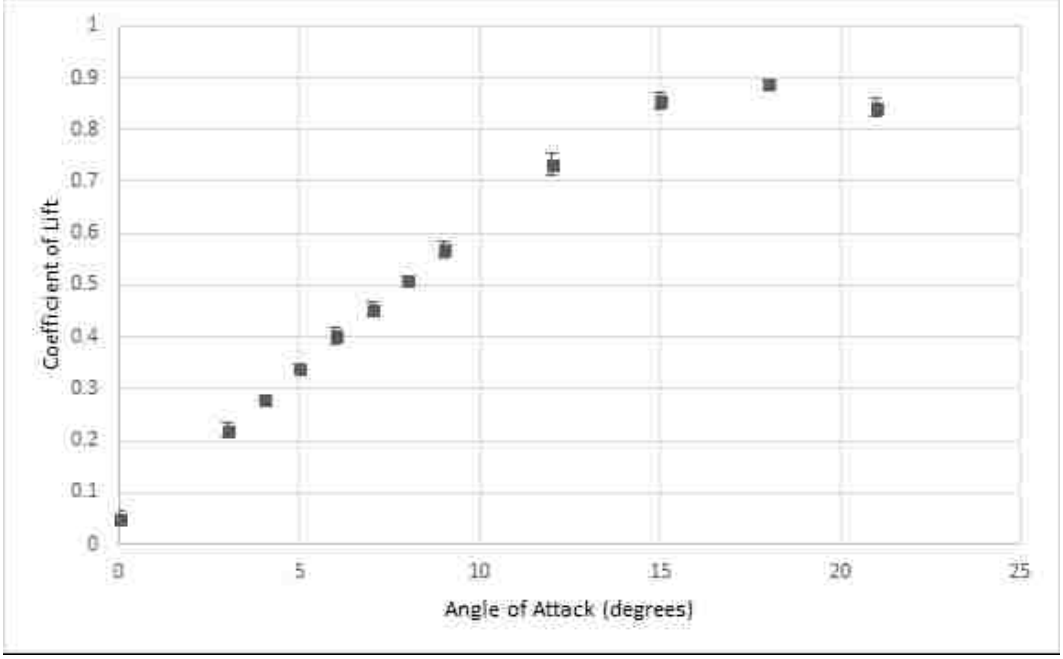

Figure 3.23: Drag Curve for Membrane Wing

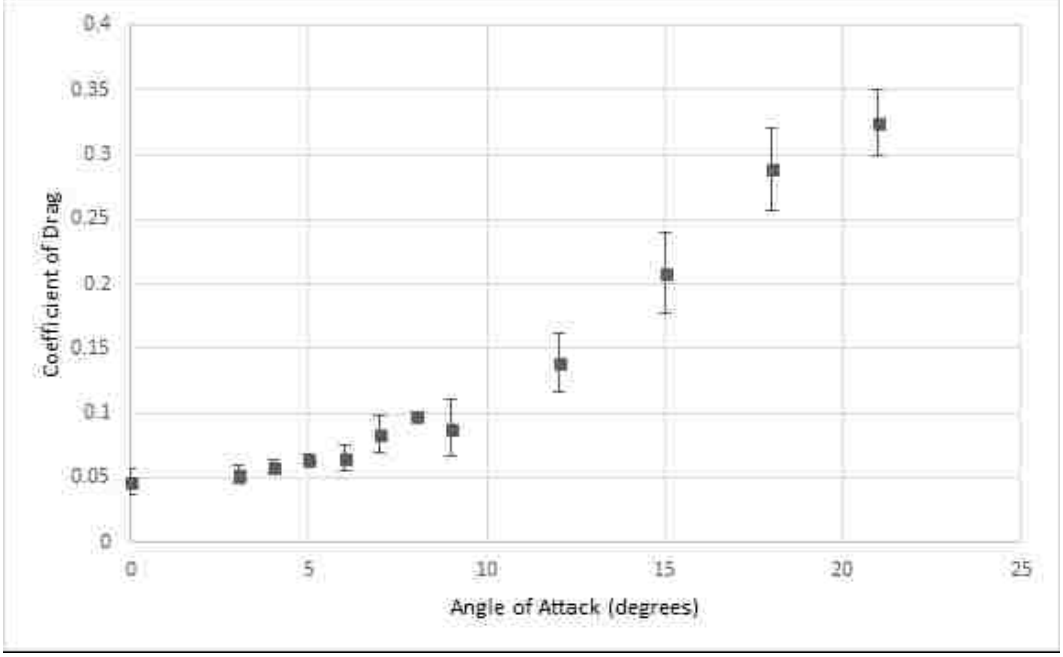

Figure 3.24: Lift to Drag Ratio for Membrane Wing

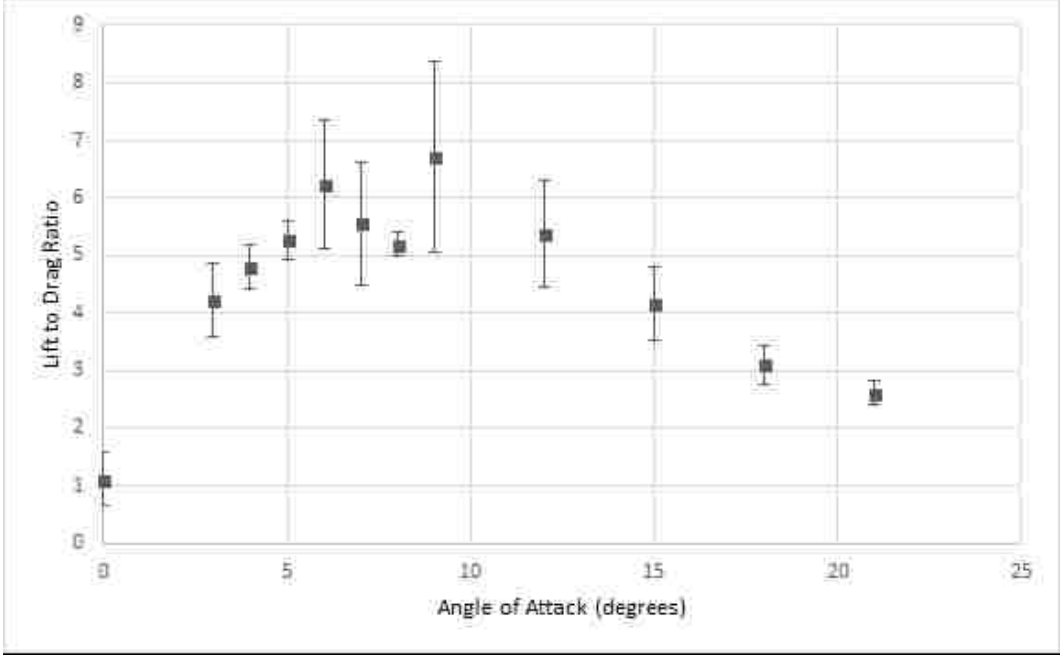

Figure 3.25: Endurance for Membrane Wing

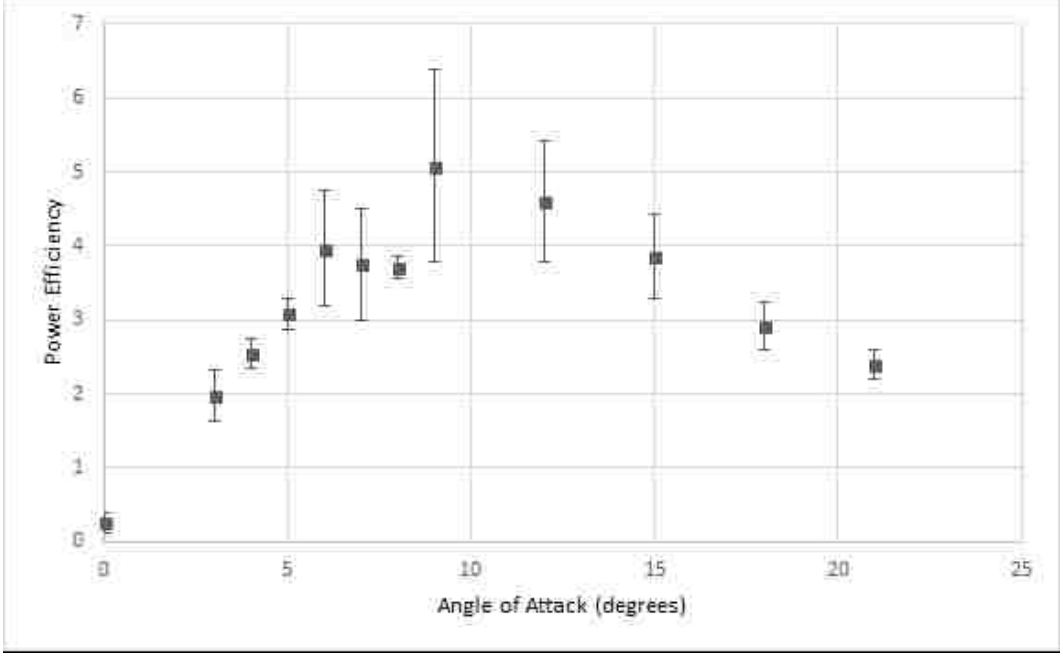

Figure 3.26: Angle of Attack for Peak Lift to Drag/Endurance

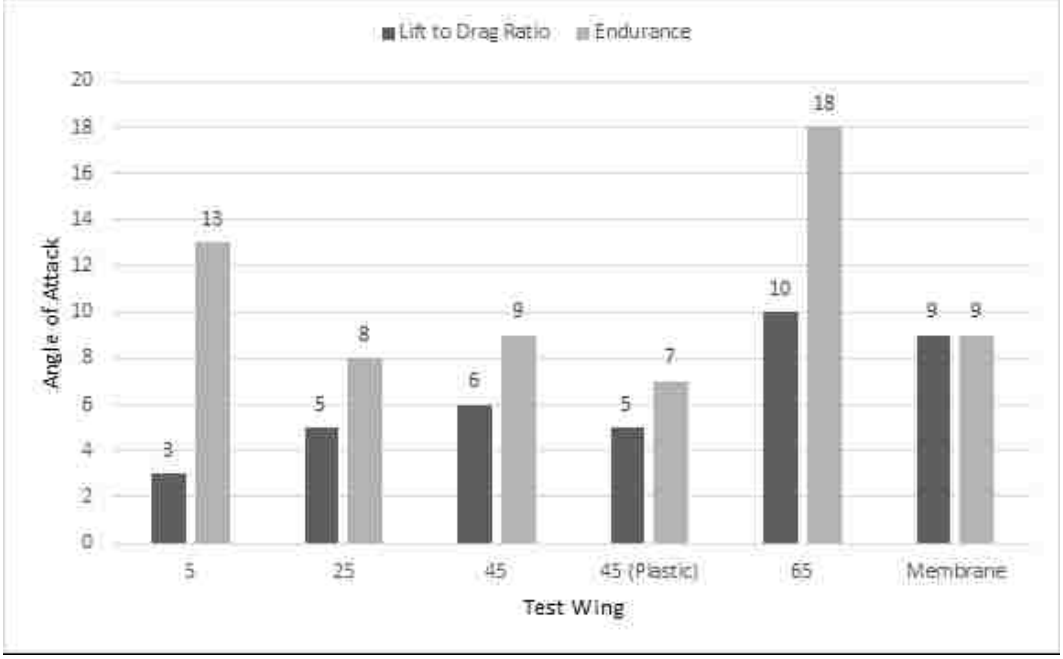

Figure 3.27: Theoretical Range vs. Wing

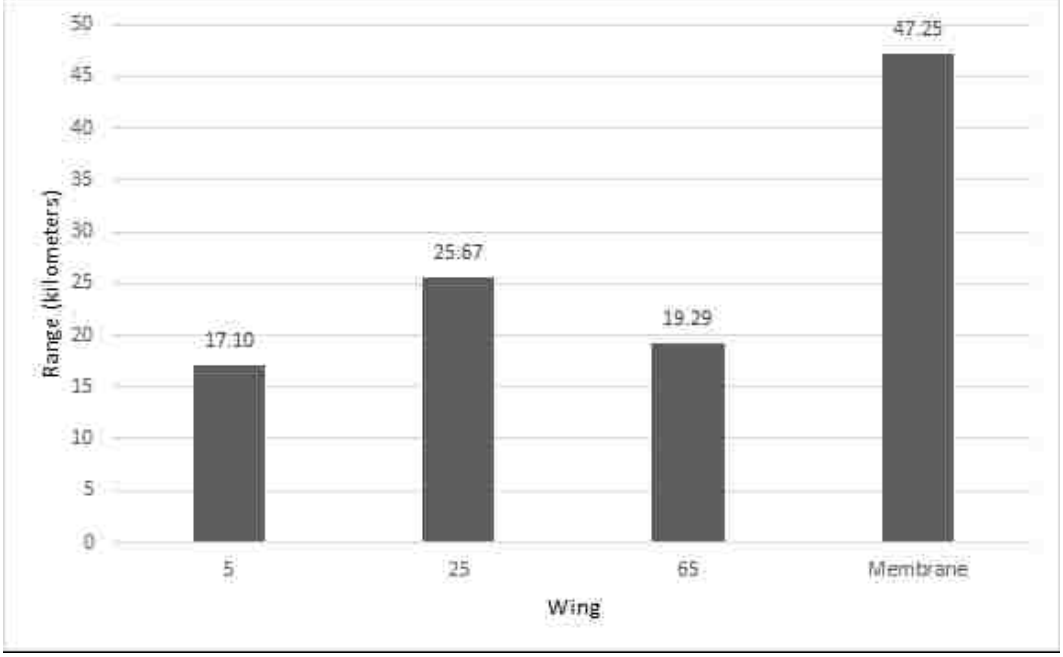

Figure 3.28: Theoretical Endurance vs. Wing

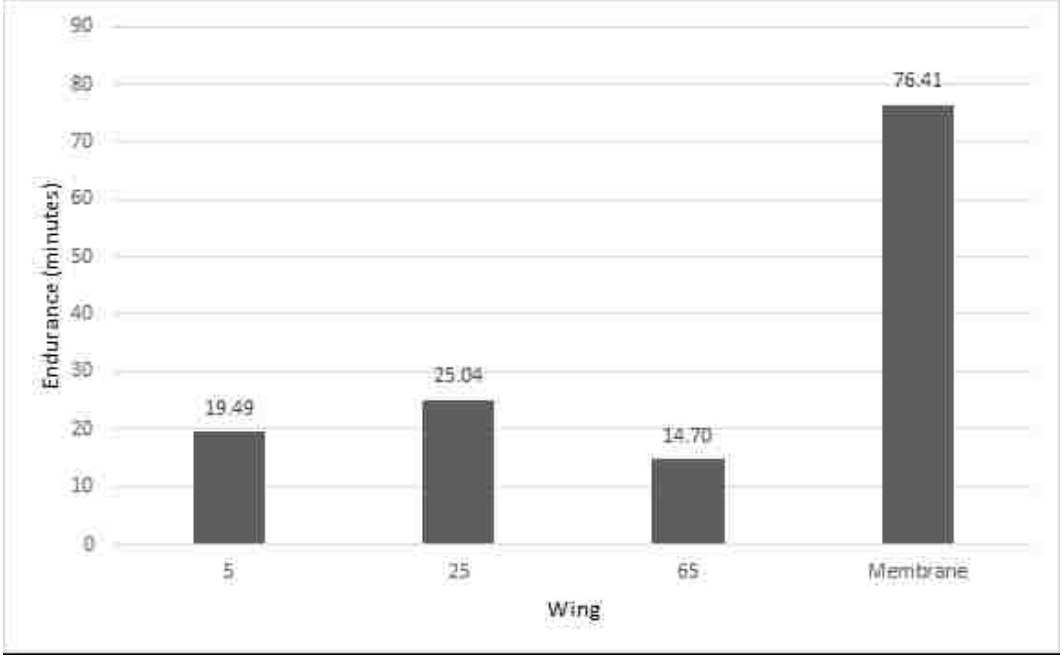

Table 3.2: Maximum C_L at 90% Confidence

Wing	$C_{L,max}$ at 90% Confidence
$\Lambda = 5$	(0.78, 0.86)
$\Lambda = 25$	(0.77, 0.87)
$\Lambda = 65$	(0.79, 0.82)

3.4 Discussion

3.4.1 Rigid Wing Results

The lift curves for the 3 main rigid wings that were tested is given in Figure 3.15. These curves show that, as the sweep angle of the wing is increased, the angle of attack at which the wing enters dynamic stall is also increased. The $\Lambda = 5$ wing reaches peak C_L at $\alpha = 15$, the $\Lambda = 25$ at $\alpha = 19$, and the $\Lambda = 65$ at $\alpha = 25$. This data seems to indicate that it would be desirable, in order to delay stall, to use a highly-swept wing.

Further, the peak C_L for all three wings are identical to within a statistical margin of error, as shown in Figure 3.12. Specifically, the 90% confidence intervals for $C_{L,max}$ are given in Table 3.2. As can be seen, these intervals overlap significantly, however there does seem to be indication that the $\Lambda = 65$ performs slightly worse in terms of overall lift generation.

With that said, the dimensional lift forces differ quite significantly as a result of the wildly different planform areas possessed by each wing (see Table 3.1). One potential concern that should be addressed is whether or not the wings, even though they possess the same C_L, produce enough dimensional lifting force at the tested flight speed to ensure that the projectile is capable

Figure 3.29: L^* vs. Angle of Attack

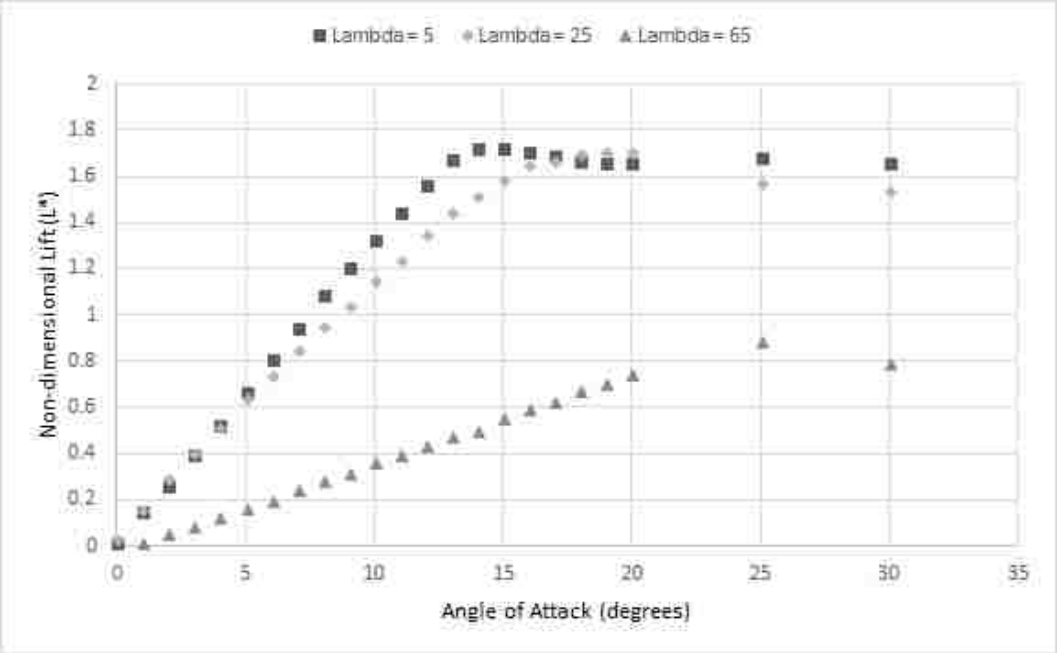

of flight.

To this end, a new non-dimensional lift, L^*, is defined as follows,

$$L^* = \frac{L}{W} \tag{3.9}$$

where L is the dimensional lift force, and W is the weight of the test model. Note that the values provided in Table 3.1 are for a full wing, not the half-wing tested. As such, the dimensional lift force values have been doubled for this analysis under the assumption that the planform is symmetric and that the full planform has the same C_L as half of the planform, thus resulting in S being doubled, thereby doubling the lift force.

Figure 3.29 shows a plot of L^* vs. α for the three rigid wings. For values

of $L^* < 1$, the projectile is not generating enough dimensional lift to balance its weight, and thus will not fly. At $L^* = 1$, the forces of lift and gravity are perfectly balanced, and for $L^* > 1$, enough lift is produced to counteract gravity, resulting in a net upward force.

Both the 5 and 25 degree swept wings begin to have $L^* > 1$ at $\alpha = 8$, however the 65 degree swept wing never produces enough lift to balance out its weight. There is thus evidence to support that, within the low Reynold's number regime (10^5) in which the GLUAS is expected to operate, a highly swept wing would be impractical, as it would be difficult to produce enough lift to keep the projectile in the air.

Raw lift production, once the GLUAS is able to fly, is not quite as important as how long the projectile will be able to remain in the air, and how far it will be able to fly. For these efficiency measures, the lift-to-drag ratio and power efficiency must be examined.

The lift-to-drag ratio governs the flight range of an aircraft. Figure 3.17 shows the lift-to-drag curves for the three rigid wing cases and Figure 3.13 shows the maximum values for lift-to-drag ratio for each wing tested. Here, there is a statistically significant result in that 65 degree swept wing has a lower lift to drag ratio than the other two wings for small values of α. The remaining two wings have very similar lift-to-drag numbers, however, qualitatively, it does appear likely that the 25 degree swept wing has slightly better performance in this metric.

Power efficiency ($C_L^{3/2}/C_D$) tells a similar story. The power efficiency curves for the rigid wings are shown in Figure 3.18 and the maximum values in Figure

3.14. The 65 degree swept wing performs worse here, and the 5 and 25 degree wings are very close, with the 25 degree potentially having a small lead.

It is important to note, however, that the peak values of power efficiency and Lift-to-Drag do not necessarily occur at the same angle of attack. Having these values peak near to each other is beneficial, as it allows a median value for α to be selected so as to get both as near to the maximum as possible. The angles at which the respective peaks occur are given in Figure 3.26. The five degree swept wing has its peaks separated by 10 degrees of α, whereas the 25 degree swept wing's are separated by only 3 degrees. Thus, the 25 degree swept wing's lift-to-drag and power efficiency curves are more consistent with each other, which could allow for an angle of attack to be selected that would best optimized both values.

Figures 3.28 and 3.27 are plots of the theoretical range, in kilometers, and endurance, in minutes, for each test model based on their peak lift-to-drag and power efficiency respectively. These calculated values, for the most part, bear out the same distribution as the underlying aerodynamic parameters of the respective equations, however it is interesting the note that the 65 degree swept wing, despite having a much lower power efficiency than the 5 degree swept wing, actually has a higher predicted endurance. This is due to the fact that the higher sweep angle wings are smaller, and thus lighter, and this decreased weight has a larger effect on the endurance equation (being raised to the $3/2$ power) than in the range equation (where it is simply inversely proportional). The weight and surface area parameters used for calculating these values can be found in Table 3.1, and the battery-related parameters in

Table 3.3: Battery-related parameters used for calculating Range and Endurance for the test models. These values are reproduced from Schutter's thesis (Schutter, 2016).

Parameter	Symbol	Value
Efficiency	η	0.4
Battery Mass	m_{batt}	$0.63\,\mathrm{kg}$
Energy Density	E^*	$538\,\mathrm{kJ\,kg^{-1}}$

Table 3.3.

PIV Data

In addition to force measurements, PIV data was taken for the 5 degree swept wing at several angles of attack, at the midspan. The time-averaged PIV images resulting from this are given in Figures 3.7 through 3.11. Red indicates positive vorticity, and blue negative. Notably, in this case, negative vorticity on the underside of the wing is indicative of stall.

Note that the wing here is pitching down, a constraint of the PIV setup used. The lower side of this wing, then, is the suction side and the upper is the pressure side. The results should be symmetrical, and thus the vortex formation on the bottom of the wing while pitching down should be the same as the vortex formation on the top of the wing pitching up.

A separation bubble begins to form at the leading edge of the wing at $\alpha = 10$, as shown in Figure 3.10. However, this region of separated flow reattaches fairly quickly down the chord of the wing. By $\alpha = 15$, the stall angle, this separated flow extends along a significant portion of the chord of the wing.

This data confirms that flow separation begins at the leading edge of the wing. Thus, it is possible that the onset of stall could be delayed through the

application of passive flow disruption at the leading edge. This could increase the range of angles of attack at which the GLUAS can operate, and remain effective.

3.4.2 Rigid vs. Semi-flexible Wing

Force measurements were collected for two wings with a sweep of 45 degrees, one plastic and one metal. Comparing the lift curves for these wings, shown in Figure 3.19, reveals that the plastic wing appears to have a slightly higher coefficient of lift than the metal one, although both stall at the same angle of attack. Of particular note is the higher coefficient of lift possessed by the plastic wing at $\alpha = 0$. This would seem to indicate that the plastic wing deforms in such a way so as to increase its angle of attack.

Interestingly, this deformation does not appear to negatively affect the efficiency of the wing. Figure 3.21 is a plot of the power efficiency vs. α and Figure 3.20 is the same for lift-to-drag ratio. Both metrics are noticeably higher for the plastic wing than for the metal one, especially near their peak values. As the efficiency drops at higher angles of attack, however, the results from the two wings converge to about the same value, especially for the lift-to-drag ratio.

These results contradict those of Zuo and Wang, which indicate a slight reduction in $C_{L,max}$ for flexible wings compared to rigid ones. Their findings for $\Lambda = 40$ show a 9% reduction in $C_{L,max}$ from the rigid wing to flexible, whereas these findings for $\Lambda = 45$ show a 3% increase[3]. Unfortunately, Zuo

[3]It should be noted that, though the $C_{L,max}$ difference between rigid and flexible is not

and Wang did not report any drag or efficiency results, and so these cannot be compared. (Zuo & Wang, 2010)

It is possible that the apparent contradiction in results can be ascribed to methodological differences, or the design of the wings themselves. Zuo and Wang use a different planform shape than was used in this study, and they varied flexibility by changing the wing thickness, rather than the material (both of their wings were aluminum). In addition, their flexible wings had squared leading edges, and their rigid had beveled, a design difference that may have contributed to their results as a confounding variable. (Zuo & Wang, 2010)

The results of that paper notwithstanding, this study provides some evidence that a flexible wing may both result in a slightly higher $C_{L,max}$ and in better efficiency than a rigid wing, which bodes well for the current GLUAS design, which makes use of plastic wing segments of similar thickness to those used in this study.

3.4.3 Membrane Wing Model

In addition to flexible plastic wings, a flexible membrane wing design was tested as well. When compared to the rigid wing models, the $C_{L,max}$ itself is slightly higher, being 9% higher than the $\Lambda = 5$ wing (10 standard deviations) and 8% (7.5 standard deviations) higher than $\Lambda = 25$ wing. Additionally, the

very large (3% or about half a standard deviation), there is a larger difference between the C_L values at lower angles of attack. For example, C_L at $\alpha = 17$ is 10% (30 standard deviations) larger for the flexible wing. Zuo and Wang provide limited data in their paper on the lift curves themselves for the $\Lambda = 40$ wings, and so these values cannot be compared. (Zuo & Wang, 2010)

wing has similar stall characteristics to the $\Lambda = 25$ wing, and reaches $C_{L,max}$ at 18 degrees.

During testing, the wing experienced large amounts of flutter, particularly at $\alpha = 3$, where the entire model and mounting assembly vibrated loudly. This behavior was only experienced at this specific angle of attack, and after pitching up slightly the noise subsided. Interestingly, the standard deviation in lift and drag measurements at this angle are not substantially higher than the surrounding angles of attack, and are significantly lower than the standard deviations at high angles of attack.

The drag curve for the membrane wing is shown in Figure 3.23. The drag appears to grow quadratically, and in fact a second-order polynomial fits the data with a coefficient of determination of 0.99. This is in contrast to the rigid wings which have a far more linear relation between coefficient of drag, and angle of attack. In addition, the standard deviation of the drag measurements increases substantially as the angle of attack is increased, and the curves for the efficiency metrics are much less smooth than the other tested wings.

The membrane wing shows a much higher theoretical range and endurance than any other wing tested. When compared to the next best wing, the $\Lambda = 25$ case, the membrane wing shows an 84% increase in theoretical range, and a 200% increase in theoretical endurance. In addition to these increases, the angle of attack for peak power efficiency is identical to that for peak range– $\alpha = 9$. These are the largest improvements in any metric revealed during this testing. The membrane wing also shows a significant improvement in the coefficient of lift at $\alpha = 0$ when compared to the rigid metal wings, probably

due to the deformation of the membrane resulting in camber.

3.4.4 Theoretical Model

As a basis for comparison for the experimental results, it is useful to establish a theoretical model. For this experiment, it was decided to use the Kuchemann modification of lifting line theory to describe the lift slope of the wing in terms of its sweep angle and aspect ratio. According to Kuchemann, the lift slope is given by[4],

$$a = \frac{a_0 \cos\Lambda}{\sqrt{1 + \left(\frac{a_0 \cos\Lambda}{\pi \mathrm{AR}}\right)^2} + \frac{a_0 \cos\Lambda}{\pi \mathrm{AR}}} \tag{3.10}$$

Applying this model, using the formulae for the various wing parameters given in Section 3.2.1 allows the predicted lift slope for every sweep angle to be calculated using this model. Figure 3.30 shows this plot, with the actual measured lift slopes plotted against the predicted curve[5]. This plot shows that, especially for small sweep angles, there is particularly good agreement between the theoretical predictions and the actually measured values, and that for larger sweeps the model appears to under-predict the slope of the lift curve.

Figures 3.32 and 3.33 show plots of the relative and absolute differences between the measured lift and predicted lift for various angles of attack. The

[4]For this model, the value of a_0 is taken to be $a_0 = 2\pi$. Also, note that the lift slope here is the slope of the lift curve when α is given in radians, not in degrees as is the case in the plots in this document.

[5]These models are only considered effective for small angles of attack, and thus the measured lift slope is plotted for $\alpha \in [1, 5]$ only.

Figure 3.30: Predicted Lift Slope vs. Sweep Angle (.2m root chord)

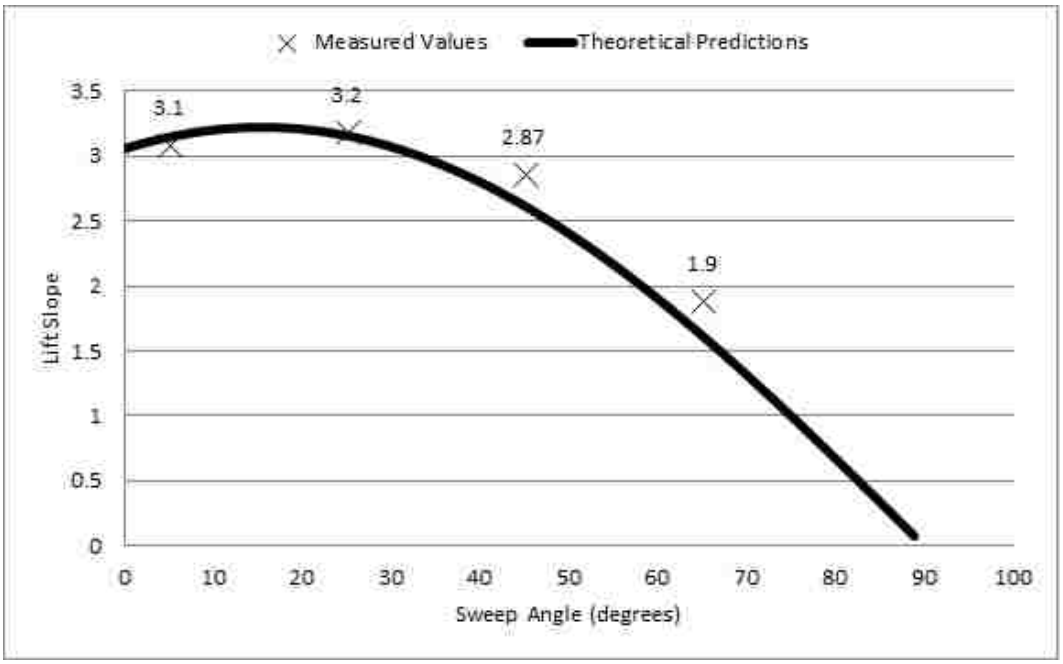

formulae for calculating these errors are,

$$\text{Absolute Error} = C_{L,predicted} - C_{L,measured} \tag{3.11}$$

$$\text{Relative Error} = \frac{C_{L,predicted} - C_{L,measured}}{C_{L,measured}} \tag{3.12}$$

with the decision to normalize the Relative Error by the measured coefficient of lift being made to avoid a singularity at $\alpha = 0$, due to the fact that lifting line theory would predicted $C_L(\alpha = 0) = 0$.

Note that, excluding $\alpha = 0$, where the relative error is quite large due to a predicted value of $C_L = 0$, for small values of α the relative error stays largely within $\pm 20\%$. The relative error appears to be relatively flat, especially on the range $\alpha \in [3, 6]$, which would appear to indicate that this model can be used

to generate an ordinal ranking of the lift slopes of the various wings, even if the specific predicted values are not completely accurate.

Figure 3.31: Kuchemann Parameters vs. Sweep Angle (.2m root chord)

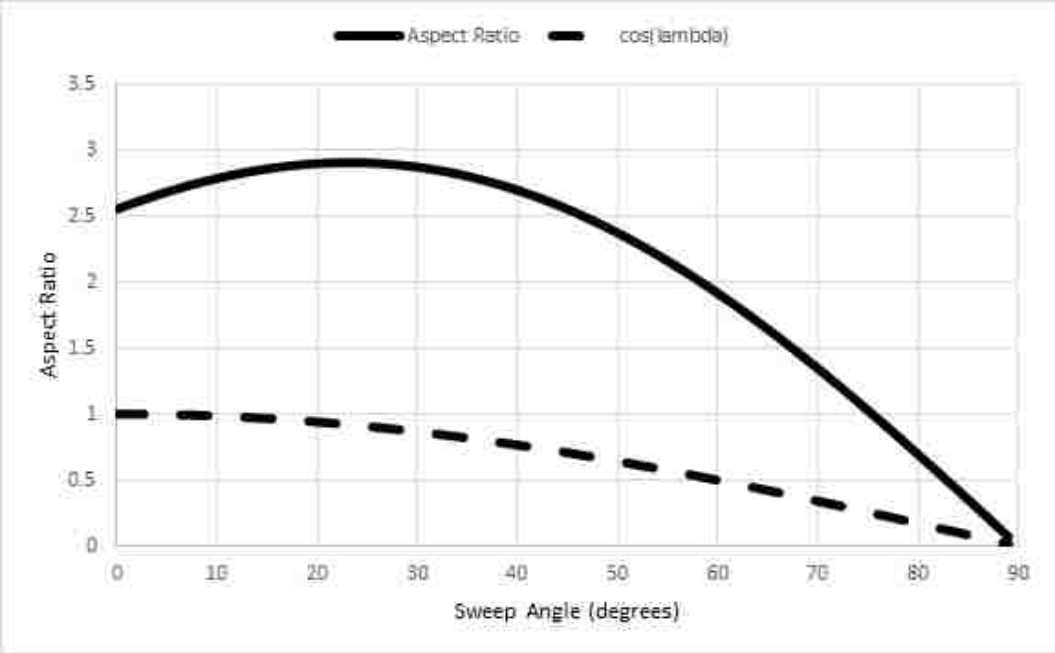

There appears to be a peak in the lift slope at $\Lambda = 15$ for this wing geometry. This peak appears to be due to the interplay between the $\cos\Lambda$ term, and the aspect ratio of the wing. The values of each of these terms are given in Figure 3.31.

Figure 3.32: Relative Difference from Theory vs. Angle of Attack for Each Sweep Angle

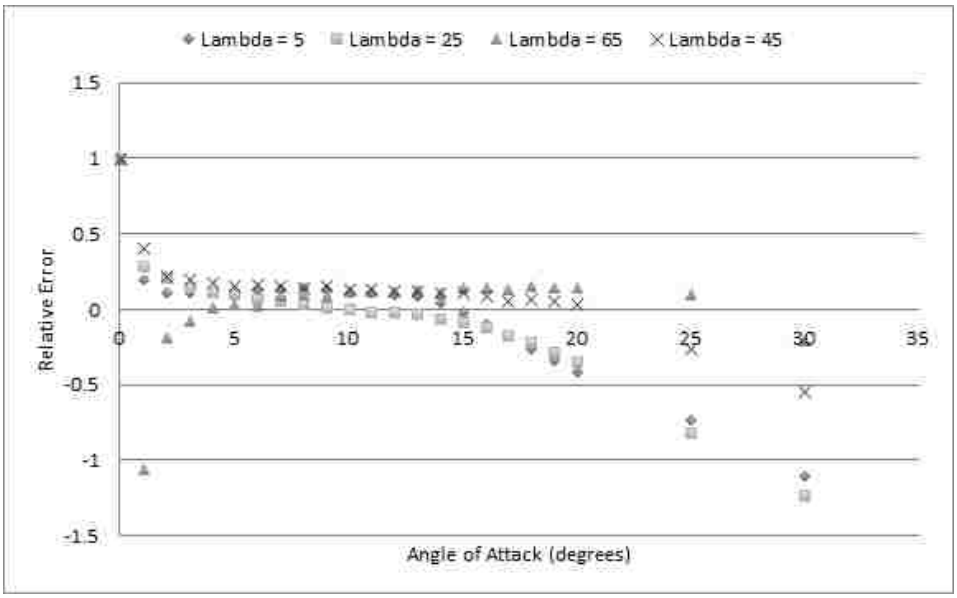

Figure 3.33: Absolute Difference from Theory vs. Angle of Attack for Each Sweep Angle

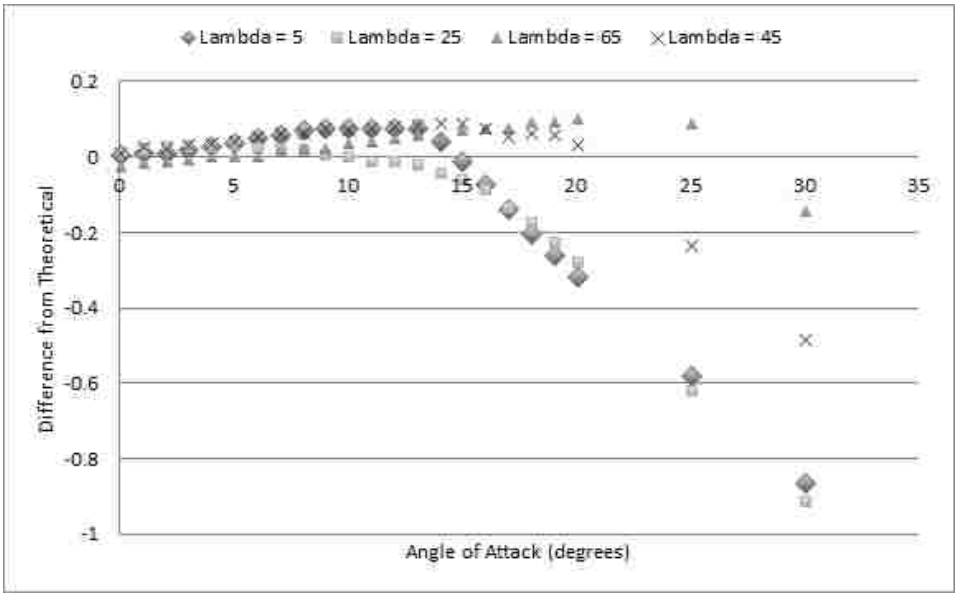

Chapter 4

Performance

4.1 Flight Testing

4.1.1 Introduction

As part of the characterization and design process for the GLUAS, it is self-evident that practical, real world testing of the design in question is necessary. This testing took the form of a large number of flight tests of the various design iterations of the the model, starting with the Model 4 GLUAS, and moving into the Model 5, along with the many design modifications that have been effected on it.

4.1.2 Model 4

Flight testing began in October, 2016. The initial flight test served to duplicate results obtained already for the Model 4 GLUAS. The projectile was

flown to altitude by a carrier aircraft, and released. It was successfully glided to the ground, and managed to cover an unexpectedly large (though not properly measured) distance. During this flight, the left elevon was torn free from the projectile, and thus the flight path was sporadic–though the projectile remained controllable. This gliding test was flown with the assistance of a first-person video stream from the front camera of the projectile, and was completely unpowered. The projectile landed and was recovered without incident, and was in perfect working order.

Further testing was performed upon the same model in order to assess its powered-flight capabilities. Initial powered tests showed that the Model 4 GLUAS suffered from a severe yaw instability during powered flight, and that the action of the propeller would cause the model to violently spin in a circle. The suspected reasons for this, and the design changes to resolve it, are detailed in Section 2.2.1.

During this flight, no yaw instability was observed. However, a large pitch instability was discovered–the Model 4 GLUAS was prone to suddenly and unexpectedly pitching up to an extreme angle, resulting in loss of control. The reasons and resolution to this instability are discussed in Section 2.2.2. The projectile was recovered in working condition.

In order to verify that the suspicions regarding the cause of the pitch instability were correct, an additional flight test was performed with a Model 4 GLUAS which had been modified via nuts, bolts, and fishing weights, to move the center of gravity forward. This flight was successful in showing that the projectile was pitch stable, however sustained flight was not obtained due

to trim problems. The projectile was recovered in working condition, however electrical problems due to overheating prevented further flight tests. This was the final test flight of the 2016 flying season.

4.1.3 Model 5

Further flight testing resumed in March, 2017, and the Model 5 GLUAS was tested for the first time. Unfortunately, adverse weather conditions resulted in loss of stability, and the subsequent uncontrolled descent and landing rendered the projectile inoperable and unable to be tested further. The test did confirm that the Model 5 redesign resolved the electrical issues which had rendered the Model 4 inoperable during the previous flight test, however because the exact cause of the loss of stability could not be identified, the results did not sufficiently demonstrate that the redesign had resolved the pitch instability experience by the Model 4. It was thought that the loss of control was due to the wind, which was blowing at 9-10 knots.

Following this test, access to a flight testing area was lost, and a new flight test field would not be made available until July, 2017.

The next flight test occurred at the author's home during June, 2017. This flight test was unsuccessful, with the Model 5 GLUAS immediately nose-diving after an attempted hand launch. It is thought that this was due to the fact that the projectile's wing segments[1] had been badly warped by heat.

Many flight tests were attempted during the months of July - October,

[1]These wing segments had been printed on a Statasys Objet, using Veropurewhite (RGD837), a material which proved insufficient for the structural needs of the GLUAS in several ways, detailed in Section A.2.

2017, once Lehigh University's drone field became available. Through these tests, sustained flight was not attained, however a very wide array of design improvements were identified. During these tests, the projectile did not appear to suffer from pitch instability that plagued the Model 5 design.

The primary causes of the crashes during this series of flight testing were the loss of propeller (see Section 2.2.4), loss of thrust due to friction (see Section 2.2.3), and stall due to pilot error and insufficient control authority.

After further iteration, many of these initial issues were resolved. A new propeller mount was devised to prevent loss of propeller during flight. The motor mount was adjusted, and the connection of the two fuselage components was strengthened. These changes were sufficient to resolve the main issues that plagued flight tests up to this point.

Following these adjustments, more flights were attempted. During several of these flights, the GLUAS banked left heavily, even when the controls were set as far as they would go to counteract this. This was the result of an apparent trim problem, and so steps were made to resolve this. The autopilot code was modified slightly in an effort to provide more control authority, but this was insufficient.

Counteracting banks like this during takeoff is traditionally the task of the rudder, but the GLUAS does not have a control surface there. So, instead, it was decided to put a fixed angular offset on the tail, to counteract this left roll and yaw tendency. One more flight was attempted with this fixed offset in place, and the GLUAS crashed after banking to the right. So it appears that the idea was sound, but that the 10 degree offset used was too great.

Table 4.1: Physical Characteristics of the Model 5 GLUAS

Model	Planform Area	Total Weight	Weight / Planform Area
Model 5	$0.097\,\mathrm{m}^2$	$3.80\,\mathrm{N}$	$39\,\mathrm{N\,m^{-2}}$
Model 5m	$0.10\,\mathrm{m}^2$	$2.89\,\mathrm{N}$	$29\,\mathrm{N\,m^{-2}}$

Table 4.2: Input parameters for Range and Endurance calculations. Values marked with an * are taken from Schutter's thesis (Schutter, 2016).

Parameter Name	Parameter Symbol	Value
Energy Density (*)	E^*	$539\,\mathrm{kJ\,kg^{-1}}$
Efficiency (*)	η	0.40
Air Density (*)	ρ	$1.225\,\mathrm{kg\,m^{-1}}$
Battery Mass	m_{batt}	$0.04\,\mathrm{kg}$

4.2 Theoretical Range and Endurance

Based on the experimental data from the test models, we can extrapolate the theoretical range and endurance of the Model 5 GLUAS, based on the range/power efficiency from the data, the weight of the test models, and surface areas of the test models. These values are listed in Table 4.1.

For this analysis, the most representative wind tunnel cases are used. Thus, the $\Lambda = 5$ case is used to provide the data for the standard Model 5, and the membrane wing case is used to provide the data for the Model 5m, with the membrane wing. The other pre-specified values used for the analysis are shown in Table 4.2.

Using these values, along with the wind tunnel measurements for peak lift to drag ratio and endurance, the theoretical peak range and endurance of the two versions of the Model 5 can be calculated. These values have been non-dimensionalized by dividing by the upper-end of the design targets given

Figure 4.1: Non-dimensional Range vs. GLUAS Model

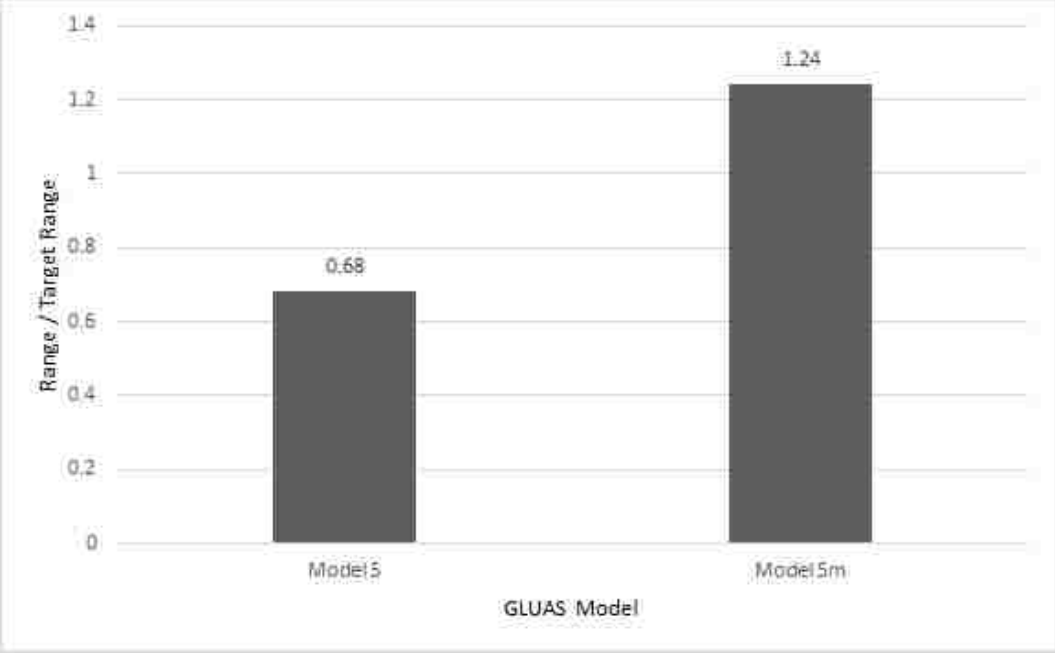

in Table 1.1, namely by 15 minutes for Endurance and 16.1 km for range. Figure 4.1 shows the calculated theoretical non-dimensional ranges for the two models, and Figure 4.2 shows the calculated non-dimensional endurance values. A value of 1.0 is indicative of meeting the upper-end requirement exactly, larger values exceed the requirement, and smaller ones do not meet it.

Comparing these calculated numbers to the requirements in Table 1.1 shows that both models fall within the targets for both range and endurance for all three design phases. However, the Model 5 does not meet the upper limit target for range.

These numbers could easily be increased further by expanding the available battery mass. At the moment, the batteries used for the Model 5 GLUAS are 450mAh LIPO batteries with a mass of 0.04 kg. If we assume constant en-

Figure 4.2: Non-dimensional Endurance vs. GLUAS Model

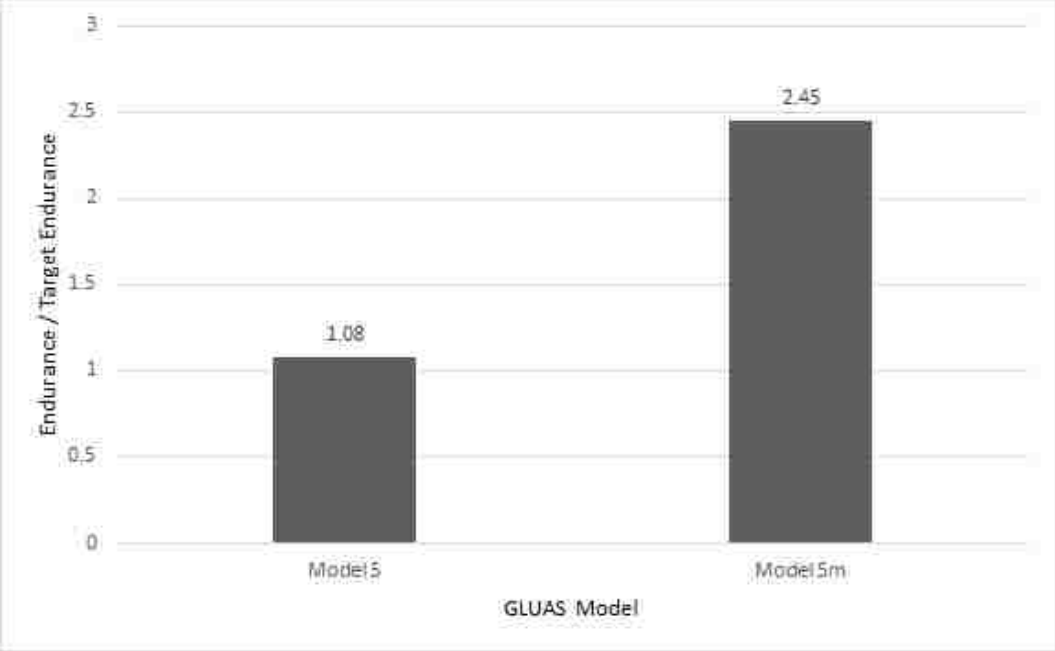

ergy density as mass increases, we can use the range and endurance equations to attempt to find an optimal battery mass. As battery mass increases, the amount of energy carried in the projectile, and thus its range and endurance, are increased. However, heavier batteries also increase the mass of the projectile, and so it might be expected that there is a point of diminishing return to carrying additional battery mass.

Figures 4.3 and 4.4 show how the range and endurance of the GLUAS changes as the battery mass is increased. Here, the battery mass has been non-dimensionalized using the total mass of the projectile,

$$m^+ = \frac{m_{battery}}{m_{battery} + m_{structural}} \tag{4.1}$$

The plots reveal that the range increases in a roughly linear fashion as

Figure 4.3: Model 5 Endurance vs. Battery Mass

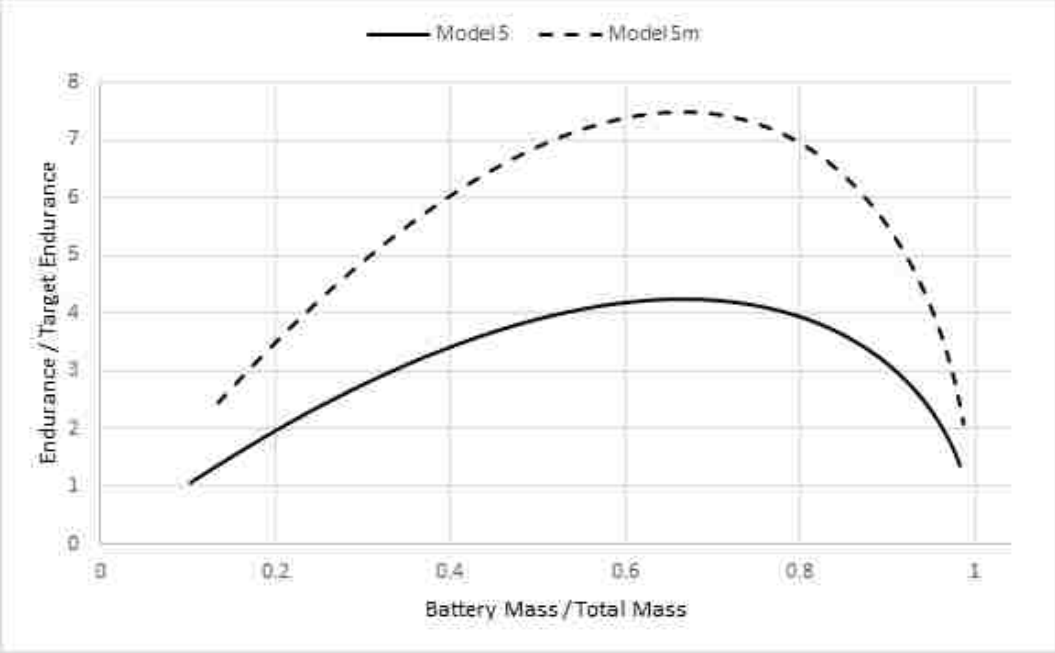

Figure 4.4: Model 5 Range vs. Battery Mass

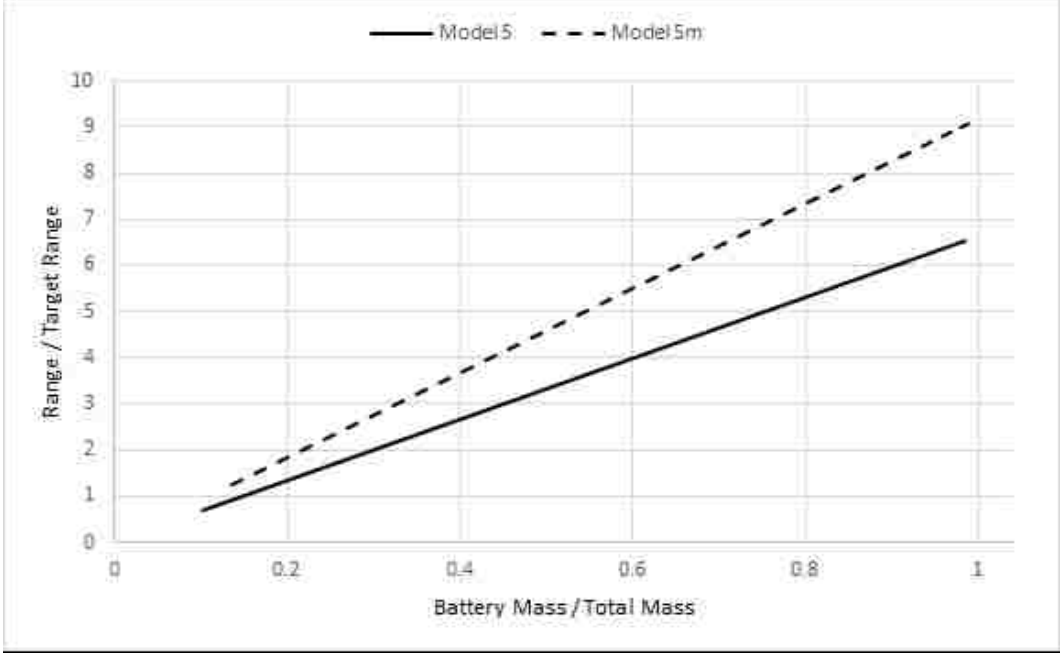

the battery constitutes more and more of the overall mass of the projectile. However, the endurance reaches a maximum, and begins to decline sharply passed that point. The peak endurance values occur at roughly $m^+ = 0.7$ for both the Model 5 and the Model 5m. Naturally, this m^+ value would not be easily obtained, however this result does reveal that increasing the battery mass will directly increase the range and endurance of the projectile for any reasonable amount of increase. Also, in the immediate vicinity of the current m^+ value, this increase in endurance will be roughly linear with the increase in m^+.

Currently, the GLUAS as designed, in both models, exceeds the target mass by a large margin. This is because the target mass provided is for a 40 mm variant, not the 60 mm variant actually being examined here. The Model 5 has a mass of 0.388 kg and the Model 5m of 0.295 kg, compared to the design target of 0.180 kg. This does seem to indicate that reaching these targets for the 40mm projectile will be quite difficult, as even the small 0.04 kg battery currently in use is too large to fit into that form factor.

Chapter 5

Conclusion

In this document, the design of a gun launched unmanned aerial system designed to fit inside of a 60mm mortar shell has been presented, alongside theoretical and experimental data both describing the design, and suggesting improvements to future designs.

Two possible models have been presented, one using a segmented plastic wing, and the other a flexible membrane wing. While the prototype membrane wing model remains untested, experimental data and theoretical calculations suggest that this model will perform better than the segmented wing model in terms of range and endurance, which are the major targets for optimization within the requirements.

Experimental data and theoretical calculations indicate that both designs should meet the targeted range and endurance requirements for the project. Unfortunately, obtaining successful flight tests of the GLUAS has proven difficult. The segmented wing model's control surfaces only constitute 10% of the

planform area, and the model is small enough to be subjected to significant propeller effects, resulting in control and stability issues during powered flight that have yet to be fully resolved.

5.1 Next Steps

5.1.1 GLUAS Design

Moving forward from this point, there are a number of possible directions that this project could take. First and foremost, the top priority is demonstrating stable flight using the existing Model 5, if possible. This has proven difficult due to trim problems, and a lack of control. As such, it seems advisable to return to the previous deployment technique of mounting the GLUAS on the underside of a large carrier aircraft, flying it to altitude, and releasing it. This allows the GLUAS to be deployed at a much higher flight speed than a simple hand launch, as well as allowing more time to attempt to gain control of the GLUAS before it hits the ground. The GLUAS itself is rather small, and potentially hard to see from the ground in flight, but the video system can be used to provide a first-person view of the projectile in flight, which can be used to control it.

Once stability has been demonstrated, further design iterations can be tested. Based on the results of this study, it appears that a membrane wing might be a good direction to take the design. The use of a membrane makes the overall projectile much lighter (The Model 5m is about 0.9 Newtons lighter than the Model 5), increase endurance and range, and also make assembly,

wing folding, and wing deployment much easier. However, the Model 5m's current method of control is a stopgap, meant for a quick proof of concept using the current Model 5. The use of a membrane allows for much more sophisticated control schemes. Two potential directions would be the use of servos to rotate each wing independently to control its angle of attack, or the use of small actuators mounted on battons to warp the shape of the wing.

In either case, the GLUAS must ultimately move away from mechanical actuators, as these devices cannot stand up to the forces of deployment out of a mortar. Piezoelectric actuators are solid-state, and should be able to survive these forces, however they require very high voltage to operate, and have limited actuation ranges.

5.1.2 Wind Tunnel Testing

Further wind tunnel testing should focus on examining the effects of propeller wash on the flow characteristics around the wing. As a micro-aerial vehicle, the propeller effects affect a significant portion of the overall planform area of the GLUAS, and thus a full understanding of the aerodynamics of the GLUAS must take this into account.

Thus, a similar experimental setup to the one used by Schutter must be devised with appropriate scaling for the propeller and electric motor (Schutter, 2016). Unfortunately, this is going to require using a much smaller wing than the half-model design can accommodate.

In addition to examining the propeller effects, further examination of membrane wings can be performed. At present, only a single design has been tested.

No consideration has been given to the thickness of the membrane, the means of attaching the membrane to the spars, the layout of spars and battons, the pre-tension on the membrane, or the effect that warping the membrane for control purposes would have. This topic could potentially provide a rich line of inquiry. Further examination of the membrane wing using PIV could also yield interesting results, perhaps helping to explain the increase of variance in the drag measurement with angle of attack.

Appendix A

3D Printing

A.1 Printer Maintenance

A.1.1 Nozzle Cleaning

Because the TAZ relies on making electrical connections through the nozzle in order to level the bed, it is very important that the nozzle remain clean. In between prints, the nozzle should be warmed up to extrusion temperature, and the exterior brushed vigorously using a nylon brush. **Do not use a metal brush, or any solvent, while the printer is turned on.** Because of the electronics in the nozzle, this could cause a short and permanently break the auto-leveling feature of the extruder. Should this happen, the entire extruder will need to be replaced.

Short of general cleaning, every so often the nozzle should be removed from the extruder and thoroughly cleaned. The removal process is discussed in Section A.1.5. Soak the nozzle in a solvent that will remove whatever

plastic has been being used (isopropyl alcohol for PLA/PVA, acetone for ABS, Limonene for HIPS). A metal brush can be used when the nozzle is removed.

A.1.2 Filament Changing

When changing filament, be sure to take the opportunity to purge the inside of the nozzle using cleaning filament. Bring the hot-end to the print temperature of the plastic last printed, and manually force cleaning filament through the nozzle until it runs clear. Then, remove the cleaning filament, bring the extruder up to the temperature of the new filament to be used, and manually force this filament through until the last of the cleaning filament has been purged.

A.1.3 Print Bed Cleaning

At least weekly, the print bed should be cleaned using a brush and solvent. Use the appropriate solvent for the materials being printed, and brush gently with a nylon brush. Don't use too much force, or the PEI coating on the bed could be damaged. Cleaning the print bed can help reduce platform adhesion problems.

A.1.4 Nozzle Cleaning Pad

As part of the printing process, the TAZ automatically runs the nozzle across a cleaning pad. However, if this pad becomes too dirty, this process can actually become counter-productive and transfer plastic onto the nozzle. Periodically,

this pad should be replaced. This can easily be done by removing the two screws holding the plastic piece around the pad in place. The cleaning pads themselves are two sided, so either flip it over or replace it, and reattach the holder to the printer.

A.1.5 Nozzle Removal

Occasionally, either for cleaning or for changing out the nozzle, the nozzle will need to be removed from the extruder. This process will require an 18mm wrench, a 7mm wrench, a 2.5mm hex key, and a 2mm hex key.

First, unplug and remove the extruder from the 3D printer. In order to properly access the nozzle, the layer cooling fans will need to be removed. This can be done by first removing the fans using the 2.5mm key. Once the fans are removed, a set of 2 screws holding the fan outlets onto the extruder will be revealed. Remove these with the 2mm key.

With these parts out of the way, use the 18mm wrench to hold the hot end firmly in place, and remove the nozzle using the 7mm wrench. This will require some force. If the hot end twists during this process, be sure to return it to its original position.

When ready to replace the nozzle, tighten it into the hole using the 7mm wrench–again holding the hot end in place. Strictly speaking, the nozzle should be tightened to exactly 30 inch-pounds of torque. With the hex nozzle that comes with the printer, this torque is more important as if it is over or under-torqued the nozzle could fracture. However, with E3D nozzles, this is less of a concern.

Once the nozzle is back and sufficiently secured, replace the fans and their outlets. Then reattach the extruder to the printer and plug it in.

A.1.6 Changing Extruder

The TAZ-6 has support for a variety of extruders. At this time, the lab has two–a single extruder and a dual-extruder. The printer should have all the hardware (second cable, filament spool, etc.) for the dual extruder already attached. Simply turn off the printer, remove the current extruder and attach/plug in the new one.

Once this is done, it is critically important to flash the appropriate firmware to the TAZ using Cura, otherwise the printer could break when it is given a print order. This can be done by turning on the printer, connecting Cura, and flashing the new firmware. To do this, select the *Machine Settings* option under the *Machine* dropdown menu in Cura, and then press the *Change Tool Head* button and follow the onscreen instructions.

Once this is done, you will need to update the extruder steps calibration on the printer itself. The appropriate value for this field is written on the back of the extruder. Enter this number by clicking once with the scroll wheel on the printer, then selecting *Configuration*, then *Advanced Settings*. Scroll to the very bottom of the list of settings until the field *ESteps/mm* is highlighted. Select this, and enter the number. For the single extruder there will only be one of these fields, for the dual there will be two. If you do not see the correct number of fields, it means that the firmware has not been properly flashed, so repeat that step and then try again.

In the case of the dual extruder, further calibration will be required to determine the offset between the two nozzles. The calibration steps are part of the OHAI for the TAZ 6 duel extruder, which are found here: `https://ohai.lulzbot.com/project/TAZ-6-dual-extruder-v2-tool-head-installation/accessories/`.

A.2 Material Considerations

A.2.1 PLA (Polylactic Acid)

PLA is a commonly used filament, and constitutes the majority of the filament currently in the lab. It is a good, general purpose thermoplastic that is easy to work with. It should be printed at a temperature between 190 °C and 220 °C and the print bed should be heated to 60 °C.

PLA is a fairly brittle material with little flexibility. It doesn't have as good of impact resistance as ABS, and it has a low melting point. It will become plastic and deform, for example, if left in a hot car. In addition, PLA will slowly dissolve in water and so is unsuitable for use in objects that need to be submerged for any length of time.

With that said, PLA is very well behaved as a printing material, and is a good default plastic to use for printing parts.

A.2.2 PVA (Polyvinyl Alcohol)

PVA is a flexible plastic that is readily dissolved in water. It makes for an excellent support material when printed using a dual-extruder with PLA, as it has very similar printing properties, and can be dissolved away post print. PVA should be printed at a temperature of around 190 °C and at a bed temperature of 60 °C.

Note that PVA has significant platform adhesion problems. It should be printed on a bed that has been coated with a PVA glue stick. As this coating makes it very difficult to remove PLA components, it is usually best to print the part on a PVA raft, so that no PLA is in contact with the coated print bed.

PVA is very sensitive to moisture, and will readily absorb it from the air. When it does, steam will be released from the nozzle while printing, and the PVA will be brittle. To avoid this, also store PVA in an airtight container with a desiccant. If PVA does absorb a lot of water, it can be dehydrated in a warm oven.

A.2.3 ABS (Acrylonitrile Butadiene Styrene)

ABS is a very durable plastic that can be used for parts that are expected to undergo a lot of stress. It has more flexibility than PLA, and much better temperature resistance.

ABS should be printed at 230 °C to 240 °C on a print bed heated to 100 °C. This material is not as well behaved as PLA, and tends to have platform

adhesion problems. In addition, it shrinks as it cools, and if it is cooled too quickly, it will warp. As a result, when printing in ABS it is important to turn off the layer cooling fan on the printer, and keep the printer away from open windows or air outlets.

In order to ensure that an ABS part adheres well to the bed, the bed should be coated with "ABS juice", a solution of ABS plastic dissolved in acetone.

Some shrinkage is unavoidable. For example, a part with screw holes that works just fine in PLA will have the holes be in slightly different places with ABS. Occasionally, this shrinkage is enough to cause tolerance problems, so it may be necessary to very slightly oversize a part when printing with ABS.

The fact that ABS dissolves readily in acetone means that the complex parts can be printed to pieces, and then acetone can be used to solvent-weld them together. Acetone can also be used to smooth the surface of a part.

A.2.4 PETG Carbon Fiber (Polyethylene Teraphthalate - Glycol)

PETG itself is a plastic that is well behaved, and fairly strong. This filament consists of PETG mixed with strands of carbon fiber. It should be printed at temperatures around 240 °C with a bed temperature of 60 °C.

Because of the carbon fiber reinforcements, this filament is highly abrasive and will wear out a brass nozzle very quickly. Only print using this filament with a reinforced steel nozzle.

A.2.5 HIPS (High Impact Polystyrene)

HIPS is a material with similar printing temperatures to ABS, however it is readily soluble in Limonene. This makes it an ideal support material for ABS, as well as being able to be used on its own to create parts. HIPS should be printed at a temperature of 225 °C with a bed temperature of 100 °C.

A.2.6 Vero Filament

The Vero filaments are used by the Stratasys Objet printer located in Wilbur. These materials result in a very smooth and nice looking part, however they are very fragile and very temperature sensitive. Parts made using this material are unsuitable for non-aesthetic roles.

The material cracks very easily. Unsupported structures (such as wings) made from this material will droop, and will not return easily to their original shape. In addition, this drooping is exacerbated by high temperatures.

A.3 Troubleshooting

A.3.1 Autoleveling Fails

The auto-leveling procedure that the printer executes just prior to performing a print is critical to ensuring that the print will come out evenly. However, this process is very sensitive to the cleanliness of the nozzle.

There are four conductive pads on the corners of the print bed. The print head will sequentially touch these pads, creating an electrical connection, to

detect their height, and with this information will calculate the plain of the bed. This will allow the printer to correct for the bed not being perfectly level.

However, this process will fail if an electrical connection cannot be made. The printer will try to level the bed three times. If at any point it fails to make a connection, it will rewipe the print head on the cleaning pad and restart the process. In order to move to the next corner, the printer will touch each pad twice–once quickly and once slowly.

If, after three attempts, the bed leveling is not completed, then the print job will be canceled and the printer will beep.

Should this occur, it is likely due to an accumulation of plastic residue on the nozzle itself. Clean the nozzle, and attempt the print again. If this still does not work, it is possible that a short has developed in the print head. This will result in the print head needing to be replaced.

A.3.2 Uneven Extrusion

Occasionally, the 3D printer will not evenly extrude filament, resulting in skipped layers in the part. Should this occur, ensure that you are printing at the appropriate temperature for the filament in question–too low or two high can be both result in clogging and flow issues. In addition, the nozzle can be seasoned in order to help the filament flow more evenly and prevent sticking. To do this, bring the hot-end up to temperature, and manually feed filament through that has been coated with olive oil. This step appears to be especially important with MatterHacker's Pro Series PLA filament, which seems fairly sticky.

In addition to these, uneven heating of the nozzle can result in this problem as well. This is especially evident when using a hardened steel nozzle, for printing an abrasive filament like Carbon Fiber or Nylon.

A.3.3 Printer Connection Failure in Cura

If a connection to the printer from the Cura software cannot be established, it may be due to another Cura session being open on the host computer. In order to reset the serial connection and allow a new session, unplug the USB cable from the back of the printer, and then plug it back in. This should allow a new connection to be established. Note that simply power-cycling the printer will not accomplish this–the USB cable must be removed.

A.3.4 Insufficient Platform Adhesion

One of the more common causes of print failure that's been observed thus far as been a failure of the part to adhere to the platform. This is especially true of small parts with little contact with the print bed.

In general, printing on a brim can help to rectify this problem. However it isn't a guaranteed fix. Should a brim on its own not work, then the print bed can be coated in order to assist with adhesion. If the part being printed is PVA or PLA, coat the region of the bed that is bring printed on with PVA glue stick, and if the part is ABS, warm up the bed and coat it with a mixture of acetone and ABS.

Be careful, as these coatings can make part removal very difficult. Especially PVA glue stick combined with PLA. If this combination is used, and the

part cannot be removed from the bed, pour isopropyl alcohol around the part and allow it to sit for a few moments, then try again to pry the part off. Be very careful, as the part will likely separate from the bed violently, and will present a splash hazard. Wear eye protection.

If an ABS part cannot be removed from the bed, then do the same thing only with acetone. Make sure to cool the bed so that the acetone doesn't immediately evaporate.

Note that the TAZ 6 print bed is coated with PEI for improved adhesion, and so Klapton tape is redundant. When printing PLA, adhesion will rarely be a problem. However, it will be important to use the appropriate coating for PVA and ABS, as these have a much harder time adhering to the bed.

A.4 General Comments

This section contains a number of general comments that don't fit well anywhere else regarding the use of the 3D printer.

- Before printing, ensure that there is sufficient filament left on the spool, and that the filament isn't tangled. A print can be paused at any time, and the filament replaced, however if the printer is allowed to run for more than a few moments without filament, there is no way to rewind it, and the print will need to be restarted.

- Watch the print start, to ensure that filament is extruded properly. At the very start, the printer will extrude a line of filament. Occasionally, this test extrusion can get dragged onto the part and cause a print failure,

so it pays to watch the first few moments of the print to manually remove it.

Appendix B

Data Analysis

Coding/Algorithms

B.1 Data Rotation

The following algorithm was used for data rotation, to ensure that all measurements are reported relative to the wind tunnel test section, and not the test model itself. For simplicity, only the forces in x and y were considered–thus only a square rotation matrix was needed.

First, the rotation matrix itself was defined.

```
def rotation_matrix(angle):
    sina = numpy.sin(angle)
    cosa = numpy.cos(angle)
    rotation = numpy.array([[cosa, -sina],
                            [sina,cosa]], dtype='float32')
```

```
    return rotation
```

This matrix was then applied to the force data. The original version of this code was,

```
def rotate_data_old(data, degrees):
    rotation = np.ascontiguousarray(
                    rotation_matrix(convert_radians(degrees)))
    transformed = np.ascontiguousarray(numpy.empty((len(data), 2),
                                                   dtype="float32"))

    for i in range(len(data)):
        transformed[i] = rotation @ data[i]
    return transformed
```

However, a parallel version of this algorithm based on CUDA was later implemented for processing large amounts of data,

```
@cuda.jit()
def rotation_kernel(rotation_matrix, data_array, output_array):
  i = cuda.grid(1)

  if i >= len(data_array):
      return

  output_array[i,0] = (rotation_matrix[0,0] * data_array[i,0])
                    + (rotation_matrix[0,1] * data_array[i,1])
```

```
    output_array[i,1] = (rotation_matrix[1,0] * data_array[i,0])
                      + (rotation_matrix[1,1] * data_array[i,1])



def rotate_data(data, degrees):
    rotation = rotation_matrix(convert_radians(degrees))
    N = len(data)
    transformed = numpy.empty((N, 2), dtype='float32')

    threadsperblock = 32
    blockspergrid = (N + (threadsperblock -1)) // threadsperblock

    rotation_kernel[blockspergrid,threadsperblock](np.ascontiguousarray(
                                                       rotation),
                                                   np.ascontiguousarray(
                                                       data),
                                                   np.ascontiguousarray(
                                                       transformed))

    return transformed
```

Appendix C

Original Experimental Design

C.1 Old Experimental Design

The originally designed experimental model was based directly on a scaled down GLUAS, including segmented wings that were a slight generalization of the real thing.

Due to size constraints, it was decided to begin characterization using a geometrically scaled model of the GLUAS, which had been cut in half along the centerline of the horizontal axis.

While it was desirable to collect data for the full model directly, the scaling factor required to allow the full sized model to be used in available testing facilities presents difficulties.

It was calculated that, in order to effectively use the available facilities, the overall surface area of the wings, as projected onto the vertical axis at a given angle of attack, must be reduced to 60% of their full size, at the absolute

Figure C.1: A direct comparison among components of the 1, .75, and .5 scale models, in decreasing order of size.

minimum. Experiments have been made with fabricating models that have been geometrically scaled by factors of 0.5 (roughly reducing the overall area to 25% of full scale) and 0.75 (50% of full scale).

Although a test model at 0.5 scale would see the largest reduction in test section blockage, the fabrication of a model at this scale has presented difficulties, due to the thinness of the wings and fuselage. As a result, a 0.75 scale model has been fabricated. This model still has a blockage ratio of less than 10%. Figure C.1 shows pieces of the vehicle to demonstrate all three scales. Figure C.2 shows a comparison between the 0.75 scale model to be used for testing, and the full size model. Figure C.3 shows the fully assembled 0.75 scale half model prototype. Note that the duct tape is used as a simple elevon joint. A version second experimental set of wings was created without the

Figure C.2: A comparison between the lower fuselage of the full sized model, and the .75 scale model to be used in wind tunnel testing.

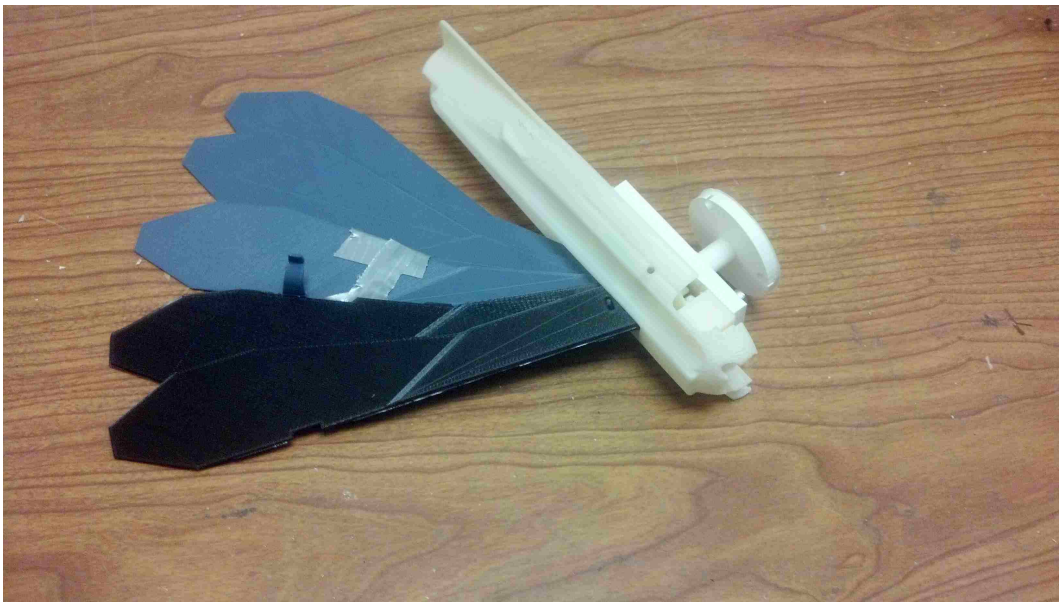

Figure C.3: The half model experimental prototype for use in wind tunnel testing.

elevon joint or control horn, for more generic tests. A diagram of these wings is given in Figure C.4.

Ultimately, this setup was dropped for the more general approach described in the rest of this document.

Figure C.4: A sketch of the simplified, segmented test wing. It is likely that this wing can be used for segmented testing under the current scheme.

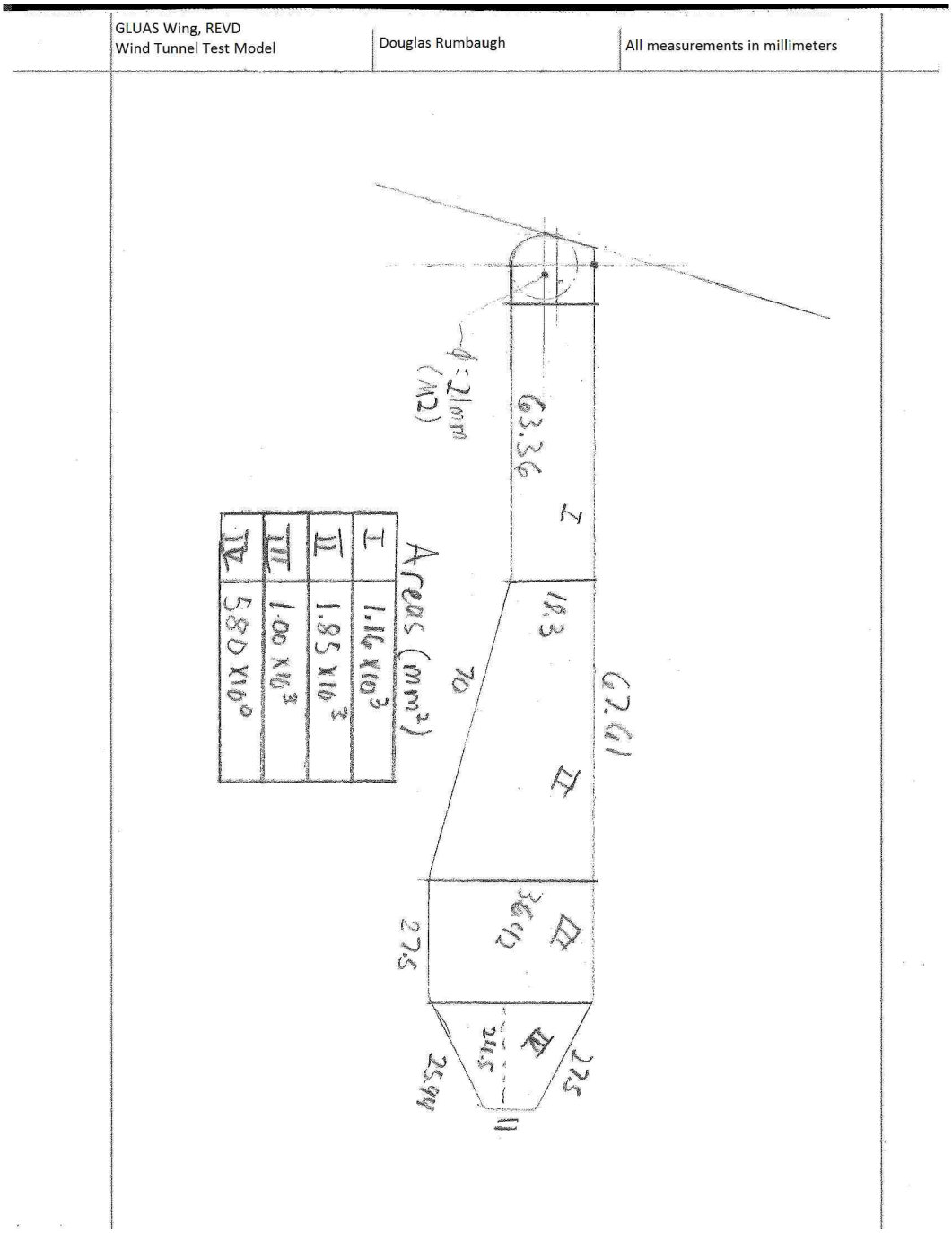

Appendix D

Autopilot Code

D.1 Lisa Code

```
<!DOCTYPE airframe SYSTEM "airframe.dtd">
<airframe name="gluas">

  <firmware name="fixedwing">
    <target name="sim"                    board="pc">
      <module name="radio_control" type="ppm"/>
    </target>

    <module name="gps" type="ublox"/>

    <target name="ap" board="lisa_s_1.0">
      <module name="radio_control" type="superbitrf_rc">
```

```
      <define name="RADIO_TRANSMITTER_ID" value="0xD47B3ECE"/>
      <define name="RADIO_TRANSMITTER_CHAN" value="0x06"/>
      <define name="RADIO_TRANSMITTER_PROTOCOL" value="0x01"/>
      <define name="USE_PERSISTENT_SETTINGS" value="TRUE"/>
      <!-- the periodic frequency is 60 by default -->
      <!-- AHRS_PROPAGATE_FREQUENCY must be < PERIODIC_FREQUENCY -->
      <configure name="AHRS_PROPAGATE_FREQUENCY"
                 value="120"/>
      <!-- 120 seems to be the max of the barometer -->
      <configure name="PERIODIC_FREQUENCY"
                 value="120"/>

      <define name="RADIO_MODE" value="RADIO_GEAR"/>
      <define name="RADIO_AUTO_MODE" value="RADIO_FLAP"/>
    </module>
  </target>

  <define name="USE_BAROMETER" value="TRUE"/>
  <module name="imu" type="lisa_s_v1.0" />
  <module name="ahrs" type="int_cmpl_quat"/>
  <configure name="USE_MAGNETOMETER" value="FALSE"/>
  <module name="telemetry"      type="superbitrf"/>
  <module name="control"/>
  <module name="navigation"/>
```

```
    <module name="ins" type="gps_passthrough"/>
  </firmware>

<!-- enable debugging -->
  <modules>
    <load name="gps_ubx_ucenter.xml">
      <define name="GPS_UBX_NAV5_DYNAMICS"
              value="NAV5_DYN_AIRBORNE_2G" />
      <define name="DEBUG_GPS_UBX_UCENTER"
              value="TRUE" />
    </load>
  </modules>

  <commands>
    <axis name="THROTTLE" failsafe_value="0"/>
    <axis name="ROLL"     failsafe_value="0"/>
    <axis name="PITCH"    failsafe_value="0"/>
  </commands>

  <servos>
    <servo name="THROTTLE"            no="0"
           min="1000" neutral="1000" max="2000"/>
    <!--no=1, SERVO 5 on board, BAT3&4-->
    <servo name="ELEVON_LEFTSIDE"   no="1"
```

```
            min="2100"  neutral="1500"  max="900"/>
    <!--no=2,SERVO 4 on board, BAT4 -->
    <servo name="ELEVON_RIGHTSIDE"  no="2"
            min="900"  neutral="1500"  max="2100"/>
  </servos>

<command_laws>
  <let var="aileron"              value="@ROLL  *  .8"/>
  <let var="elevator"             value="@PITCH * .8"/>
  <set servo="THROTTLE"           value="@THROTTLE"/>
  <set servo="ELEVON_LEFTSIDE"    value="$elevator + $aileron"/>
  <set servo="ELEVON_RIGHTSIDE"   value="$elevator - $aileron"/>
</command_laws>

<section name="BAT">
    <define name="MILLIAMP_AT_FULL_THROTTLE"  value="45500"/>
    <define name="CATASTROPHIC_BAT_LEVEL"  value="3.2"  unit="V"/>
    <define name="CRITIC_BAT_LEVEL"  value="3.5"  unit="V"/>
    <define name="LOW_BAT_LEVEL"  value="3.7"  unit="V"/>
    <define name="MAX_BAT_LEVEL"  value="4.2"  unit="V"/>

  </section>

  <rc_commands>
```

```
    <set command="THROTTLE" value="@THROTTLE"/>
    <set command="ROLL"     value="@ROLL"/>
    <set command="PITCH"    value="@PITCH"/>
  </rc_commands>

  <section name="IMU" prefix="IMU_">
    <!--board orientation-->
    <!--roll-->
    <define name="BODY_TO_IMU_PHI"   value="120." unit="deg"/>
    <!--pitch-->
    <define name="BODY_TO_IMU_THETA" value="0." unit="deg"/>
    <!--yaw-->
    <define name="BODY_TO_IMU_PSI"   value="0." unit="deg"/>

    <define name="ACCEL_X_NEUTRAL" value="0"/>
    <define name="ACCEL_Y_NEUTRAL" value="0"/>
    <define name="ACCEL_Z_NEUTRAL" value="0"/>
  </section>


 <section name="AHRS" prefix="AHRS_">
    <!-- updated with goodman campus magnetics field -->
    <define name="H_X" value="0.38393"/>
    <define name="H_Y" value="0.0830188"/>
```

```
    <define name="H_Z" value="0.919622"/>
  </section>

  <section name="MISC">
    <define name="NOMINAL_AIRSPEED" value="12." unit="m/s"/>
    <define name="CARROT" value="5." unit="s"/>
    <define name="KILL_MODE_DISTANCE" value="(1.2*MAX_DIST_FROM_HOME)"/>
    <define name="CONTROL_FREQUENCY" value="60" unit="Hz"/>
    <define name="DEFAULT_CIRCLE_RADIUS" value="60." unit="m"/>
  </section>

  <section name="VERTICAL_CONTROL" prefix="V_CTL_">
    <define name="POWER_CTL_BAT_NOMINAL" value="3.7" unit="volt"/>
    <!-- outer loop proportional gain -->
    <define name="ALTITUDE_PGAIN" value="0.06"/>
    <!-- outer loop saturation -->
    <define name="ALTITUDE_MAX_CLIMB" value="2."/>

    <!-- auto throttle inner loop -->
    <define name="AUTO_THROTTLE_NOMINAL_CRUISE_THROTTLE" value="0.45"/>
    <define name="AUTO_THROTTLE_MIN_CRUISE_THROTTLE" value="0.35"/>
    <define name="AUTO_THROTTLE_MAX_CRUISE_THROTTLE" value="0.85"/>
    <define name="AUTO_THROTTLE_CLIMB_THROTTLE_INCREMENT" value="0.2"
                                                          unit="%/(m/s)"
```

```
    <define name="AUTO_THROTTLE_PGAIN" value="0.023"/>
    <define name="AUTO_THROTTLE_IGAIN" value="0.01"/>
    <define name="AUTO_THROTTLE_PITCH_OF_VZ_PGAIN" value="0.05"/>

    <!-- auto pitch inner loop -->
    <define name="AUTO_PITCH_PGAIN" value="0.06"/>
    <define name="AUTO_PITCH_IGAIN" value="0.0"/>
    <define name="AUTO_PITCH_MAX_PITCH" value="0.35"/>
    <define name="AUTO_PITCH_MIN_PITCH" value="-0.35"/>

    <define name="THROTTLE_SLEW" value="0.5" unit="s"/>
  </section>

  <section name="HORIZONTAL_CONTROL" prefix="H_CTL_">
    <define name="COURSE_PGAIN" value="0.9"/>
    <define name="ROLL_MAX_SETPOINT" value="0.70" unit="rad"/>
    <define name="PITCH_MAX_SETPOINT" value="0.5" unit="rad"/>
    <define name="PITCH_MIN_SETPOINT" value="-0.5" unit="rad"/>

    <define name="ROLL_PGAIN" value="6600."/>
    <define name="AILERON_OF_THROTTLE" value="0.0"/>
    <define name="PITCH_PGAIN" value="5500."/>
    <define name="PITCH_DGAIN" value="0.4"/>
```

```
    <define name="ELEVATOR_OF_ROLL" value="2400"/>
  </section>

  <section name="NAV">
    <define name="NAV_GLIDE_PITCH_TRIM" value="0"/>
  </section>


  <section name="FAILSAFE" prefix="FAILSAFE_">
    <define name="DELAY_WITHOUT_GPS" value="2" unit="s"/>
    <define name="DEFAULT_THROTTLE" value="0.5" unit="%"/>
    <define name="DEFAULT_ROLL" value="0.3" unit="rad"/>
    <define name="DEFAULT_PITCH" value="0.5" unit="rad"/>
    <define name="HOME_RADIUS" value="60" unit="m"/>
    <define name="RC_LOST_MODE" value="HOME_MODE"/>
  </section>

 <section name="AUTOPILOT">
   <define name="MODE_MANUAL" value="AP_MODE_ATTITUDE_DIRECT"/>
   <define name="MODE_AUTO1" value="AP_MODE_ATTITUDE_DIRECT"/>
 </section>

  <section name="AUTO1" prefix="AUTO1_">
    <define name="MAX_ROLL" value="60" unit="deg"/>
```

```
    <define name="MAX_PITCH" value="35" unit="deg"/>
  </section>

 <section name="GCS">
    <!--set the icon in GCS to a flying wing. Purely aesthetic.-->
    <define name="AC_ICON" value="flyingwing"/>
  </section>

</airframe>
```

Appendix E

Bill of Materials

E.1 Materials

Part Name	Vendor	Count
PICO-WIDE-V2 Compact PAL Camera	ReadyMade RC	1
Pololu 5V 1A Step-down Voltage Regulator	ReadyMade RC	1
Cricket Pro 5.8GHz VTX w/ Pigtail Connection [1]	ReadyMade RC	1
BLHeli SP Series 20A Opto ESC	ReadyMade RC	1
VAS 5.8 GHz Cloverleaf Omni SMA	ReadyMade RC	1
RMRC Orange Series 450mAh 3S 35C Lipo	ReadyMade RC	1
Cricket 3 Pin Camera Cable	ReadyMade RC	1
Lisa/S Starter Kit	1 Bit Squared	1
Hitec HS-35HD Servo	ReadyMade RC	2
Cheetah A2204/14 1400kv Motor	BP Hobbies	1
M3 Tee Nut	Amazon	2
M3x30mm Screw	McMaster-Carr	2
120 degree, Right hand wound, .484" OD Torsion Spring	McMaster-Carr	1
120 degree, Left hand wound, .484" OD Torsion Spring	McMaster-Carr	1
Mini-banana connectors	Amazon	3
M3 Unthreaded Spacer, 14mm long, 6mm OD	McMaster-Carr	2
M2x5mm Thread Forming Screw	McMaster-Carr	18
M3x10mm Screw	McMaster-Carr	2
M2.5x10mm Screw	McMaster-Carr	4
Custom Circuit Board	N/A	1
Uxcell EP-8060 Propeller	Amazon	1

Table E.1: Components list and costs for current GLUAS design.

Part	Count
Fuselage Upper	1
Fuselage Lower	1
Fuselage Middle	1
Left Wing 1	1
Left Wing 2	1
Left Wing 3	1
Left Elevon	1
Left Wing 4	1
Left Wing 5	1
Right Wing 1	1
Right Wing 2	1
Right Wing 3	1
Right Elevon	1
Right Wing 4	1
Right Wing 5	1
Propeller Mount	1

Table E.2: 3D Printed Components for current GLUAS design.

References

Bahlman, J., Swartz, S., & Breuer, K. (2013). Design and characterization of a multi-articulated robotic bat wing. *Bioinspiration and Biomimetics*.

Bleischwitz, R., de Kat, R., & Ganapathisubramani, B. (2015). Aspect-ratio effects on aeromechanics of membrane wings at moderate reynolds numbers. *AIAA*, *53*(3), 780-788.

Brown, G., Haggard, R., & Norton, B. (2003). Inflatable structures for deployable wings. *AIAA Journal*.

Danforth, B. N., & Michener, C. D. (1988). Wing folding in the hymenoptera. *Entomological Society of America*.

Galinski, C., Lawson, N., & Zbikowski, R. (2004). Delta wing with leading edge extension and propeller propulsion for fixed wing MAV. In *24th international conference of the aeronautical sciences.*

Galinski, C., & Zbikowski, R. (2007). Some problems of micro air vehicles development. *Bulletin of the Polish Academy of Sciences*, *55*(1), 91-98.

Hepperle, M. (n.d.). *Electric flight - potential and limitations* (Tech. Rep.). NATO.

Ifju, P. G., Jenkins, D. A., Ettinger, S., Lian, Y., & Shyy, W. (2002). Flexible-wing-based micro air vehicles. *American Institude of Aeronautics and Astronautics*.

Lian, Y., & Shyy, W. (2007). Laminar-turbulent transition of a low Reynolds number rigid or flexible airfoil. *AIAA Journal*, *45*(7), 1501-1513.

Pelletier, A., & Mueller, T. J. (2000). Low Reynolds number aerodynamics of low-aspect-ratio, thin/flat/cambered-plate wings. *J. Aircr.*, *37*(5), 825-832.

Saito, K., Nomura, S., Yamamoto, S., Niiyama, R., & Okabe, Y. (2017). Investigation of hindwing folding in ladybird bettles by artificial elytron transplantation and microcomputed tomography. *PNAS*, *114*(22), 5624-5628.

Schutter, T. (2016). *Design, fabrication, and characterization of a gun-launched deployable-wing unnamed aerial system* (Unpublished master's thesis). Lehigh University.

Selig, M. S. (2010, August). Modeling propeller aerodynamics and slipstream effects on small uavs in realtime. In *AIAA atmospheric flight mechanics 2010 conference.* Toronto, Ontario, Canada: AIAA.

Stanford, B., Ifju, P., Albertani, R., & Shyy, W. (2008). Fixed membrane wings for micro air vehicles: Experimental characterization, numerical modeling, and tailoring. *Progress in Aerospace Sciences*, *44*, 258-294.

Stowers, A., & Lentink, D. (2015). Folding in and out: passive morphing flapping wings. *Bioinspiration and Biomimetics*, *10*.

Thamann, M. (2012). *Aerodynamics and control of a deployable wing uav for automomous flight* (Unpublished master's thesis). University of Kentucky.

Torres, G. E., & Mueller, T. J. (2004). Low-aspect-ratio wing aerodynamics at low reynolds numbers. *AIAA J.*, *42*(5), 865-873.

Vega, A., Bose, P., & Buyuktosunoglu, A. (2017). Rugged embedded systems. In T. Green (Ed.), (p. 207-235). Cambridge, MA: Elsevier.

Watkins, S., Milbank, J., & Loxton, B. J. (2006). Atmospheric winds and their implications for microair vehicles. *AIAA*.

Zuo, L. X., & Wang, J. J. (2010). Planform and flexibility on lift characteristics for flow over low-aspect ratio wings. *Journal of Aerospace Engineering*, *23*(1), 55-61.

Vita

Douglas Bahr Rumbaugh, Jr. was born in Warminster, Pennsylvania, on November 26th, 1993, to Douglas Rumbaugh Sr. and Tammy Rumbaugh. He graduated *magna cum laude* from Harrisburg University of Science and Technology in 2016, with a Bachelors of Science in Computer and Information Sciences, with a concentration in Software Engineering. He began work on his Master's of Science in Mechanical Engineering at Lehigh University later that same year.

Douglas held an adjunct lecturer position at Harrisburg University in 2016, and again starting in 2018. He has worked in database and mainframe (COBOL) programming through Computer Aid Inc. for Highmark Inc. and Kaiser Permanente, and later as an independent consultant for WildFig Data, performing Python and database programming work. He is the co-creator of the Rumbaugh-Bricker Machine Instruction Set, an emulated machine language designed to lower the barrier of entry to machine-level programming for students.